Investigation of Gas Sensing and Diode Laser Frequency Stabilisation Using Novel Photonic Microstructures

Thesis
by

PABLO PINEDA-VADILLO

Submitted to the

University of Dublin

for the degree of

DOCTOR OF PHILOSOPHY

School of Physics
University of Dublin
Trinity College Dublin

March 2010

Declaration

This thesis has not been submitted as an exercise for a degree in this or any other university. The work described in this thesis is entirely my own, with exception of assistance recognised in the acknowledgements and the collaborative work noted in the publications. I agree that Trinity College may lend or copy this thesis on request.

Investigation of Gas Sensing and Diode Laser Frequency Stabilisation Using Novel Photonic Microstructures

By Pablo Pineda-Vadillo *March 2010*

Summary

Laser spectroscopy is nowadays a widespread research field with countless applications across multiple disciplines. In particular, the application to gas sensing in the near-infrared region significantly benefits from the specific properties of laser sources. Gas species exhibit well-defined, complex spectral absorption structures that require the utilisation of tuneable, high resolution and spectrally narrow sources to be resolved. Such requirements are fulfilled by several types of Tuneable Diode Lasers (TDL's) readily available from the optical telecommunication industry, where much work was done during the last decades to develop and improve the characteristics of these laser devices. Further technology development and intensive research has lead to TDL's of high optical power and narrow emission linewidth to be routinely available for research groups across the world, thus opening the possibility for investigation of gas absorption processes of increasing complexity and very narrow spectral scales. In addition, advances in manufacturing technology have enabled the design and fabrication of new photonic microstructures in parallel to the development of laser sources. The combination of both factors has thus multiplied the possibilities for challenging gas-sensing research, which in turn reveals new fundamental characteristics of gaseous systems whose study requires more and more stable, narrow linewidth and powerful laser sources.

The overall aim of the research presented in this thesis is thus to investigate the application of some specific novel microstructures to gas sensing, making use of high precision DL's and paying special attention to DL frequency stabilisation schemes. In particular, two different photonic microstructures were utilised during our experimental work. On one hand, laser spectroscopy experiments were performed making use of the so-called *Hollow-Core Photonic Bandgap Fibres (HC-PBF*'s). PBF's represent a radically new approach to light guidance in optical fibres based on electromagnetic interference effects, with the special case of HC-PBF's suited to gas sensing experiments due to their hollow-core structure. Experiments were carried out both under the linear and nonlinear absorption regimes, targeting acetylene gas hosted within the hollow fibre. The basic sensing properties of the fibre were first tested under a linear absorption regime, paying attention to HC-PBF-specific effects. Experimental work was then carried out under a nonlinear absorption regime, and the change in absorption properties of acetylene due to saturation effects of the corresponding absorbing transitions characterized. A novel saturation scheme is reported, where saturation of the absorbing transition at two different wavelengths opens up new possibilities for study of nonlinear effects. Absorption features in the saturation regime are characterized by their very narrow spectral linewidth, a fact that makes them attractive to investigation of laser frequency stabilisation schemes. Thus, further experimental work was carried out regarding HC-PBF-based DL frequency stabilisation. Successful implementation of a novel modulation-free technique to lock the emission frequency of DL's is reported, and comparison with existing methods presented.

On the other hand a second type of photonic microstructure was studied during our experimental work, namely *optical microspheres*. Optical microspheres are three-

dimensional optical microresonators within whose volume laser light can propagate for long periods of time with minimum losses. During our experimental research the particular case of *Whispering Gallery Modes* (WGM's) was studied, a special type of optically guided modes where light is confined very near to the surface of the microspheres by *Total Internal Reflection* (TIR). A fabrication process based on fibre melting was implemented that allowed for fabrication of high-quality silica microspheres, into which light was coupled using an optical-prism-based scheme. The spectral shape of the WGM's in high-quality microspheres critically depends, among other factors, on the linewidth properties of the utilised laser source. Our experimental work was carried out using DL's of different linewidth characteristics, and the morphology of WGM's excited within the microspheres was investigated. Much work has been done using these type of microspheres with applications in several fields. In our case, optimization of the experimental scheme lead to the successful implementation of a novel technique to measure the linewidth properties of laser sources. The emission linewidth of a DL was successfully estimated and is reported in this thesis, with consistent results as compared to other well-established linewidth measurement schemes.

In summary, the results reported in this thesis significantly contribute to enhancing the capability of performing high-accuracy gas sensing and DL frequency stabilisation experiments making use of novel photonic microstructures. Several novel schemes are demonstrated based on affordable DL's and laboratory equipment, with comparable results to other more complex schemes. Suggestion for further optimization of the novel schemes is discussed, as well as possibilities for future work in this very interesting physics research field.

Acknowledgments

Not an easy thing to look at a blank page and bring your memory back over the last four years, but there we go...

On top of the *list,* my deepest gratitude goes for **Prof. John Donegan** for smiling since the first time I made my way into that office until the last time I will, giving me the chance under his supervision to join the photonics group that would become my scientific neighbourhood during my Dublin times in such a nice way.

The Pav also counts, it's been the beer neighbourhood as well!

How to talk about supervision and smiles without inviting **Dr. Vincent Weldon** and **Mr. Mick Lynch** to approach and climb up to the podium right now? May I invite them to please come over and collect their respective pint-trophy, for it has been the super-combined power of these three superheroes that have helped me through my long PhD way. A pint that has been in many occasions full of Guinness, but more important of experimental help and theoretical discussions, laboratory guidance and scientific writing help, friendly voice over the phone or in some lines with an email. Only when you look back at the pile of books and papers on your desk, semidestroyed first lab book or oldest data hidden in your PC does your mind realize that you actually know a lot more than a good while ago, and how much effort and help they have put on this game.

For you, three musketeers, up the pints and loud CHEERS!

But I've got a big Dublin limo this time, so there is still plenty of space left. The rest of senior researchers in the group please come and take your honorific seats, still fighting with the lasers with brave and master skills! Please welcome the old guard that helped me during my first and subsequent steps. Mr.McInerney & mr.Richard, good coffee support, lab questions and help; Ms. Kinsella and Robbie, make-pay-slips and important documents to reach their final place; Mr. Ken *Gates*,

tweak-and-repair; the *Ironmen* a.k.a workshop, with countless bits and pieces for scientific research.

And of course both of you, wise Doctor Gerlach and Dr.Severine!! Side by side many years, sharing time in the luxurious dining hall and helping me deal with laser fears.

And you are still all impatient to find your names here, those who enjoyed Salthill or even made it to Kinsale!! KemiChristy could not enjoy twice, but her name appears first for her patience and lab help. From Dublin or west coast, Ukraine, Polska or 中国; with a thick beard or glassess, like for cones, the best bratwurst or always grabbing a tea; in the SNIAM or Westland, somewhere in the Hamilton or the labs. You all have been or still are around here, the Semiconductor Photon-ers making these years so enjoyable and full of small details!!

You didn't find your names, but will make sure to pass you all a honest THANKS-pint.

A lot of work done, a lot of names to name,
Physics is boring some say? You are all invited, please come here and check.
My coffees and coffee crew, in my hand drawing pens,
How could I live without them, even for a single day???

From the superheroes in the podium to the whole crew in the limo, for their invaluable help in achieving, after all, **the main aim**: Here you are, thesis. Well done.

PABLO

List of Publications and Presentations

Oral and poster presentations

- Pablo Pineda-Vadillo, Michael Lynch, John F. Donegan and Vincent Weldon, "**Non-Resonant Wavelength Modulation Saturation Spectroscopy In Acetylene-Filled Hollow-Core Photonic Bandgap Fibres Applied To Modulation-Free Laser Diode Stabilization**", poster presentation, 7th International Conference on Tunable Diode Laser Spectroscopy, 13-17th July 2009, Zermatt, Switzerland.

- Christy Charlton, Michael Lynch, Pablo Pineda-Vadillo, John F. Donegan and Vincent Weldon, "**Whispering Gallery Modes in Glass Microspheres for Near Infrared Gas Sensing**", oral presentation, EUROPTRODE IX European conference, 30th March-2nd April 2008, Galway, Ireland.

- Christy Charlton, Michael Lynch, Pablo Pineda-Vadillo, John F. Donegan and Vincent Weldon, "**NIR Gas Sensing by Whispering Gallery Modes Excited in Glass Microspheres**", poster presentation, Photonics Ireland conference, 24-26th September 2007, Galway, Ireland.

- Pablo Pineda-Vadillo, Michael Lynch, Christy Charlton, John F. Donegan and Vincent Weldon, "**Nonlinear Saturation Spectroscopy in Acetylene-Filled Hollow-Core Photonic Bandgap Fibres Using Tuneable Laser**

Diodes", poster presentation, Photonics Ireland conference, 24-26th September 2007, Galway, Ireland.

- Vincent Weldon, Michael Lynch, Pablo Pineda-Vadillo, Christy Charlton, D. McInerney, John F. Donegan, "**Spectroscopic Based Gas Sensing Using Widely Tuneable Diode Lasers**", poster presentation, US-Ireland R&D partnership sensors workshop, 20th-21st February 2007, Dublin, Ireland.

Publications

- Pablo Pineda-Vadillo, Vincent Weldon, Michael Lynch and John F. Donegan, "**Non-Resonant Wavelength Modulation Saturation Spectroscopy In Acetylene-Filled Hollow-Core Photonic Bandgap Fibres Applied To Modulation-Free Laser Diode Stabilization**", Opt. Express **17**, 23309-23315 (2009)

List of Acronyms Used

AM – Amplitude Modulation
AOM - Acusto-Optical Modulator
BS - Beam Splitter
CM - Centre of Mass
CW – Continuous Wave
DBR - Distributed Bragg Reflector
DFB - Distributed Feed Back
DM - Discrete Mode
ECL – External Cavity Laser
EDFA - Erbium-Doped Fibre Amplifier
EOM - Electro-Optical Modulator
FM - Frequency Modulation
FP - Fabry-Perot
FSR – Free Spectral Range
FWHM - Full Width at Half Maximum
HC-PBF - Hollow-Core Photonic Bandgap Fibre
LD - Laser Diode
LIA - Lock-In Amplifier
NIR – Near Infra Red
PBF - Photonic Bandgap Fibres
PD - Photodiode
RF - Radio Frequency
RMS - Root Mean Square
SG-DBR – Sampled Grating Distributed Bragg Reflector
SM – Single Mode
SNR - Signal-to-Noise Ratio
TEC - Thermo-Electric Cooler
WGM - Whispering Gallery Modes
WM - Wavelength Modulation
PC - Photonic Crystals
TM - Transverse Magnetic
TE - Transverse Electric
TLD - Tuneable Laser Diode
WM - Wavelength Modulation
WMS - Wavelength Modulation Spectroscopy

Dedication

¿Lo ves, Grejo?

Al Grejo-Cangrejo y la Arhuelita Máhica,
Los mejores.

Abuelo, siempre te querremos.

Va por ti, abuelo Heli. D.E.P.

El purito

Pónmelo difícil,
tráeme batallas,
que ya me encargaré yo
de seducir a bibliotecarias.

KASE.O.
& TÉCNICA PURITO

TABLE OF CONTENTS

CHAPTER 4:
SATURATION-BASED LASER FREQUENCY STABILISATION

CHAPTER 5:
LASER LINEWIDTH ANALYSIS AND SPHERICAL MICROCAVITIES

CHAPTER 1

INTRODUCTION

1.1. INTRODUCTION

Optical gas sensing overview

Spectroscopic sensing of chemical species is nowadays present in most analytical chemical laboratories, with spectrophotometers that recognize different species from their characteristic absorption, fluorescence or Raman scattering spectra. In the case of gas detection the most common method is the analysis of the spectral transmission, carried out in two principal regions of the optical spectrum. In the shorter wavelength region, covering approximately the UV-visible blue interval (≈ 250-500 nm), gas absorption or emission lines are detected which arise from atomic/molecular electronic transitions. In the longer wavelength region, covering the near and mid-infrared bands (≈ 750-6000 nm), the vibrational and rotational absorption processes are however more significant. The loss of photon energy contributes to the kinetic energy of the gas absorbing molecules, with either individual atoms vibrating relative to other atoms within the molecule (vibrational absorption) or the molecule itself rotating as a whole (rotational absorption).

A special case among gas spectrometry is that of optical-fibre-based gas sensors [1], where optical fibres play a key role in the detection scheme. A vast number of such

type of sensors exist, due to an extensive range of available technologies (fibre gratings, interferometers, etc.) and measured parameters (strain, temperature, etc.). Those schemes operating in the short wavelength spectral region are not suitable for long-distance remote sensing applications due to the intrinsic loss of silica fibres at that interval. On the contrary, when fibre-based gas sensors operate at the longer wavelength region losses due to silica absorption are avoided and remote gas sensing becomes a feasible application. In addition, laser light sources operating in such near and mid-infrared bands are readily available from the telecommunication industry, exhibiting particular properties that help enhancing spectroscopic-based sensing.

Many types of optical fibre sensor technologies are currently approaching saturation [2], but in recent years remarkable progress in some technology areas has given rise to new state-of-the-art sensor schemes attracting the attention of researchers. In particular, the work presented in this thesis is related to the advances in photonic crystal technology applied to near-infrared fibre-based optical gas sensing, together with the application of optical microcavities for laser frequency stabilisation purposes.

Laser spectroscopy in novel photonic microstructures

The use of laser sources for optical spectroscopy experimentation is a well-established, cross-disciplinary field where an enormous number of applications lie within research areas as broad as Physics, Chemistry or Biology [3]. The high optical intensity achieved with these types of sources, along with the extraordinary monochromaticity of their optical output, as compared with incoherent sources, has a huge impact in spectroscopy research since lasers became routinely available as part of laboratory equipment across the world. High optical powers and wide tuneability

characteristics opened up the possibilities for experimental investigations at an atomic and molecular level, which have nowadays reached limits hardly imaginable just few decades ago. In particular, investigation of many gaseous species of environmental and/or industrial interest has significantly benefited from semiconductor laser diodes (LD's) developed for the telecommunications industry [4-6]. These LD's operate in the near-infrared region where the overtone/combination absorption spectra of many gases occur, so the intensive research and development concerning these devices for the telecommunications sector indirectly contributed to the subsequent growth and development of laser-based gas sensing techniques.

On the other hand advances in the photonics manufacturing technology have made it possible for theoretical proposals to become experimentally feasible, ultimately leading to the appearance of novel photonic microstructures for experimental research. A special case is that of the *Photonic Bandgap Fibres* (PBF's, also referred sometimes as *Photonic Crystal Fibres* though we will use the more general *Bandgap* term during this thesis), where a photonic crystal structure [7] is embedded along the micrometer-sized core of an optical fibre giving rise to a bandgap guidance mechanism. Much work has been done on this exotic type of optical fibre since the original design was first proposed and implemented, with tens of different PBF structures available at present giving rise to a wide range of applications making it a *hot topic* in photonics research [8, 9]. During the research described in this thesis a particular type of PBF is utilised, because it suits laser-based gas sensing experiments due to its inherent properties: the *Hollow-Core* PBF (HC-PBF). This type of PBF consists of an array of hollow micro-capillaries distributed over the cross-section of a silica fibre in a photonic crystal geometry surrounding a larger

hollow core. Light is tightly focused within the narrow core, usually of the order of 10-20 μm in diameter, giving rise to a significant enhancement of the optical field intensity. Light is normally guided along the air-filled core [10], but when gas is hosted within the microstructure the light interaction with molecules is greatly enhanced due to the intense field. During our experimental work we have characterized the absorption properties of acetylene gas hosted in a HC-PBF. Acetylene is a linear molecule with no permanent dipole moment and exhibits a well-defined, regularly-spaced absorption spectrum around 1.5 μm. Both the linear and nonlinear absorption regimes have been investigated using LD's acquired from the telecommunications industry. High-power Distributed Feed Back (DFB) LD's were used to investigate the change in absorption properties of the gas under a nonlinear absorption regime, demonstrating a novel scheme for the study of saturation effects.

In addition, special attention has been paid to the frequency stabilisation of LD's during the research presented in this thesis, as this is one of the most important laser characteristics regarding both spectroscopic and communications applications. A novel laser stabilisation scheme was proposed and demonstrated based on the nonlinear saturation of acetylene in HC-PBFs. Absolute frequency stabilisation of a high-power DFB LD was achieved in a modulation-free format, obtaining stabilisation figures comparable to other more complex techniques. A second type of optical microstructure, namely *optical microspheres* or *micro-resonators,* has been used to characterise the frequency noise in laser sources. When light is evanescently coupled into high-quality microspheres under appropriate conditions, the so-called *Whispering Gallery Modes* (WGM's) excited within the microcavity can travel almost in a lossless fashion confined to the proximity of the surface. A vast number of applications exist that make use of these special modes within a microspherical

cavity, and make this topic a very active one nowadays [11]. During the final part of the research project the dependence of the WGM's spectral morphology on the linewidth characteristics of the laser source was studied, using a carefully optimized experimental set-up. A novel WGM-based method to estimate the emission linewidth of diode lasers was demonstrated and it yields consistent results with other well-established experimental techniques, opening up the possibility for future work and research.

1.2. THESIS OVERVIEW

- **Chapter 1** aims to provide a general introduction about our research project, introducing the basic concepts and setting the context for the particular experiments to be presented in following chapters.
- **Chapter 2** includes a summary of the most important theoretical concepts and experimental methods required to understand and perform basic gas sensing and laser spectroscopy experiments. Topics covered include linear absorption laws, spectral broadening processes, description of laser sources for spectroscopic applications, modulation detection techniques, basic molecular structure and properties of acetylene and description of HC-PBFs. Basic experimental results are presented to support the theoretical approach.
- **Chapter 3** deals with the experimental work carried out in acetylene-filled HC-PBFs under a nonlinear absorption regime. A proper theoretical background is set prior to presentation of experimental results, which include characterization of nonlinear absorption properties of acetylene and

demonstration of a novel *double* saturation scheme (where saturation is alternatively achieved at *two* different wavelengths in a novel approach).

- **Chapter 4** focuses on the application of the nonlinear absorption transitions presented in chapter 3 to laser frequency stabilisation. Fundamental theory regarding laser frequency stability is accordingly presented to support the reported experimental results. A novel stabilisation scheme is proposed and demonstrated achieving high-accuracy absolute frequency stabilisation of a high-power DFB LD. This method is based in the implementation of *Wavelength Modulation* (WM) techniques within the experimental scheme presented in chapter 3.
- **Chapter 5** details the experimental work carried out using optical microspheres and laser-excited WGM's. An extensive theoretical basis is first presented, covering the fundamental theory of laser linewidth in LD's, common laser linewidth measurement techniques (*self-homodyne* and *heterodyne* schemes) and main properties and description of optical microspheres. A brief description of the particular *Discrete Mode* (DM) laser sources utilised during the experimental work is also included. Experimental results are then presented for the fabrication of silica microspheres, DM and DFB DL's self-homodyne linewidth measurements, morphology of excited WGM's and demonstration of a novel microsphere-based linewidth estimation technique.
- **Chapter 6** summarises the experimental work presented during the thesis, assessing the fulfilment of the research project aims and suggesting several possibilities for future work.

1.3. REFERENCES

1. B. Lee, "Review of the present status of optical fiber sensors," Optical Fiber Technology **9**, 57-79 (2003).

2. B. Lee, S. Roh, and J. Park, "Current status of micro- and nano-structured optical fiber sensors," Optical Fiber Technology **15**, 209-221 (2009).

3. W. Demtröder, *Laser Spectroscopy: Basic Concepts and Instrumentation, 2Ed* (Springer, 1996).

4. V. P. Duraev, and A. V. Melnikov, "Single frequency DFB lasers for high resolution spectroscopy," Spectrochimica Acta Part A: Molecular and Biomolecular Spectroscopy **52**, 877-879 (1996).

5. K. H. Schlereth, "III-V semiconductor lasers: application in telecommunication systems - suitability for spectroscopy," Infrared Physics & Technology **37**, 129-142 (1996).

6. F. Wittgrefe, M. D. Hoogerland, and J. P. Woerdman, "Semiconductor lasers for spectroscopy," Measurement Science and Technology, 304 (1991).

7. J. D. Joannopoulos, *Photonic crystals : molding the flow of light* (Princeton University Press, Princeton, 2008).

8. J. C. Knight, "Photonic crystal fibres," Nature **424**, 847-851 (2003).

9. P. S. J. Russell, "Photonic-Crystal Fibers," Lightwave Technology, Journal of **24**, 4729-4749 (2006).

10. R. F. Cregan, B. J. Mangan, J. C. Knight, T. A. Birks, P. S. J. Russell, P. J. Roberts, and D. C. Allan, "Single-Mode Photonic Band Gap Guidance of Light in Air," Science **285**, 1537-1539 (1999).

11. A. Chiasera, Y. Dumeige, P. Féron, M. Ferrari, Y. Jestin, G. N. Conti, S. Pelli, S. Soria, and G. C. Righini, "Spherical whispering-gallery-mode microresonators," Laser & Photonics Review **9999**, NA (2009).

CHAPTER 2

BASIC GAS SENSING AND HOLLOW-CORE PHOTONIC BANDGAP FIBRE CHARACTERIZATION

2.1. INTRODUCTION

Optical Spectroscopy is a widely used technique for analysing the properties of different types of materials, where a light beam interacts with a sample producing a characteristic optical signal. Different information about the material may be extracted depending on the type of light used (visible, IR, etc.), the specimen (solid, liquid, gaseous, etc.) and the nature of the signal collected (transmitted, reflected, scattered, etc.). Laser Spectroscopy, as its name suggests, makes use of laser light sources exploiting some of their inherent properties to enhance detection results. Some characteristics, such as high monochromaticity and directionality of laser beams along with wide tuning capabilities, represent major reasons to investigate and use laser-based spectroscopy techniques [1].

In this chapter the main properties of laser-based spectroscopy techniques relevant to our experimental work will be presented. Basic optical absorption laws, absorption linewidth broadening processes and in particular optical absorption by gases will be

discussed. Specific characteristics of both the acetylene gas targeted during our work and the Laser Diodes (LD's) utilised are included, together with a description of the Hollow-Core Photonic Bandgap Fibre (HC-PBF) microstructure used for experimental research. The theoretical approach is finally backed up by some basic characterization measurements of our detection system, setting the basis for further investigation of the system in upcoming chapters.

2.2. BACKGROUND

2.2.1. LIGHT ABSORPTION: BEER'S LAW

Light of angular frequency $w=2\pi v$ travelling through a material of refractive index n can experience a number of different processes. In general, part of the incoming radiation is absorbed by the medium, while the rest is free to propagate until it eventually escapes, retaining its original propagation direction –transmitted light- or presenting some deviation - scattered light-. *Absorption* processes are accompanied by *dispersion* of the light, the latter defined by the change in phase velocity of light from its value in vacuum c. These properties of the interaction of electromagnetic radiation with an absorbing medium are classically described by an oscillator model for the atomic electrons, leading to the definition of a complex refractive index to explain both effects. It is the purpose of this section to present the basic rules governing linear absorption of light by a medium of refractive index n, with the nonlinear absorption regime further discussed in chapter 3. Understanding the basic laws governing optical absorption processes is crucial in our case, as most of the experimental work presented in this thesis is related to such an effect.

Beer-Lambert Law

Consider a light beam travelling along the Z direction of an absorbing medium of number density C and transverse area A. The total number of illuminated molecules for a material thickness dz is $CAdz$, though the effective area presented by this ensemble is given by $\sigma CAdz$, σ being the cross-section for absorption/scattering in this case. Thus, the total probability for a molecule of being either absorbed or scattered out of the beam will be [2]

$$\frac{dI_z}{I_z} = \frac{\sigma CAdz}{A} \tag{2.1}$$

which upon integration gives the so-called Beer-Lambert law for linear attenuation

$$I = I_0 e^{-\sigma Cz} = I_0 e^{-\mu z} \tag{2.2}$$

If scattering is neglected, then the *linear attenuation coefficient* $\mu=\sigma C$ is equal to the *linear absorption coefficient* α and the Beer-Lambert relation can be rewritten in the form

$$I(\lambda) = I_0(\lambda) e^{-\alpha(\lambda) z} \tag{2.3}$$

where the dependence of the absorption coefficient on the wavelength λ of the incoming light is explicitly indicated. In Optical Spectroscopy, the Beer-Lambert law is usually expressed in terms of the incoming plane wave angular frequency $\omega = 2\pi c/\lambda = 2\pi\upsilon$, and the medium, frequency-dependent, complex refractive index $n(\omega)$. The treatment presented by Measures [3] (special emphasis on the use of tuneable laser diodes in laser absorption measurements) is appropriate in our specific case, hence we can write

$$n(\omega) = \eta(\omega) + \frac{1}{2} i\chi(\omega) \tag{2.4}$$

where the real part of the refractive index $\eta(\omega)$ accounts for the dispersion of the light as it travels through the medium and the imaginary term $\chi(\omega)$ is related to its absorption properties. The oscillator model for an electromagnetic wave travelling through a medium of complex refractive index (2.4) leads to the well-known *Kramers-Kronig* dispersion relations relating these two terms, which apply in the proximity of an atomic transition frequency ω_0 and for the case of the imaginary term reads [3]

$$\chi(\omega) = \frac{Ne^2 f_0 \gamma}{4\epsilon_0 m_e \omega[(\omega - \omega_0)^2 + (\gamma/2)^2]} \tag{2.5}$$

where N is the number density of oscillators, e and m_e the charge and mass of the electron, respectively, and γ the damping constant for the oscillator model. The absorption coefficient introduced in (2.3) is related to the imaginary term of the refractive index so that

$$\alpha(\omega) = \frac{\omega\chi(\omega)}{c} \tag{2.6}$$

where c is the speed of light in vacuum. It is thus convenient to refer to the frequency-dependent form for the Beer-Lambert law for consistency,

$$I(\omega) = I_0(\omega) e^{-\alpha(\omega) z} \tag{2.7}$$

Lineshape function

In spectroscopic applications, the Beer-Lambert law (2.7) can be written as

$$I(\tilde{\upsilon}, z) = I_0 e^{-\kappa(\tilde{\upsilon}) z_D} = I_0 e^{-\kappa(\tilde{\upsilon}) C z} \tag{2.8}$$

where $\kappa(\tilde{\upsilon})$ is the absorption coefficient at the frequency $\tilde{\upsilon}$ when the latter is expressed in inverse length units according to the relations

$$\tilde{\upsilon}(cm^{-1}) \equiv \frac{1}{\lambda(cm)} \equiv \frac{\upsilon(Hz)}{c(cm\ s^{-1})} = \frac{\omega(Hz)}{2\pi c(cm\ s^{-1})} \tag{2.9}$$

and $z_D = Cz$ is the so-called *optical density* with generic units of concentration times length (we have used the notation introduced in (2.2)). The absorption coefficient $\kappa(\tilde{\upsilon})$ thus has units of reciprocal concentration times length, and is normally expressed in 1/(molecules cm^{-3} cm) or (cm^2/molecule). We will simplify the notation from now on and use υ when referring to $\tilde{\upsilon}(cm^{-1})$ for more clarity. Because the shape of the absorption profile is generally of interest (as it is during our experimental work), the absorption coefficient can be rewritten in a more useful form according to

$$\kappa(\upsilon) = Sg(\upsilon - \upsilon_o) \tag{2.10}$$

where the so-called *linestrength S* is essentially the integrated absorption coefficient and includes information about the absorption profile shape,

$$S = \int_{-\infty}^{\infty} \kappa(\upsilon) d\upsilon \tag{2.11}$$

while the *lineshape function* $g(\upsilon - \upsilon_o)$ is normalised according to

$$g(\upsilon - \upsilon_0) = C\phi(\upsilon - \upsilon_0), \quad \int_{-\infty}^{\infty} g(\upsilon - \upsilon_0)d\upsilon = 1 \tag{2.12}$$

and allows intensity profiles described by $\phi(\upsilon - \upsilon_o)$ to be compared directly. A common choice is that the concentration C in (2.8) is expressed in molecules/cm^3 since these units are independent of temperature (if the absorbing medium is a gas and concentration is expressed in terms of pressure units, then its equation of state needs to be specified). In that case S has units of cm/molecule and the lineshape function $g(\upsilon - \upsilon_0)$ is given in cm according to (2.10). The mathematical form for the lineshape function in the most important cases affecting our experimental work will be presented in the upcoming section 2.2.3.

2.2.2. LIGHT ABSORPTION IN GASES

Optical absorption was investigated in our case regarding a gaseous absorbing medium. Most of the experimental work presented in upcoming chapters 3 and 4 was carried out utilising **acetylene** ($^{12}C_2H_2$) as the target gas, so a brief summary of the main properties of this molecule relevant to our work will be included here. During some specific stages of our experiments we used commercial gas cells which also contained different quantities of ammonia (NH_3) and hydrogen cyanide (HCN).

Optical absorption by a gas occurs when the energy carried by an incoming photon is resonant with the difference between two molecular energy states. The distribution of energy states for a gas is determined by three types of motion, namely *rotational*

(molecules rotating about its centre of mass, CM), *vibrational* (vibrations of individual/sets of atoms within a molecule with a static CM) and *electronic* (electrons moving within the molecule). Depending on the particular symmetry of the targeted molecule, the energy levels are distributed in a specific manner. In addition, these three types of motion interact with each other according to established selection/combination rules, giving rise to very complex absorption spectra in some cases.

In the case of the acetylene gas targeted during our experimental work, the absorbing transitions belong to the *rotational-vibrational combination band* $\upsilon_1+\upsilon_3$. We can describe the main properties of such bands as follows. First of all, we are working within a *vibrational* band characterized by its corresponding vibration frequency υ. Secondly, the band is not centred at a *fundamental* vibration frequency υ_i, but at a *combination* value $\upsilon_i + \upsilon_j$ (υ_1 and υ_3 correspond to two of the total five normal vibration modes available for acetylene [4]). Thirdly, the absorbing transitions occur between *rotational* energy levels whose distribution is embedded on top of the vibrational modes. This type of rotational-vibrational energy map is illustrated in figure 2-1, corresponding to some of the relevant energy levels and transitions in the simpler case of a diatomic molecule (this figure is adapted from the very comprehensive book on molecular spectroscopy by Banwell [5]). Note how the absorption spectrum schematically shown at the foot of the figure consists of several absorption lines with varying intensities, due to the fact that not all rotational J levels are populated to the same degree in thermal equilibrium. The $\upsilon_1+\upsilon_3$ band for acetylene is centred at a wavelength of approximately 1525.8 nm within the Near Infra Red (NIR) region, where the intensity of absorption lines is much smaller than in the IR fundamental absorption region. This is a very important fact to take into account,

because these weak transitions are difficult to detect unless very sensitive detection schemes are implemented or the gas concentration is high. A more extended, good comprehensive summary of main molecular concepts relevant to spectroscopy can be found in Weldon [6], while an extremely detailed treatment on Infrared and Raman spectra of polyatomic molecules was published by Herzberg and can be consulted for advanced topics [7].

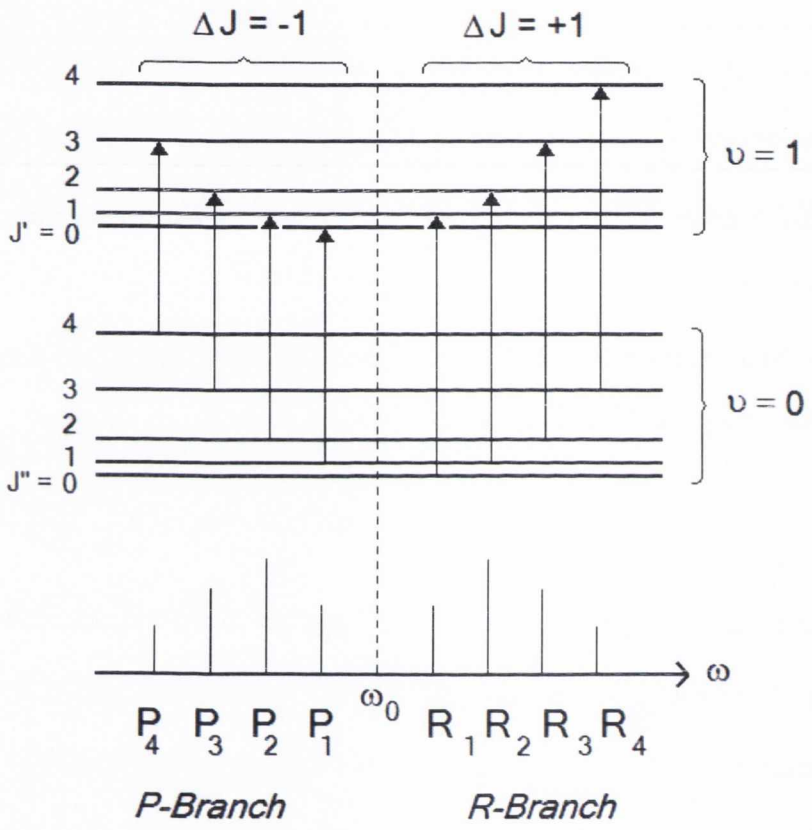

***Figure 2-1**: Schematic diagram for the rotational (J) – vibrational (υ) energy level distribution of a diatomic molecule. The absorption spectrum (bottom) arises from transitions between rotational levels with a change in the rotational number of* ΔJ = -1 (P-Branch) *or* ΔJ = +1 (R-Branch). *The different intensities for the lines are related to the fact that not all levels have the same populations in thermal equilibrium. The scale in the figure does not correspond to the real case, but is readjusted for clarity (figure adapted from Banwell [5]).*

2.2.3. BROADENING PROCESSES

Real absorption profiles for gaseous systems are not δ-like functions but exhibit some finite linewidth due to several broadening effects. The convolution of these effects determines the final lineshape function for the absorbing transition, empirically characterized by its Full Width at Half Maximum (FWHM) as illustrated in figure 2-2 below. Several physical processes affected the absorption profiles during our experimental work, and can be classified/described according to different criteria.

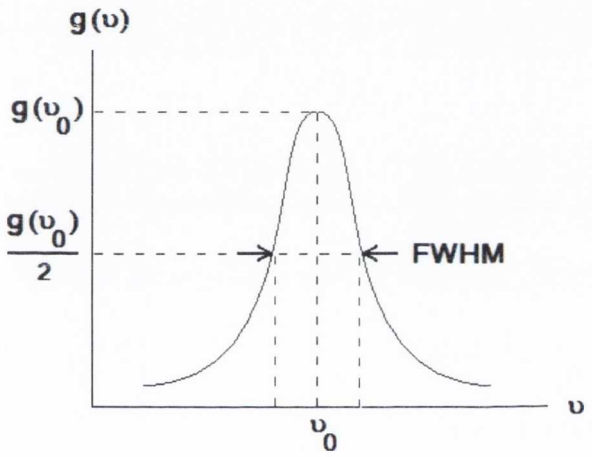

Figure 2-2: *A broadened spectral feature centred at* υ_0 *is described by a lineshape function* $g(\upsilon-\upsilon_0)$ *of maximum intensity* $g(\upsilon_0)$ *and Full Width at Half Maximum (FWHM).*

Firstly, table 2-1 illustrates the classification of broadening mechanisms depending on the distribution of the molecular absorption/emission probability. Not all the molecules in a particular ensemble have the same properties, so different absorption properties apply.

Table 2-1 · Broadening mechanisms: probability	
A. HOMOGENEOUS ***Equal*** *probability of absorption or emission of radiation for molecules in the same energy level.*	B. INHOMOGENEOUS ***Different*** *probability of absorption or emission of radiation for molecules in the same energy level.*
A.1. NATURAL OR RADIATIVE A.2. COLLISIONAL A.3. TRANSIT TIME A.4. POWER	B.1. DOPPLER

Each of the broadening mechanisms presented in table 2-1 arises as a result of a different physical effect. Analysis of each of these mechanisms can be found in the literature with a different degree of detail [1, 8-13], while the discussion in this section will be limited to a summary of the most relevant ideas associated to each of them, as presented in table 2-2. Those broadening processes significantly contributing to the linewidth measurements presented in this thesis are highlighted in light grey, while the remaining are negligible in our case (orders of magnitude are included in table 2-4 at the end of this section). Table 2-3 points out which elements/equipment included in the laboratory set-ups are associated with each of the mechanisms, providing a useful experimental overview.

Table 2-2 · Broadening mechanisms: physical origin	
Broadening mechanism	*Physical origin*
A.1. NATURAL OR RADIATIVE	Finite lifetime τ of excited states produces spread of absorption frequencies, Heisenberg $\Delta E \geq h/2\tau\pi$
A.2. COLLISIONAL	Interparticle/wall collisions: molecular phase shifts
A.3. TRANSIT TIME	Transit of particles through laser beam τ_{TR} shortens effective energy transition lifetime
A.4. POWER	High intensity beam induces molecular populations change, modifying absorption properties
B.1. DOPPLER	Particle velocity distribution (Maxwell) and Doppler effect

Table 2-3 · Broadening mechanisms: laboratory	
Broadening mechanism	*Set-up element/device related*
A.1. NATURAL OR RADIATIVE	Targeted gas (lifetime of targeted transition)
A.2. COLLISIONAL	Targeted gas (pressure, intermolecular collisions) + HC-PBF core walls (molecule-wall collisions)
A.3. TRANSIT TIME	Laser beam cross section within HC-PBF core
A.4. POWER	High power laser in nonlinear absorption experiments
B.1. DOPPLER	Targeted gas (thermal velocity distribution)

As presented in the previous tables, three main broadening mechanisms contribute to our experimental measurements. The most straightforward mechanism is that related

to the well-known **Doppler** effect, where a molecule with a non-zero velocity component in the propagation direction of the radiation field absorbs a photon at some frequency shifted from the resonant transition frequency *at rest*. The distribution of molecular speeds across the whole ensemble of active molecules is given by the Maxwell-Boltzmann distribution, which tells us which molecules fall in which velocity class. The final result is a spectral absorption profile given, to a first approximation commonly used, by a **Gaussian** lineshape function of the form [3]

$$g_D(\upsilon - \upsilon_0) = \left(\frac{2}{\Delta\upsilon_D}\right)\sqrt{ln2/\pi}\exp\left[-\frac{2(\upsilon - \upsilon_0)^2 ln2}{\Delta\upsilon_D}\right] \tag{2.13}$$

with a FWHM of

$$\Delta\upsilon_D = \frac{2\upsilon_0}{c}\sqrt{2kTln2/m} \tag{2.14}$$

Note how the magnitude of the Doppler broadening increases with temperature as $T^{1/2}$ and resonant frequency υ_0. During each of our experiments both the gas temperature and the operating frequency (within some small tuning range) are kept constant, and so the associated Doppler width is essentially constant.

The second effect important to our purposes is the spectral broadening introduced by molecular **collision** processes. Several models exist to explain such an effect, but we will restrict our discussion to the simple Lorentz model followed in [10]. This model assumes that the electron oscillation described by the classical absorption model halts on collision and then restarts with a completely random phase, totally unrelated to that prior to the collision event. This incoherence eventually leads to molecular absorption

at a frequency different than the resonant value, and it can be demonstrated that the collisionally broadened lineshape function is given by a **Lorentzian** curve

$$g_L(\upsilon - \upsilon_0) = \left(\frac{\Delta\upsilon_L}{2\pi}\right)\frac{1}{[(\upsilon - \upsilon_0)^2 + \Delta\upsilon_L^2/4]} \tag{2.15}$$

A rather cumbersome expression for the FWHM ($\Delta\upsilon_L$) of this normalised lineshape is found in the treatment by Measures that we are following [3], so for our explanation purposes we can refer to Svelto [14] where the linewidth for a collisionally-broadened transition is given in a different approach by

$$\Delta\upsilon_L = \frac{1}{\pi\tau_C} = \Delta\upsilon_L^0\left(\frac{P}{P_0}\right)\left(\frac{T_0}{T}\right)^{1/2} \tag{2.16}$$

where τ_C represents the mean time between collisions and the pressure and temperature dependence for the linewidth parameter have been taken from Measures [3] again ($\Delta\upsilon^0{}_L$ is the linewidth at standard pressure and temperature conditions). The most important fact illustrated by relation (2.16) for our experimental purposes is that, at a fixed gas temperature, the collisional broadening increases linearly with pressure. Note that this type of broadening can be introduced not only by intermolecular collisions, but also by collisions of the active molecules with the **walls** of the gas hosting structure. The latter effect is small when gas cells of the order of tens of centimetres of height/widths are used, but in the specific case of our Hollow-Core PBF the wall collisions play a crucial role (the diameter of the utilised fibre was approximately $d \approx 11\ \mu m$). However this fibre-related broadening is in practice almost indistinguishable from the transit-time effect explained next, with treatment in the

literature using one of the two possible approaches. We will follow the transit-time approach when analysing experimental results during chapter 3.

The last of the three significant broadening mechanisms to take into account during our experiments is that related to the **transit-time** effect: under certain physical conditions the transit time of gas molecules *moving* across the laser beam becomes smaller than their excited state lifetime. This *effective* shorter lifetime eventually gives rise to a spread of the absorbing frequencies around the resonant value, as time and optical frequency can be related via the Heisenberg uncertainty relations. It can be demonstrated (Demtröder, [15]) that the spectral intensity profile for atoms perpendicularly traversing a Gaussian laser beam of 1/e diameter *2w* with a velocity v is given by a **Gaussian** curve

$$I(\omega) = I_0 \exp\left[-(\omega - \omega_0)^2 \frac{w^2}{2v^2}\right] \tag{2.17}$$

with a transit-time limited FWHM

$$\Delta\upsilon_{TT} \approx 0.4v/w \tag{2.18}$$

Figure 2-3 further illustrates the previous discussion. Note that this effect depends on the geometry of the fibre, which is fixed in our case, but also on the *gas temperature*: the value for the mean velocity of the gas molecules is given by the kinetic theory of gases and ultimately depends on the temperature *T* for a fixed molecular mass *M* [16].

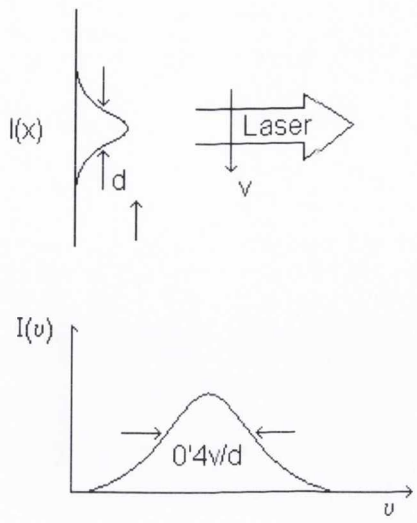

***Figure 2-3**: Transit-time broadening of an absorbing transition, due to absorbing molecules crossing a laser beam in a shorter time than their excited state lifetime. Gas molecules perpendicularly crossing a Gaussian laser beam of 1/e diameter* d *with velocity* v *exhibit an intensity profile* I(υ) *with a FWHM* ≈ 0.4v/d. *Figure adapted from Demtröder [1].*

Thus, the main broadening processes affecting an absorbing transition during our experimental work have been both qualitatively and mathematically described. Note that, in a real situation, the final absorption profile is the result of more than one broadening factor at the same time and cannot be described by the *pure* lineshapes described above. In such case the so-called ***Voigt*** profile must be used, a convolution of a Lorentzian and Gaussian profiles that must be evaluated numerically [3]. A graphical comparison between the normalised Lorentzian, Gaussian and Voigt profiles with the same area under the curve $A = 1$ is included in figure 2-4, where it can be observed that the Voigt profile essentially follows a Lorentzian profile near its wings and a Gaussian curve around the line centre. Further analysis of absorption lineshapes in gases can be found in [17, 18].

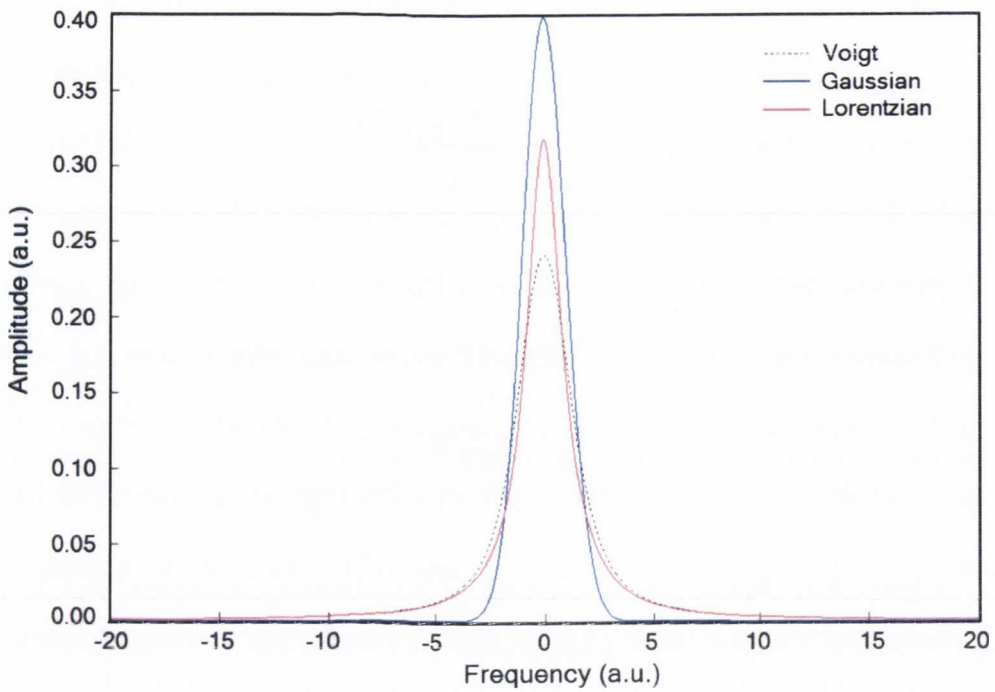

Figure 2-4: *Simulation results for normalised Gaussian, Lorentzian and Voigt lineshape profiles of the same area under the curve* A = 1. *Note how the Voigt profile is essentially similar to a Lorentzian curve at the wings, while it approaches a Gaussian shape at the line centre (scales are adjusted to emphasise the Lorentzian similarity though).*

Orders of Magnitude

It is useful to estimate the orders of magnitude of the broadening processes affecting our measurements under typical experimental conditions. Having an idea of the relative magnitude of the individual contributions helps with optimizing the experimental set-up when required, as well as helping to select the proper relation when performing some theoretical fit of acquired data. According to the previous discussion in this section, there are basically two experimental parameters that determine the final broadening contributions: the gas temperature and pressure. Typical conditions during our experimental work include gas temperatures of $T_{GAS} \approx$ 22 °C and pressures $P_{GAS} \approx 1$ mbar. Table 2-4 below includes some estimation for the

order of magnitude of the broadening processes under such conditions, together with the typical value for the emission frequency linewidth of the utilised diode lasers.

Table 2-4 · Broadening mechanisms: orders of magnitude

Broadening mechanism	Order of magnitude (T ≈ 22 °C, P ≈ 1 mbar)
A.1. NATURAL OR RADIATIVE	Lifetime of targeted molecular transitions (C_2H_2, overtone rotational-vibrational transitions, NIR) $\tau \sim$ ms, $\Delta\upsilon_N \sim$ 100's Hz
A.2. COLLISIONAL	$\Delta\upsilon_{COL} \approx$ 10 MHz
A.3. TRANSIT TIME	$\Delta\upsilon_{TT} \approx$ 50 MHz
B.1. DOPPLER	$\Delta\upsilon_D \approx$ 500 MHz
LASER LINEWIDTH	Typically $\Delta\upsilon_{LAS} \approx$ 1-5 MHz

As it can be observed the broadening is dominated by the Doppler effect at low pressure values. As pressure increases so does the collisional term, eventually dominating the total absorption linewidth at pressures above tens of millibars. The natural linewidth associated with our targeted transitions is negligible, while the power broadening presented in table 2-2 does not apply to our measurements (high-power LD's are used during the experimental work presented in next chapter, but the weak-field approximation where no power broadening occurs applies). Note how the estimated values for these broadening processes –except the negligible natural linewidth term- are significantly higher than the typical emission frequency linewidth of the diode lasers utilised during experimental work.

2.2.4. PHOTONIC BANDGAP FIBRES

It has been mentioned in several occasions how the gas hosting structure that we are using affects particular aspects of the measurements during our experimental work. The so-called Hollow-Core Photonic Bandgap Fibres are a novel, *exotic* type of photonic microstructures, so a description of their working principle and main properties are included next.

Photonic Crystals and Photonic Bandgap Fibres

Standard optical fibres were first designed and still work on the basis of the Total Internal Reflection (TIR) produced due to the refractive index step between the fibre core and cladding materials. However, the appearance of a new type of photonic structures through which light of particular frequencies could not propagate opened up a new, wide range of possibilities. *Photonic Crystals* (PC's, [19]) are periodical structures in which materials of different refractive index alternate according to the geometry imposed by a certain lattice configuration (figure 2-5a corresponds to a hexagonal lattice of air $\varepsilon = 1$ and material of dielectric constant $\varepsilon = 12$). By means of multiple interference effects, based on a detailed analysis of the Maxwell equations, the periodic distribution of the refractive index gives rise to either allowed or forbidden frequency states for photons. The total frequency interval across which light is not able to propagate defines the so-called *Photonic Band Gap* (PBF), analogous to semiconductors and *electronic* bandgaps. By carefully designing the wavelength-scale periodic lattice in a PC and choosing appropriate materials the PBG structure can be tailored with a reasonable degree of freedom, and the bandgap *window* adjusted to a particular value within some range. The corresponding *complete* Transverse Magnetic (TM) bandgap arising from the PC structure presented in figure 2-5a can be observed

in figure 2-5b. Note that the bandgap depends on the particular polarization state of the optical field, with an *incomplete* gap for the Transverse Electric (TE) polarization.

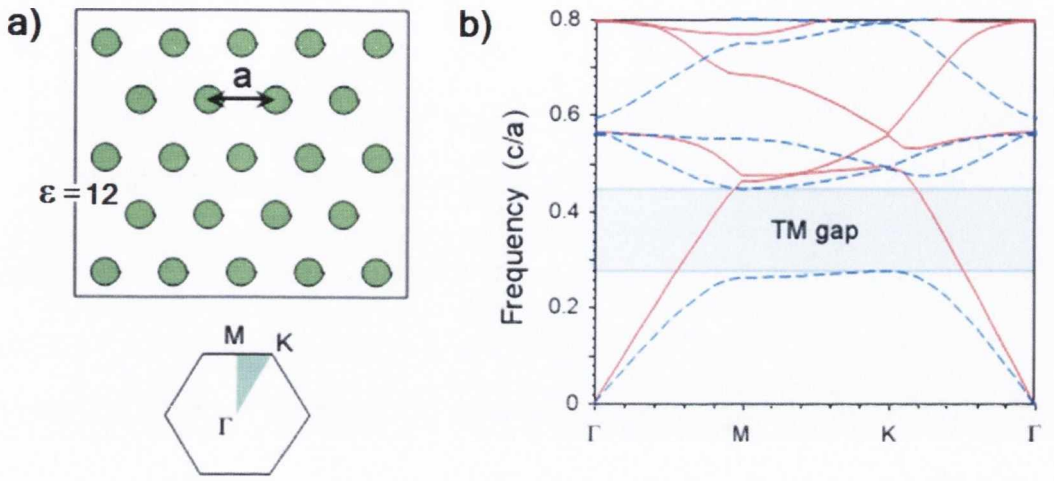

***Figure 2-5**: Example of a two-dimensional photonic bandgap structure (a) created by distributing a material of dielectric constant* ε = 12 *over a hexagonal lattice of parameter* a. *The associated complete TM and incomplete TE frequency bandgaps can be observed in (b). Figure taken from [19].*

On the other hand, it was in the early nineties when the idea of embedding photonic bandgap structures into optical fibres was first proposed. Consequent research and development resulted in the realization of the first *Photonic Bandgap Fibre* (PBF) in 1995 [20], in which a hexagonal close-packed array of air holes running along the inside of a standard, silica fibre, was realized with the help of a stack-and-draw mechanical technique. In an ideal PBF the bandgap structure is designed so that only one fundamental mode is allowed to propagate along the fibre core length. Secondary modes rapidly decay across the surrounding fibre region due to the photonic band gap effect, so that only a small fraction of them manages to propagate off-core. While these secondary modes are of much weaker intensity than the fundamental peak and can be usually neglected, they can significantly change the transmission and

polarization properties of the fibre if coupling of an external single-mode laser is not properly optimized. More details about these coupling effects are included in section 3.3.1 of chapter 3. Many applications have emerged from this new type of fibres [21-26], but the analysis will be restricted here to the gas sensing properties exhibited by certain types of PCFs.

Hollow-Core Photonic Bandgap Fibres and Gas Sensing.

The main feature of the so-called *Hollow-Core Photonic Bangap Fibres* (HC-PBF's) [27-30] is, as suggested by the name, the presence of a hollow core. The core, along with a surrounding array of air holes distributed according to a PC structure, is typically embedded within a standard silica fibre. This hollow structure can easily be filled with either gaseous or liquid materials [31-34] by standard pumping techniques or just by using capillary or diffusion effects. In our case a commercial model HC-1550-02 from NKT Photonics was used, with a hollow core of approximately 11 μm in diameter ([35], figure 2-6). It was filled with acetylene gas using diffusion effects, described in more detail in the upcoming section 2.3.1.

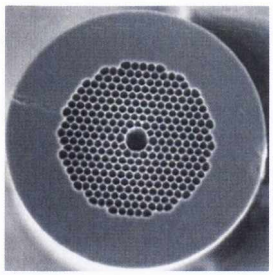

***Figure 2-6**: Cross-section of the HC-PBF utilised during our experimental research. The hollow structure was filled with acetylene using a diffusion effect. Taken from [35].*

2.2.5. TUNEABLE SEMICONDUCTOR LASER DIODES

Gas absorption spectra and NIR tuneable Laser Diodes.

As described in section 2.2.2, the absorbing transitions of acetylene targeted during the experimental work presented in this thesis lie within the NIR spectral region around 1.5 μm. Many environmentally important gases such as CO_2 or CH_4 are also active absorbers within such spectral range, so reliable laser sources operating at this wavelength scale are necessary to carry out sensing research. As pointed out during the thesis introduction, the laser diodes (LD's) developed by the optical communications industry in the last decades are ideal candidates in this respect. An optical telecommunication window was opened in 1977 centred at 1550 nm (the *C-band*), so much effort was made to improve the performance of laser sources working in this NIR region of interest. These affordable LD's fulfil the linewidth characteristics required for spectroscopic applications, their emission frequency can be tuned across a wide range of values and they exhibit a great flexibility when modulation techniques need to be applied. Many different types of tuneable LD's (TLD's) exist that fulfil our spectroscopic requirements, based on different laser structures and tuning mechanisms. Because this chapter serves as a general overview we will only point out here the global characteristics of the TDL's used during our experimental work. A detailed insight into the physics behind the wavelength tuning mechanisms and output linewidth characteristics of these lasers is presented later in the thesis, complementing the short introduction included here.

DFB and SG-DBR laser diodes

Two different types of TLD's were used during our experimental work, namely *SG-DBR (Sampled Grating Distributed Bragg Reflector)* and *SGC-DFB (Strongly Gain*

Coupled Distributed Feed Back) laser diodes. A very detailed treatment on tuneable laser sources by Buus [36] can be consulted for specific design and working principles applying to these LD's, while the main features relevant to basic gas sensing are presented in the following table 2-5:

Table 2-5 · NIR tuneable lasers used and main features

	SG-DBR (Sampled Grating Distributed Bragg Reflector)	SGC-DFB (Strongly Gain Coupled Distributed Feed Back)
WAVELENGTH RANGE (NM)	1535-1570	1537.5-1539.5
TUNING MECHANISM	Current	Current/Temperature

2.2.6. MODULATION DETECTION TECHNIQUES

In order to enhance the detection of the weak absorption signals of acetylene in the NIR region some high sensitivity techniques can be applied. Two different cases will be presented next, both of them based in the modulation of the emission wavelength of the laser diodes utilised. The first case corresponds to the so-called *Wavelength Modulation Spectroscopy* (WMS) technique, and has been extensively used during the experimental research for this thesis. The second case, known as the *Frequency Modulation Spectroscopy* (FMS) technique, has not been applied here but will be briefly summarised for it is related to some of the topics covered.

Wavelength Modulation Spectroscopy

In this first case, the emission wavelength of the laser source is modulated at frequencies smaller than the FWHM of the absorption profile (≈ kHz/MHz). Modulation is typically achieved using an external sinusoidal signal applied to the modulation facility of the current controller driving the laser. Following the treatment by Reid and Labrie in [37], the emission frequency therefore may be written as

$$\upsilon(t) = \bar{\upsilon} + a\cos\phi_m t \tag{2.19}$$

where $\bar{\upsilon}$ is the mean emission frequency, ϕ_m the angular modulation frequency and a the modulation amplitude. Because absorption is weak for the targeted gas transitions, the Beer-Lambert law presented in (2.8) can be approximated by the expression

$$\begin{aligned} I(\upsilon) &= I_0(\upsilon)[1 - \kappa(\upsilon)z_D] \\ &= I_0(\upsilon)\left[1 - \kappa\left(\bar{\upsilon} + a\cos\phi_m t\right)z_D\right] \end{aligned} \tag{2.20}$$

The time dependent term, periodic and even function, can be expanded in a cosine Fourier series

$$\kappa(\bar{\upsilon} + a\cos\phi_m t) = \sum_{n=0}^{\infty} H_n(\bar{\upsilon})\cos(n\phi_m t) \tag{2.21}$$

where $H_n(\bar{\upsilon})$ is the n^{th} Fourier component of the modulated absorption coefficient. The mean frequency is considered constant over a modulation period and the laser power assumed to remain constant while modulation occurs. Equation (2.21) essentially summarises the key aspect of this technique: demodulating the detected signal using a *Lock-In Amplifier* (LIA, [38, 39]) referenced at some multiple nf of the modulation frequency $f = \phi_m/2\pi$ makes the LIA output proportional to the n^{th} *Fourier*

component according to $I_0(\upsilon)H_n(\bar{\upsilon})z_D$. A detailed theoretical analysis shows that such components are dependent on the absorption lineshape or its derivatives, so the above discussion means that, in practice, the output of a demodulator referenced at the n^{th} multiple of the laser modulation frequency is proportional to the n^{th} derivative of the absorption profile. A simple, more intuitive way of understanding this important result is presented by Suplee et al in [40]. If the small absorption coefficient $\kappa(\upsilon) << 1$ in (2.20) is expanded into a Taylor series around the mean frequency $\bar{\upsilon}$ one gets

$$I(\upsilon) = I_0(\upsilon)\left[1 - z_D\left(\kappa(\bar{\upsilon}) + \left.\frac{d\kappa}{d\upsilon}\right|_{\bar{\upsilon}}(\upsilon - \bar{\upsilon}) + \frac{1}{2!}\left.\frac{d^2\kappa}{d\upsilon^2}\right|_{\bar{\upsilon}}(\upsilon - \bar{\upsilon})^2 \cdots\right)\right] \tag{2.22}$$

which using (2.19) and applying trigonometric identities can be rewritten as

$$\begin{aligned} I(\upsilon) = I_0(\upsilon)\Bigg[1 - z_D\Bigg(\kappa(\bar{\upsilon}) + \left.\frac{d\kappa}{d\upsilon}\right|_{\bar{\upsilon}} a\cos(\phi_m t) + \\ + \frac{1}{2!}\left.\frac{d^2\kappa}{d\upsilon^2}\right|_{\bar{\upsilon}} a^2\frac{1}{2}\cos(2\phi_m t)\cdots\Bigg)\Bigg] \end{aligned} \tag{2.23}$$

Only terms up to second order have been considered, as higher terms for the Taylor expansion rapidly decay according to the weighting amplitude factor a^n (the modulation amplitude a in WMS experiments is usually small compared to the FWHM of the targeted absorption feature). Thus, equation (2.23) explicitly reveals the proportionality between the first and second derivatives of the absorption coefficient κ and the components of the transmitted intensity demodulated at frequencies ϕ_m and $2\phi_m$, respectively. Note that the unique Fourier transform of the absorption coefficient in (2.21) is essentially the same as the Taylor expansion, because trigonometric identities allows for terms in consecutive frequencies $n\phi_m$ to be

grouped together. Figure 2-7 represents a typical schematic set-up when using this Lock-in detection technique.

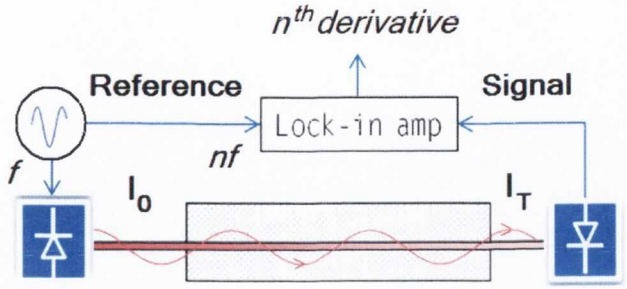

***Figure 2-7**: Schematic diagram for a WMS lock-in detection technique. The laser wavelength is modulated with a reference signal of frequency* f, *and the detected signal processed by a LIA referenced at a frequency* nf. *The output of the LIA is proportional to the* n^{th} *derivative of the transmitted intensity* I_T.

It can be demonstrated that the amplitude of the detected n^{th} harmonic signal depends on the amplitude a of the modulation signal, which in practice allows for optimization of the LIA output amplitude. Such optimization is applied in chapter 4 as an example, where we refer to the parameter a as the *modulation depth*. A particular advantage of this WMS detection technique is that any residual sloped background detected in direct transmission measurements is effectively suppressed, significantly improving the Signal-to-Noise Ratio (SNR) of the acquired data.

Frequency Modulation Spectroscopy

The second case is essentially based in the same principle as WMS, but only differs in the order of magnitude of the applied modulation frequency: In the FMS technique, the modulation frequency is much higher than the FWHM of the absorption line. The main effect of this high-frequency modulation is the appearance of several sidebands in the optical power spectrum of the laser source, separated from the carrier emission frequency v_0 by an amount exactly equal to the modulation frequency f. The number

of sidebands can be controlled by adjusting the modulation amplitude applied to the laser, with only the first sidebands typically considered. Several beat effects can occur between the sidebands and carrier peaks that may affect the detected signal, and must be assessed if some detailed information needs to be extracted. On the other hand, the main advantage of FMS detection is shifting the detection frequency to higher values where the low-frequency *1/f* noise affecting the laser is greatly reduced. However, the lock-in amplifier must be substituted by discrete high-frequency components which are more expensive and sensitive to external noise coupling. A detailed discussion on the origin and minimisation of such noise effects is included in chapter 4 of this thesis, where the topic of frequency stability in lasers is studied in detail. Formal analysis of both WMS and FMS techniques can be found in references [40, 41].

2.3. HOLLOW-CORE PHOTONIC BANDGAP FIBRE BASIC CHARACTERIZATION

After introducing the most important concepts related to basic gas sensing and laser spectroscopy during the previous sections, some experimental results will be presented here that characterize the basic behaviour of our system. Such characterization included the measurement of acetylene diffusion time into the HC-PBF, basic direct transmission and WMS gas sensing, and assessment of the broadening processes as a function of gas pressure. All of these investigations were essentially carried out under the same experimental set-up, tailored to each case and introducing minor changes when required. Figure 2-8 below schematically depicts the global experimental arrangement in the laboratory.

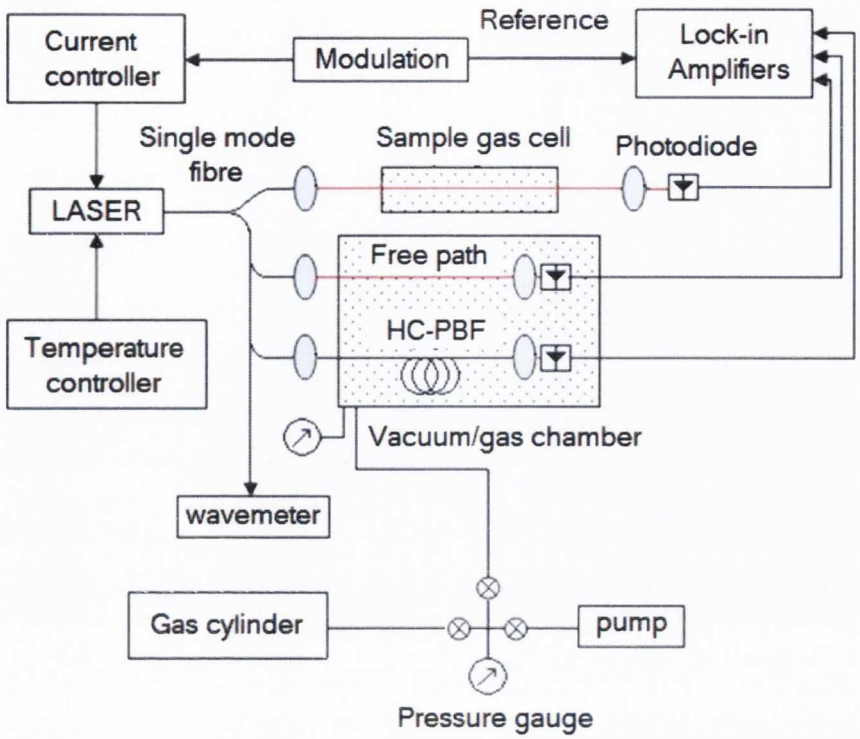

***Figure 2-8**: Schematic representation for the global set-up utilised during the basic characterization of the optical sensing system.*

As can be observed in the figure, the fiberised output from the laser (whose temperature and injection current are controlled by external units) can be split in four different paths using appropriate single mode fibres and splitters. One of the paths directly leads to a wavemeter to measure the emission wavelength when required. The second path is connected to a sealed sample gas cell containing selected mixtures of NH_3, HCN and $^{12}C_2H_2$, through which the laser beam travels before being detected by an InGaAs photodiode (PD). The third and fourth paths both enter a vacuum/gas chamber connected to an acetylene gas cylinder and turbo-molecular pump by means of appropriate valves (⊗). The gas pressure can be measured either using a high-accuracy ion pressure gauge directly connected to the chamber, or by using a secondary gauge connected to a subsidiary known volume. The ratio between the

subsidiary and chamber volumes (approximately 1:60) allows for specific amounts of acetylene to be injected within the gas/vacuum chamber when required. An additional needle valve is attached to the system if fine control of the pressure is required. The first path within the chamber is a free-space beam travelling across the absorbing gas and then detected using a PD located within the chamber. Light directed along the second chamber path is coupled into the HC-PBF and eventually collected using a second, independent PD. The output signal from the three PD signals can be fed to a lock-in amplifier that is set in a WMS detection fashion along with a modulation (voltage) source. Both the input/output ends of the HC-PBF and collimating lenses within in the chamber are set on precision translational stages allowing for fine alignment. This global set-up allowed us to perform all of the basic characterization experiments described next.

2.3.1. HC-PBF DIFFUSION TIME

In order to first analyse the diffusion properties of C_2H_2 into the PCF, the general gas sensing scheme presented in the previous section is slightly modified. Light from a SG-DBR source is directed along the two gas chamber paths. In the case of the free-space path the corresponding PD is substituted with an appropriate mirror at near-perpendicular incidence, so that laser light is reflected back out of the chamber through the same window and then collected using the former PD. This path serves as a *reference*, and is labelled accordingly. The second HC-PBF path is set in the same way as described earlier in section 2.3. Figure 2-9 schematically illustrates the arrangement

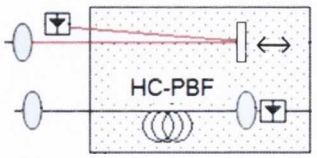

***Figure 2-9**: Modification of the experimental set-up for diffusion measurements. A mirror with variable position substitutes the former PD collecting the free path beam within the gas chamber. The PD is now placed external to the chamber, collecting the reflected light.*

In this double-path arrangement the absorption coefficient is the same for both beams, as they interact with the same gas concentration (pressure). However, the transmission along the reference path can be adjusted by tuning the mirror position until the absorbance A for both *channels* is the same,

$$\frac{I_i}{I_{oi}} = e^{-\alpha z_i}, \qquad A \equiv \alpha z_i, \qquad i = REF, PBF \tag{2.24}$$

Once this condition is fulfilled, we inject different concentrations of gas into the chamber and monitor the detected signals in time. Whereas the gas instantaneously fills the vacuum chamber and absorption remains stationary for the reference path, some diffusion time is required for the fibre to be filled: the transmission signal for the reference path corresponds to a fixed value, while the absorption in the HC-PBF exhibits an asymptotical behaviour. Corresponding results are presented in figure 2-10, where the observed ripples are attributed to mechanical alignment deviations.

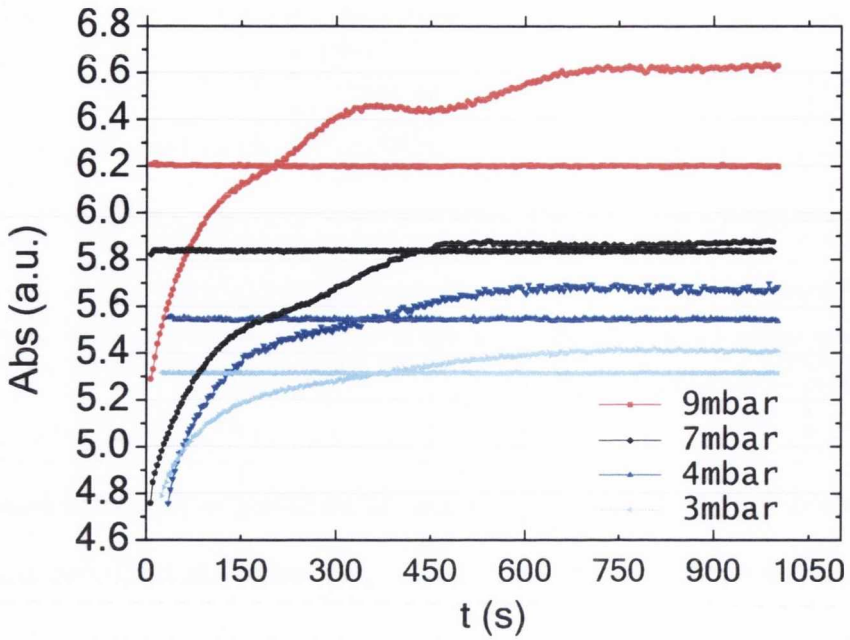

***Figure 2-10**: Results for the measurement of the HC-PBF gas diffusion time. At each pressure the reference absorption value remains constant (horizontal lines), while the corresponding fibre trace exhibits an asymptotical behaviour. When molecules have completely diffused within the fibre a steady state is reached.*

Diffusion time values for each pressure are extracted from the previous data by finding the time from which the difference between the reference and the PCF signals remains constant (within a 10% interval). Results are presented in table 2-6.

Table 2-6 · Measured HC-PBF acetylene diffusion times

P (mbar ±0.5)	t_{DIFF} *(s ±50)*
3.0	600
4.0	550
7.0	450
9.0	700

An average value of $t_{DIFF} \approx 10$ *min* extracted from these results will be taken as a reference. It is important to have an idea for the order of magnitude of the diffusion time, because it sets the lower limit for the time from which the molecular ensemble within the fibre will be at thermal *rest*. Gas temperature was kept constant at $T = 22$ $°C$ during the measurements.

2.3.2. HC-PBF WMS SENSING TEST

The basic gas sensing capability of HC-PBF's was examined by coupling the light from the SG-DBR LD into the fibre and then filling the gas chamber with 5 mbar of acetylene. To enhance the detection signal WMS techniques were applied and the operating LIA referenced to the second harmonic ($2f$) of the modulation frequency. The modulated laser wavelength was then tuned across a wide range, and the transmitted signal detected with a PD. Results for successful WMS detection of several acetylene absorption lines are presented in figure 2-11. Gas temperature is kept constant at a value of $T = 22$ $°C$, while the dominant broadening process at this pressure regime is the Gaussian-shaped Doppler contribution.

As is clear from the results presented in the figure, multiple gas lines are successfully detected using the WMS technique. Even small signals from weakly absorbing lines can be distinguished due to the SNR enhancement associated with this modulation technique. The particular shape of the 2f harmonics for selected gas lines around 1530 nm can be observed in the inset.

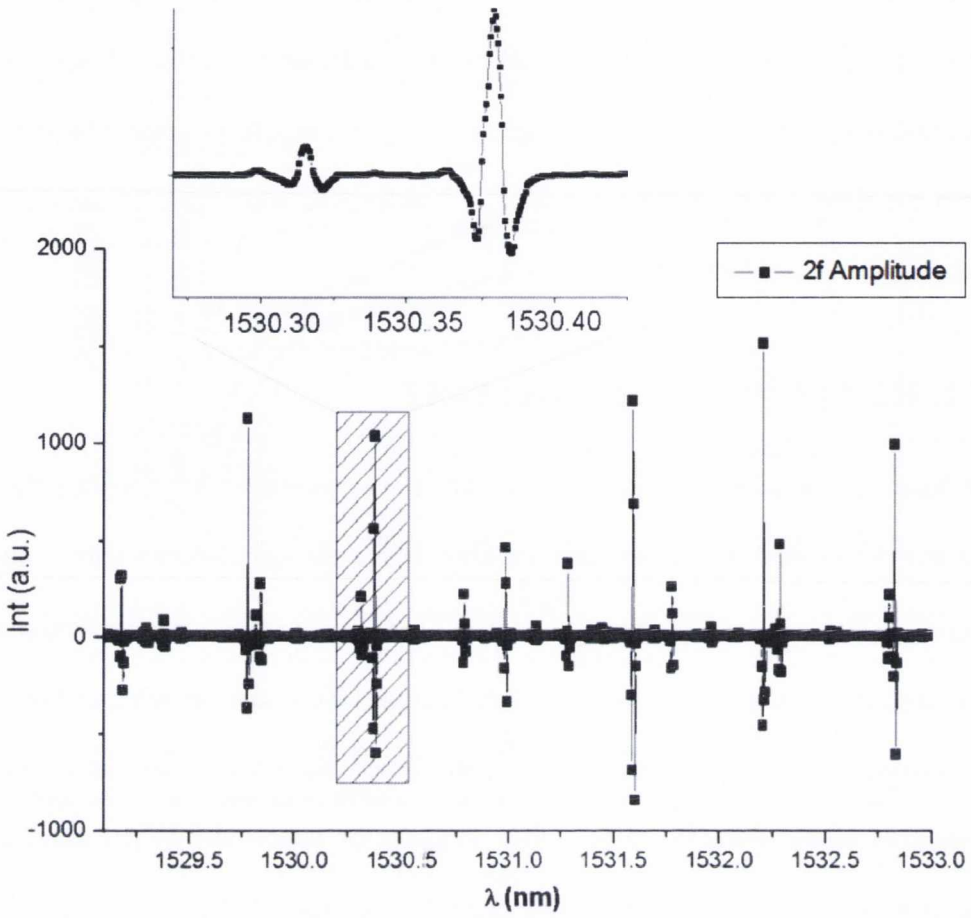

***Figure 2-11**: Results for the successful WMS detection of the second harmonic of multiple acetylene absorption lines. The gas is hosted within a HC-PBF, and the SGDBR wavelength tuned across an interval of more than 3nm. The particular 2f lineshape corresponding to selected transitions around 1530 nm can be observed in the inset.*

2.3.3. HC-PBF PRESSURE RESPONSE

In this case our aim was to investigate the spectral broadening response of the acetylene absorption line with pressure. In order to increase the gas pressure in the chamber without affecting the total absorption undergone by the laser beam, evaporated liquid nitrogen gas was leaked in. Nitrogen molecules are not active absorbers of the NIR light, so this ensures that the recorded absorption line for

acetylene will not change its shape because of concentration changes, but only due to foreign gas pressure broadening effects. In this case the laser light is split along the two paths within the gas chamber (HC-PBF and free space), while a system of vacuum valves allows for control of the nitrogen leaking rate. This rate must be slow enough to fill the HC-PBF in a quasi-stationary regime, so that pressure can be assumed to be constant for each scanned absorption line (individual scans take an approximate time of 1min). A precise needle valve is included in the leaking system to improve the control of the leaking rate, which is measured to be $dp/dt \approx 4/60$ *mbar/min.* This nitrogen leaking rate is much slower than the average acetylene diffusion rate into the fibre of $dp/dt \approx 36/60$ *mbar/min* calculated from the measured diffusion time. The system is left for several hours and direct transmission signals acquired. The targeted absorption line was centred at $\lambda_0 = 1539.42$ *nm* and gas temperature kept at $T = 22$ *°C.*

As described in section 2.2.3, several mechanisms contribute to the final linewidth of the acquired transmission signal. In order to extract the individual components, theoretical fits of the experimental data to a Voigt profile are performed. The output of such theoretical fitting yields two different values, namely the homogeneous linewidth $\Delta\upsilon_{HOM}$ and the inhomogeneous linewidth $\Delta\upsilon_{INHOM}$. Results for the homogeneous component of the total broadening are presented in figure 2-12, while the extracted inhomogeneous component due to the Doppler effect is in very good agreement with the theoretical value calculated using equation (2.14):

$\Delta\nu_D$ (theory) = *470 MHz*
$\Delta\nu_D$ (experimental) = *462 MHz*

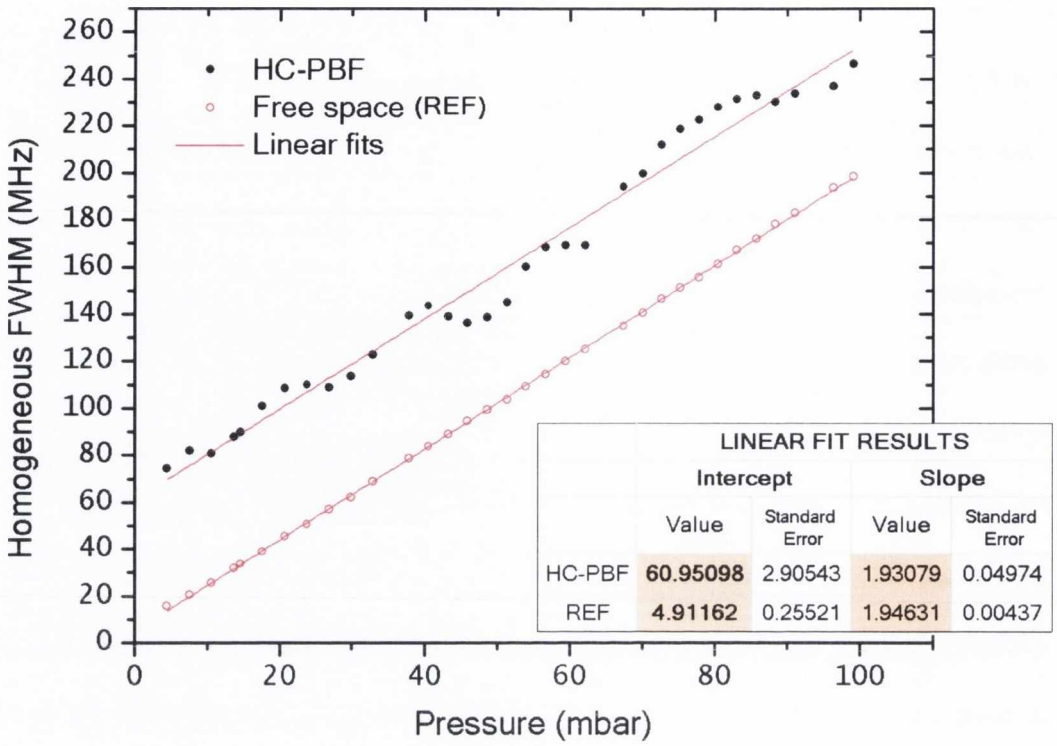

Figure 2-12: *Homogeneous broadening component of the total FWHM of the selected acetylene absorption line against gas pressure hosted in the HC-PBF. Data have been obtained after fitting the recorded absorption line to a Voigt profile and each of the two traces independently fit to a straight line.*

Analysis of the presented results for the homogeneous FWHM component yields several interesting points. First of all, our assessment of the theoretical linear increase of the collisional broadening with increasing gas pressure is clearly backed up by the fitted results: Both the HC-PBF and reference path linewidths increase linearly as gas is leaked into the system. Theoretical linear fits are performed, with an average slope for both the free space and fibre paths of $\Delta\upsilon/\Delta P \approx 2$ *MHz/mbar*. Because the acetylene absorption line is broadened due to the pressure introduced by a different gas, this parameter is commonly referred to as the *foreign gas broadening coefficient*. A detailed analysis reported by Minutolo et al. [42] for the same acetylene absorption line and nitrogen foreign gas yields a value for this coefficient of $\Delta\upsilon/\Delta P \approx 2.06$

MHz/mbar, confirming the validity of our analysis. The ripples observed in the fibre trace are attributed to low-frequency mechanical noise affecting the laser-fibre coupling, thus affecting the single-mode guidance of the fibre as mentioned in section 2.2.4.

On the other hand, a constant difference can be observed between the fibre and reference linewidths at all pressures (i.e. two *parallel lines* are observed). Because the HC-PBF trace exhibits a larger homogeneous value for the total linewidth, this means that an extra broadening component is affecting the gas molecules within the fibre core. According to discussion in section 2.2.4 such additional broadening is attributed to the transit-time effect, so an estimation can be made according to relation (2.18) and then compared to the experimental value extracted from the previous figure. The assumption is made that acetylene molecules cross a Gaussian beam of 1/e intensity diameter $d = 7.5\ \mu m$ [35] with a three-dimensional (3D) mean molecular velocity $v_{3D} = \sqrt{(8RT/\pi M)} = 490.3\ ms^{-1}$ at a temperature of $T = 22°C$, and a corrected two-dimensional (2D) velocity of $v_{2D} = \sqrt{(\frac{2}{3})}v_{3D} = 400.3\ m\ s^{-1}$ (this correction is introduced because the transit-time broadening is calculated with respect to any direction perpendicular to the fibre axis). The final results for both the theoretical and experimental estimations correspond to

$\Delta\nu_{TT}$ **(theory)** $\approx$ ***40 MHz***
$\Delta\nu_{TT}$ **(experimental)** $\approx$ ***56 MHz***

Some difference exists between the two final results, though both estimations are of the same order of magnitude and agree within experimental and theoretical error. The observed ripples along the HC-PBF trace suggest that the coupling of light into the

fibre could be further optimized, eventually improving the fitting accuracy and the final results.

2.4. CONCLUSIONS

The basic theoretical background regarding laser-based gas sensing in Hollow-Core Photonic Bandgap Fibres has been discussed in this chapter. The main laws governing linear absorption of laser light by a gaseous medium have been stated, putting some emphasis on the characteristics of our particular laboratory system that affects the broadening processes . The main properties of HC-PBF's and laser sources utilised during experimental work and relevant to spectroscopic-based gas sensing have been presented, as well as an insight into the detection techniques utilised to enhance the achievable sensitivity limit. Experimental results have been presented to back up the theoretical approach, successfully characterizing some of the HC-PBF properties relevant to our research work. Therefore this facilitates the understanding and preparation of more complex experimental set-ups, and allows us to investigate different aspects of laser-diode based gas sensing as presented in upcoming chapters.

2.5. REFERENCES

1. W. Demtröder, *Laser Spectroscopy: Basic Concepts and Instrumentation, 2Ed* (Springer, 1996).

2. P. P. Garrett, "Absorption and Transmission of light and the Beer-Lambert Law," (2006), http://www.physics.uoguelph.ca/~pgarrett/teaching/PHY-1070/lecture-21.pdf.

3. R. M. Measures, "Chapter 3: Infrared Laser Absorption: Theory and Applications," in *Laser Remote Chemical Analysis*, J. D. Winefordner, ed. (John Wiley & Sons, 1988).

4. J. I. Steinfeld, *Molecules and Radiation: An Introduction to Modern Molecular Spectroscopy, p. 245-248* (Dover Reprint Edition, 2005).

5. C. N. Banwell, and E. M. McCash, *Fundamentals of Molecular Spectroscopy* (McGraw-Hill, 1994).

6. V. Weldon, "Spectroscopic Based Gas Sensing Using Tuneable Diode Lasers," in *Encyclopedia of Sensors*, C. A. Grimes, E. C. Dickey, and M. V. Pishko, eds. (American Scientific Publishers, 2005).

7. G. Herzberg, *Infrared and Raman Spectra of Polyatomic Molecules* (D. Van Nostrand Company, Inc, 1945).

8. J. Elijah Kannatey-Asibu, "Broadening mechanisms," in *Principles of Laser Materials Processing*, J. W. Sons, ed. (2009), pp. 90-92.

9. V. S. Letokhov, and V. P. Chebotayev, *Nonlinear Laser Spectroscopy* (Springer-Verlag, 1977).

10. R. M. Measures, *Laser Remote Chemical Analysis* (John Wiley & Sons, 1988).

11. K. Shimoda, *High-Resolution Laser Spectroscopy, Ch.2, pp. 12-14* (Springer-Verlag, 1976).

12. S. Stenholm, *Foundations of Laser Spectroscopy* (John Wiley & Sons, 1984).

13. H. Walter, *Laser Spectroscopy of Atoms and Molecules* (Springer-Verlag, 1976).

14. O. Svelto, *Principles of Lasers 4th Ed., Ch. 2, pp. 44-45* (Springer, 1998).

15. W. Demtröder, "3.4. Transit-Time Broadening," in *Laser Spectroscopy: Basic Concepts and Instrumentation, 2Ed*(Springer, 1996).

16. C. R. Nave, "Kinetic Theory," (Department of Physics and Astronomy, Georgia State University, 2005), http://hyperphysics.phy-astr.gsu.edu/hbase/Kinetic/kinthe.html2009.

17. M. Lepère, "Line profile study with tunable diode laser spectrometers," Spectrochimica Acta Part A: Molecular and Biomolecular Spectroscopy **60**, 3249-3258 (2004).

18. P. L. Varghese, and R. K. Hanson, "Collisional narrowing effects on spectral line shapes measured at high resolution," Appl. Opt. **23**, 2376-2385 (1984).

19. J. D. Joannopoulos, *Photonic crystals : molding the flow of light* (Princeton University Press, Princeton, 2008).

20. T. A. Birks, P. J. Roberts, P. S. J. Russell, D. M. Atkin, and T. J. Shepherd, "Full 2-D photonic bandgaps in silica/air structures," Electronics Letters **31**, 1941-1943 (1995).

21. F. Benabid, G. Bouwmans, J. C. Knight, P. S. J. Russell, and F. Couny, "Ultrahigh Efficiency Laser Wavelength Conversion in a Gas-Filled Hollow Core Photonic Crystal Fiber by Pure Stimulated Rotational Raman Scattering in Molecular Hydrogen," Physical Review Letters **93**, 123903 (2004).

22. J. B. Jensen, J. Riishede, J. Broengx, J. Laegsgaard, T. Tanggaard Larsen, T. Sorensen, K. Hougaard, E. Knudsen, S. B. Libori, and A. Bjarklev, "Photonic crystal fibers; fundamental properties and applications within sensors," in *Sensors, 2003. Proceedings of IEEE*(2003), pp. 269-278 Vol.261.

23. J. C. Knight, "Photonic crystal fibres," Nature **424**, 847-851 (2003).

24. D. G. Ouzounov, F. R. Ahmad, D. Muller, N. Venkataraman, M. T. Gallagher, M. G. Thomas, J. Silcox, K. W. Koch, and A. L. Gaeta, "Generation of Megawatt Optical Solitons in Hollow-Core Photonic Band-Gap Fibers," Science **301**, 1702-1704 (2003).

25. P. S. J. Russell, "Photonic-Crystal Fibers," Lightwave Technology, Journal of **24**, 4729-4749 (2006).

26. J. Tuominen, T. Ritari, H. Ludvigsen, and J. C. Petersen, "Gas filled photonic bandgap fibers as wavelength references," Optics Communications **255**, 272-277 (2005).

27. F. Benabid, F. Couny, J. C. Knight, T. A. Birks, and P. S. J. Russell, "Compact, stable and efficient all-fibre gas cells using hollow-core photonic crystal fibres," Nature **434**, 488-491 (2005).

28. S. Konorov, A. Zheltikov, and M. Scalora, "Photonic-crystal fiber as a multifunctional optical sensor and sample collector," Opt. Express **13**, 3454-3459 (2005).

29. T. Ritari, H. Ludvigsen, and J. C. Petersen, "Photonic Bandgap Fibers in Gas Detection," Spectroscopy **20**, 30-34 (2005).

30. T. Ritari, J. Tuominen, H. Ludvigsen, J. Petersen, T. Sørensen, T. Hansen, and H. Simonsen, "Gas sensing using air-guiding photonic bandgap fibers," Opt. Express **12**, 4080-4087 (2004).

31. J. M. Fini, "Microstructure fibres for optical sensing in gases and liquids," Measurement Science and Technology, 1120 (2004).

32. Y. L. Hoo, W. Jin, H. L. Ho, and D. N. Wang, "Measurement of gas diffusion coefficient using photonic crystal fiber," Photonics Technology Letters, IEEE **15**, 1434-1436 (2003).

33. Y. L. Hoo, W. Jin, C. Shi, H. L. Ho, D. N. Wang, and S. C. Ruan, "Design and Modeling of a Photonic Crystal Fiber Gas Sensor," Appl. Opt. **42**, 3509-3515 (2003).

34. K. Nielsen, N. Danny, S. Thorkild, B. Anders, and P. H. Theis, "Selective filling of photonic crystal fibres," Journal of Optics A: Pure and Applied Optics, L13 (2005).

35. NKT photonics, "HC-1550-02 fibre datasheet," http://www.nktphotonics.com/side5334.html.

36. J. Buus, M. C. Amann, and D. J. Blumenthal, *Tunable Laser Diodes and Related Optical Sources* (Wiley-IEEE Press 2005).

37. J. Reid, and D. Labrie, "Second-harmonic detection with tunable diode lasers — Comparison of experiment and theory," Applied Physics B: Lasers and Optics **26**, 203-210 (1981).

38. "Lock-In Amplifier," (Bentham Electronics), http://www.bentham.co.uk/pdf/F225.pdf2009.

39. H. S. John, "Frequency-domain description of a lock-in amplifier," American Journal of Physics **62**, 129-133 (1994).

40. J. M. Supplee, E. A. Whittaker, and W. Lenth, "Theoretical description of frequency modulation and wavelength modulation spectroscopy," Appl. Opt. **33**, 6294-6302 (1994).

41. J. A. Silver, "Frequency-modulation spectroscopy for trace species detection: theory and comparison among experimental methods," Appl. Opt. **31**, 707-717 (1992).

42. P. Minutolo, C. Corsi, F. D. Amato, and M. D. Rosa, "Self- and foreign-broadening and shift coefficients for C2H2 lines at 1.54 um," The European Physical Journal D **17**, 175-179 (2001).

CHAPTER 3

NONLINEAR GAS SENSING: SINGLE AND DOUBLE SATURATION

3.1. INTRODUCTION

In the previous chapter the basis for laser-based gas sensing experiments in Hollow-Core PBF's [1, 2] was established. A Description of the main laser sources paying attention to their most important features regarding spectroscopy has been introduced, and the main types of semiconductor laser diodes used in our experimental work. The structure and working principle of HC-PBF's has been examined and several features specific to this type of fibres discussed. A description of the gaseous absorbing species used in our experimental work has been introduced from a molecular point of view, and absorption laws in the linear regime clearly stated. The diffusion properties, gas sensing capability and pressure response of HC-PBF's have been demonstrated corresponding to the linear absorption regime. However, the same hollow-core fibres can be used in experimental work under a nonlinear absorption regime. As light is trapped and focused inside the hollow, micrometer-scale core of the microstructured fibres, the intensity of the optical field is significantly increased across the absorbing volume. This feature, in addition to the long optical paths in small physical space provided by PBF's (bend losses are minimum as light guidance is not based on TIR so

long lengths of fibre can be coiled requiring minimum space), gives rise to and makes these fibres a perfect candidate for the study of nonlinear effects. A particular phenomenon occurs when the intensity of the incoming radiation field is increased and the molecular populations of the energy levels involved in the absorbing transition are significantly modified: the pumping rate overcomes the effective relaxation rate for the transition so that it becomes *saturated.* The direct effect of such saturation is a decrease in the absorption of any further light directed across the absorbing sample. Exploitation of this effect making use of suitable experimental schemes makes it possible to study fine spectral details in the otherwise Doppler-broadened absorption profile. The significant reduction in the spectral widths of the saturation features (typically tens of MHz at few mbars of pressure) compared to the Doppler-broadened profiles (typically hundreds of MHz at the same pressure values) has immediate consequences in high-accuracy frequency applications.

Saturation spectroscopy for several gas species such as acetylene, ammonia or hydrogen cyanide has been investigated in these microstructures [3-5]. Application to wavelength referencing and integration of PBF fibres into portable systems has been studied and demonstrated [6, 7]. In particular, the application of acetylene is of special interest due to its well-defined absorption spectrum in the 1.5 μm spectral region, with regularly spaced absorption lines over a range of tens of nanometres [8-10]. Several studies have been carried out addressing the influence of parameters such as the optical power and gas pressure on the linewidth of saturated transitions, together with the effect of the fibre geometry [11-14]. In this chapter the saturated absorbing properties of acetylene are first investigated and compared with corresponding results from several previous studies. Saturation effects are achieved utilising high-power laser diodes readily available from industry, which fulfil the linewidth specifications

necessary for laser spectroscopy research (low output linewidth) and exhibit good versatility to apply modulation techniques as compared to other types of laser sources (this is very important for example in order to implement frequency stability schemes, as presented in next chapter). Based on our experimental results a novel experimental approach is suggested. Simultaneous saturation of an absorbing transition at two different wavelengths is demonstrated, based on modulation of the laser frequency and non-resonant effects in a three-level molecular system. The simple yet powerful modification of the experimental scheme significantly improves the accuracy of the extracted saturation results. Potential applications are discussed and the link with stabilization of the emission frequency of lasers is introduced, a topic discussed in detail in the following chapter.

3.2. BACKGROUND

3.2.1. NONLINEAR ABSORPTION: SATURATION

When a light beam of angular frequency ω travels through an absorbing medium, the intensity of the beam decreases exponentially with distance according to Beer's law as discussed in chapter 2,

$$I = I_0 e^{-\alpha(\omega)z} \tag{3.1}$$

where $\alpha(\omega)$ is the absorption coefficient and z the distance travelled across the absorbing medium. This is true at sufficient low intensities and absorption paths, with the relative change of intensity dI/I over a distance dz being constant and equal to $\alpha(\omega)$.

However, if the intensity of the incoming beam exceeds a certain value this law is no longer valid and a new approach is required. Assume an open two-level system with absorbing molecules being excited from a ground energy level 1 to an upper energy level 2. The system is referred to as *open* because it is assumed that the optical pumping occurs only between those two levels even if they may decay into other levels. The number of molecules excited to the upper level is proportional to the optical pumping rate P, while the relaxation to the ground level is determined by the average relaxation rate $<R>$. The *saturation parameter* S is defined as the ratio between these two rates, and its value is useful to distinguish between different absorption regimes. In the linear case the intensity of the radiation field I is small and the population difference between levels 1 and 2 is independent of I (i.e., the relative absorbed power dP/P is constant). However, if the intensity is high enough so that the excitation rate overcomes the relaxation processes then the populations of the absorbing levels are significantly modified and the spectral absorption profile is changed. The intensity $I = I_S$ at which the saturation parameter becomes $S = 1$ is called the *saturation intensity*. The *saturation power* is $P_S = I_S A$, where A is the cross section of the laser beam at the absorbing molecular sample. The exact change in the absorption profile depends on the specific experimental conditions and broadening processes affecting the transition so a brief summary will be included in this section including the most important concepts and relationships. The comprehensive analysis found in Demtröder [15] will be followed, where the usual convention of using the angular frequency $\omega = 2\pi \upsilon$ is used to avoid factors of 2π in the equations. An advanced nonlinear treatment can be found in Letokhov and Chebotayev [16].

Saturation of a homogeneous broadened profile

In the case of a set of atoms at rest in the observer's coordinate system, the absorption coefficient in the neighbourhood of a molecular transition frequency ω_0 is given by a Lorentzian function

$$\alpha_0(\omega) = \frac{2\hbar B_{12}\Delta N_0}{\pi c\gamma}\frac{(\Delta\omega/2)^2}{(\omega-\omega_0)^2+(\Delta\omega/2)^2} \tag{3.2}$$

where $\Delta\omega$ is the Full Width at Half Maximum FWHM of the absorption profile. The coefficient B_{12} is the *Einstein coefficient of induced absorption* and the quantity $\Delta N_0 = N_{10} - N_{20}$ the unsaturated population difference between the ground and excited levels 1 and 2. When the pump rate of the transition $P=B_{12}\rho(\omega)$ ($\rho(\omega)$ being the spectral energy density of the radiation field) increases and the relaxation rate is overcome then the absorption coefficient can be rewritten in the form

$$\alpha_S(\omega) = \alpha_0(\omega_0)\frac{(\Delta\omega/2)^2}{(\omega-\omega_0)^2+(\Delta\omega_S/2)^2} = \frac{\alpha_0(\omega)}{1+S_\omega} \tag{3.3}$$

with the frequency-dependent saturation parameter S_ω given by

$$S_\omega(\omega) = \frac{B_{12}\rho(\omega)}{\langle R\rangle}L(\omega-\omega_0) \tag{3.4}$$

This parameter represents the ratio between the pump and average relaxation rates, and in the case of a homogeneously broadened line it follows a Lorentzian shape $L(\omega-\omega_0)$ given by

$$L(\omega - \omega_0) = \frac{Ne^2\pi}{4\epsilon_0 mc} \frac{\Delta\omega_N/2\pi}{(\omega_0 - \omega)^2 + (\Delta\omega_N/2)^2} \tag{3.5}$$

This expression corresponds to the Kramers-Kronig relation for the absorption of an oscillator with mass m and number volume density N [17], with $\Delta\omega_N$ being the natural linewidth of the absorbing transition. Thus, the effect of the saturation in a homogeneously broadened profile is to decrease the unsaturated absorption coefficient $\alpha_0(\omega)$ by a factor of $(1+S_\omega)$. The saturation power is bigger at the line centre than at the wings according to (3.4) and (3.5) because the absorbed power is bigger there. This means that the change in the absorption coefficient is bigger at the line centre than at the wings. The result is that the lineshape for the saturated absorption coefficient is broadened with respect to the unsaturated case, as shown in figure 3-1 below. The saturated coefficient $\alpha_S(\omega)$ still follows a Lorentzian lineshape but the linewidth is now $\Delta\omega_S = \Delta\omega(1+S_0)^{1/2}$. In the weak-field approximation ($S_0 << 1$) the saturated linewidth can be approximated by $\Delta\omega_S \approx \Delta\omega$.

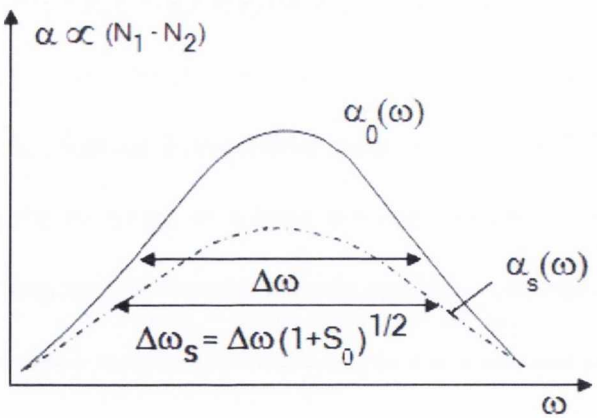

***Figure 3-1**: Schematic illustration for the saturation of a Lorentzian homogeneously broadened line by a high intensity laser. The unsaturated absorption coefficient $\alpha_0(\omega)$ is broadened, resulting in a saturated coefficient $\alpha_S(\omega)$ with a Lorentzian profile and linewidth $\Delta\omega_S = \Delta\omega(1+S_0)^{1/2}$ (figure adapted from [15]).*

Saturation of an inhomogeneous broadened profile

In the case of a set of atoms possessing some thermal motion the absorption coefficient is broadened from its homogeneous value due to the Doppler effect. When the Doppler broadening is much bigger than the homogeneous width (which is our case for example, at gas pressures of few mbar and Doppler widths of the order of hundreds of MHz) the intensity profile of such an absorbing line is given by a Gaussian profile

$$I(\omega) = I_0 \exp\left(-\frac{(\omega-\omega_0)^2}{0.36\Delta\omega_D{}^2}\right) \tag{3.6}$$

around a molecular transition at a frequency ω_0. The full width at half maximum (FWHM) depends on the atom/molecule mass m and temperature T and is given by $\Delta\omega_D = (2\omega_0/c)(2(\ln 2)kT/m)^{1/2}$. A more rigorous analysis shows that the real lineshape is a mixture between a pure Gaussian and a pure Lorentzian lineshape and is referred to as *Voigt* profile, already discussed in chapter 2.

When the intensity of the radiation field is increased and significant saturation occurs the effect is different than in the homogeneous case. Here the frequency of the radiation in the frame of a molecule with speed **v** becomes $\omega' = \omega - \mathbf{kv} = \omega - kv_z$ due to the Doppler effect, $k=k_z$ being the propagation constant of the incoming field. A detailed analysis shows that molecules are excited within the interval $dv_z = \Delta\omega/k$ centred at $v_z = (\omega - \omega_0)/k$, so that a so-called *Bennet hole* is created in the velocity distribution of the ground level $N_1(v_z)$ and a correspondent peak appears in the upper level distribution $N_2(v_z)$. This situation is illustrated in figure 3-2. The linewidth of this dip is $\Delta\omega_s = \Delta\omega(1+S_0)$, and the depth at its centre is $\Delta N_0(v_z) - \Delta N(v_z) = \Delta N_0(v_z)S_0/(1+S_0)$.

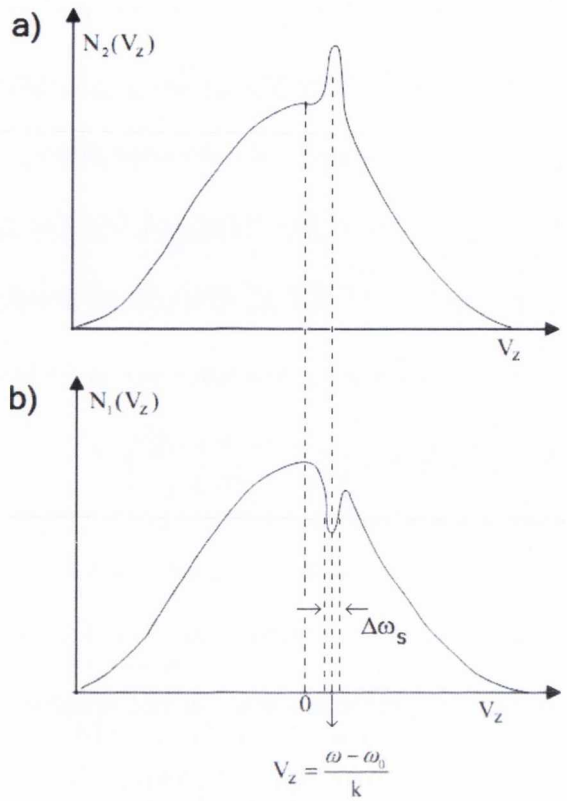

***Figure 3-2**: Schematic diagram for the saturation of an inhomogeneously broadened line. (a) A* Bennet hole *is created in the velocity distribution of the ground level* $N_1(v_z)$. *(b) A correspondent peak is created in the upper level distribution* $N_2(v_z)$ *(figure adapted from [15]).*

A detailed analysis shows that in the usual weak field approximation $S_0<<1$ the absorbing coefficient still follows a Voigt profile, this time reduced by the frequency-independent factor $(1+S_0)^{1/2}$:

$$\alpha_S(\omega) = \frac{\alpha_0(\omega_0)}{\sqrt{1+S_0}} \exp\left(-\frac{(\omega-\omega_0)^2}{0.36\Delta\omega_D{}^2}\right) \tag{3.7}$$

Thus, even if a Bennet hole is created at each frequency ω by the strong beam, it **cannot** be detected just by tuning that frequency around the absorption line centre: two lasers are needed to observe the change in absorption due to saturation effects (a special case is that of a single laser reflected back through the absorbing medium, as explained elsewhere in this section).

1. A strong ***pump*** laser, wave vector $\boldsymbol{k_1}$ at frequency ω_1 burns a hole in velocity class $v_z \pm \Delta v_z/2$ with $v_z = (\omega_0 - \omega_1)/k_1$ and $\Delta v_z = \Delta\omega/k_1$, as discussed above.
2. A weak ***probe*** laser, wave vector $\boldsymbol{k_2}$ and tuneable frequency ω across the Voigt profile. No interference with the pump is assumed due to its weak optical power.

Calculations lead to the following result for the saturated absorption coefficient

$$\alpha_S(\omega_1, \omega) = \alpha_0(\omega)\left[1 - \frac{S_0}{\sqrt{1+S_0}}\frac{(\Delta\omega/2)^2}{(\omega - \omega')^2 + (\Gamma_S/2)^2}\right] \tag{3.8}$$

which corresponds to an unsaturated Doppler profile $\alpha_0(\omega)$ with a saturation dip of Lorentzian shape at a frequency

$$\omega' = \omega_0 \pm (\omega_1 - \omega_0)k_1/k_2 \tag{3.9}$$

The signs ± hold respectively for co- or contra-propagating beams, while the linewidth of the absorption dip $\Gamma_S = \Delta\omega + \Delta\omega_S = \Delta\omega\,[1+(1+S_0)^{1/2}]$ equals the sum of

the saturated dip width $\Delta\omega_S$ due to the pump plus the unsaturated absorption width $\Delta\omega$. Figure 3-3 illustrates these results.

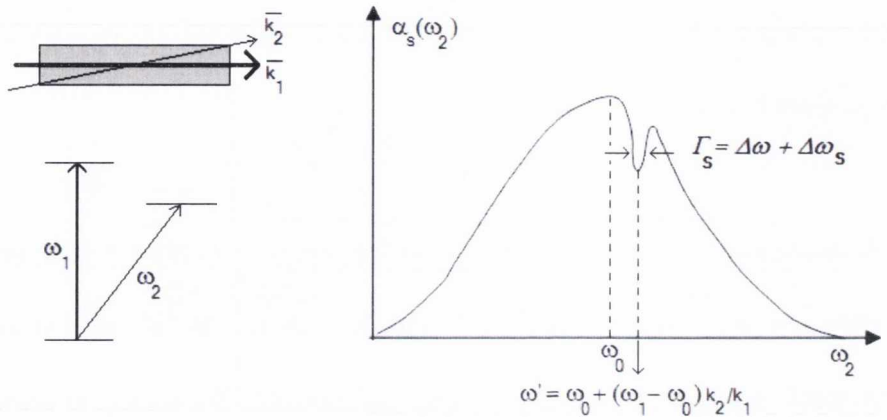

***Figure 3-3**: Schematic diagram for the saturation of an inhomogeneously broadened line using two lasers. A strong pump beam of frequency and wave vector (ω_1 , k_1) saturates the transition, while the frequency ω_2 of a weak probe laser (ω_2 , k_2) is tuned across the absorption line centred at ω_0. A saturation hole of linewidth Γ_S is detected in the spectral absorption profile of the probe at a frequencyω' (figure adapted from [15]).*

A special case is that where the only laser used is the strong pump, but is reflected back after travelling through the absorbing medium so that the counter-propagating wave acts as the probe. A detailed analysis can be found again in Demtröder [15], but we will restrict the analysis here to the case which matches our experimental description in section 3.3: the saturating wave is kept at the absorption line centre $\omega = \omega_0$ and a weak probe beam is tuned across the line profile. In such case, the absorption coefficient is given by

$$\alpha_S(\omega) = \alpha_0(\omega)\left[1 - \frac{S_0}{2}\frac{(\Delta\omega_S/2)^2}{(\omega - \omega')^2 + (\Delta\omega_S/2)^2}\right] \qquad (3.10)$$

This represents the unsaturated Doppler broadened profile $\alpha_0(\omega)$ with a Lorentzian dip of linewidth $\Delta\omega_S \approx \Delta\omega$ at the line centre and is valid in the weak field approximation $S_0 << 1$. The dip in the absorption profile is usually referred to as the *Lamb* dip. Figure 3-4 below illustrates a global comparison of the different saturation regimes described here, with the last case included in figure 3-4(c).

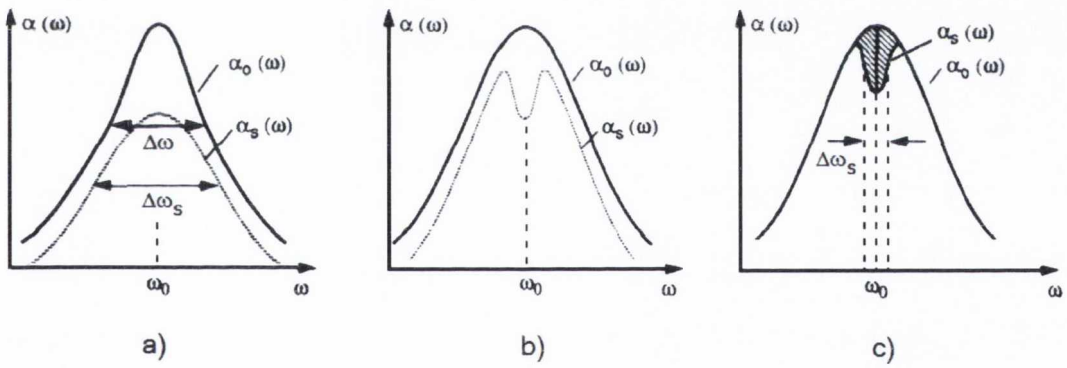

***Figure 3-4**: Comparison of different saturation regimes. (a) Pump laser tuned across a homogeneously broadened absorption line. (b) Two counter-propagating waves coming from a single pump laser tuned across an inhomogeneously broadened absorption line. (c) The pump frequency is fixed at the centre of an inhomogeneously broadened line while the frequency of a second weak probe laser is scanned across (figure adapted from [15]).*

3.2.2. RESONANT AND NON-RESONANT TRANSITIONS

The above discussion is limited to the case where the pump and probe laser frequencies ω_1 and ω_2 are either fixed or tuned across the vicinity of a two-level molecular absorbing transition at a frequency ω_0. If the pump frequency is kept at the line centre a Lamb dip is created at that point and detected by the weak probe when its frequency is resonant with ω_0. However, such an effect is not unique to a resonant scheme but can be extended to a three-level molecular system in a non-resonant fashion. Under some specific circumstances, the absorption of the probe laser around a transition at a frequency ω_0 can be decreased by means of a strong pump laser targeting a frequency ω_{PUMP} far away from that of the probe. Such a phenomenon is referred to as *Electromagnetically Induced Transparency* (EIT) [18-20] and is based on coherent population trapping [21], a quantum coherence effect in 3-level systems which usually requires a detailed quantum mechanical treatment. EIT effects have been experimentally demonstrated in several types of atomic systems, but in our case we will restrict the analysis to the gaseous case pointing out the key features important to our experimental purposes.

The first point is related to the rotational-vibrational absorption spectrum of a linear molecule such as acetylene. Figure 3-5 illustrates some possible rotational transitions between two vibrational states v and v' in a parallel band of such a molecule [11]. Rotational absorption lines to the low-frequency side of the band centre ω_0 correspond to an increment of the rotational quantum number of $\Delta J = -1$ and are referred to as the *P branch*, while those to the high-frequency side with $\Delta J = +1$ form the *R branch* [22]. In the illustrated example the pump laser is tuned into resonance with the transition $P(J+1)$ of the figure, modifying its population densities in a similar fashion

than described in the previous section. The question at this stage is how to detect such saturation effect with a probe targeting an absorbing transition in the *R*-branch, which can be tens of nanometres away: only certain combinations of non-resonant *P* and *R* transitions will give rise to EIT effects.

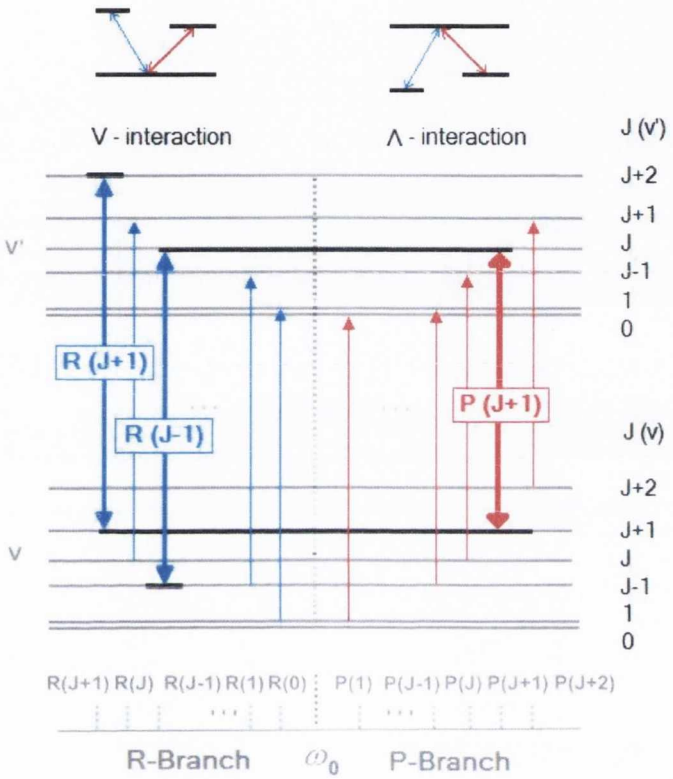

***Figure 3-5**: Rotational transitions between two vibrational states* v *and* v' *in a parallel band of a linear molecule such as acetylene. Non-resonant EIT effects only occur under the pump-probe combinations P(J+1)-R(J+1)* (V-type) *or P(J+1)-R(J-1)* (Λ-type). *Figure adapted from [11].*

The solution comes from the corresponding theoretical analysis and is graphically shown in the figure above: only those transitions in the *R-branch* sharing either the ground or the upper level with the saturating transition *P(J+1)* will allow for EIT. Combinations of the form *P(J+1) – R(J-1)* sharing the upper level are referred to as a

Λ-type interactions (the corresponding transition diagram has a "*Λ*" shape, as shown in figure 3-5 above), while schemes of the form *P(J+1) – R(J+1)* sharing the ground level are known as *V-type* interactions (the transition diagram has a "*V*" shape in this case, again shown in figure 3-5 above). The present discussion is valid for any line targeted by the pump laser within the P branch, making it possible to study saturation effects over a wide frequency range.

In practice, this means that the saturation effects described in the previous section can be detected by a probe laser scanning either of the *R(J±1)* transitions. This non-resonant scheme will be used in our case, as it minimises any possible interference between the pump and probe beams shifting any beat signal to high frequencies. Theoretical analysis to compare experimental results with the expected values can be either performed following any of the two saturation/EIT approaches. The saturation approach will be used in our case when analysing the recorded data, though the results reported by Benabid et al. following an EIT approach [11] are also in good agreement with the results to be presented.

3.2.3. THE PUMP-PROBE EXPERIMENT

The physical basis for the saturation of an absorbing transition has been described at this stage. In this section a general overview of the experimental arrangements most commonly implemented by research groups to perform saturation experiments is included, complementing the theoretical approach. Details for the specific arrangements implemented during our experimental work are included in section 3.3.

The most extended experimental scheme to perform saturation experiments is known as the ***pump-probe*** scheme, and involves the use of two laser beams as the name suggests. As discussed in section 3.2.1 the first beam is known as the ***pump***, and

corresponds to the laser providing the high optical power responsible for saturation. It is operated in a cw fashion and gives rise to molecular population modifications and saturation of the absorbing transition. A high-power laser diode can be used (such as commercially available DFB lasers) or else substituted by a low-power laser working in conjunction with an optical amplifier (commonly an Erbium-Doped Fibre Amplifier, EDFA). Both schemes are valid and eventually provide the required optical power to achieve saturation at a fixed wavelength. The second laser beam, referred to as the ***probe***, is a low optical power beam used to probe the saturated transition. This laser is also operated in a cw fashion, but its frequency must be continuously tuned across the desired transition. This probe beam is derived from a second, independent tuneable laser source, or may be extracted from the pump beam using a suitable beam splitter (in that case typically 5-10% of the pump beam is split off). Both the pump and probe beams must be combined, collimated and coupled into the gas hosting structure to achieve light-gas interaction. It is common to set a *co-propagating* scheme when two independent sources are used, while a *contra-propagating* scheme is usually implemented when the probe beam is extracted from the pump. Light is detected using suitable photodiodes (PD) and separation of both beams is usually necessary to extract relevant information. A common approach is to set the relative beam polarizations mutually orthogonal using suitable optical elements and then introduce polarizing beam splitters to separate the beams. An alternative approach is to introduce some kind of modulation (amplitude/frequency) in either/both of the laser sources and then utilise lock-in techniques to demodulate the signals independently at their respective frequencies. Complete separation of the beams can be a difficult task and sometimes is not achieved, so that pump-probe interference effects must be

assessed before carrying out the main experimental work. A schematic illustration of both cases is presented in figure 3-6.

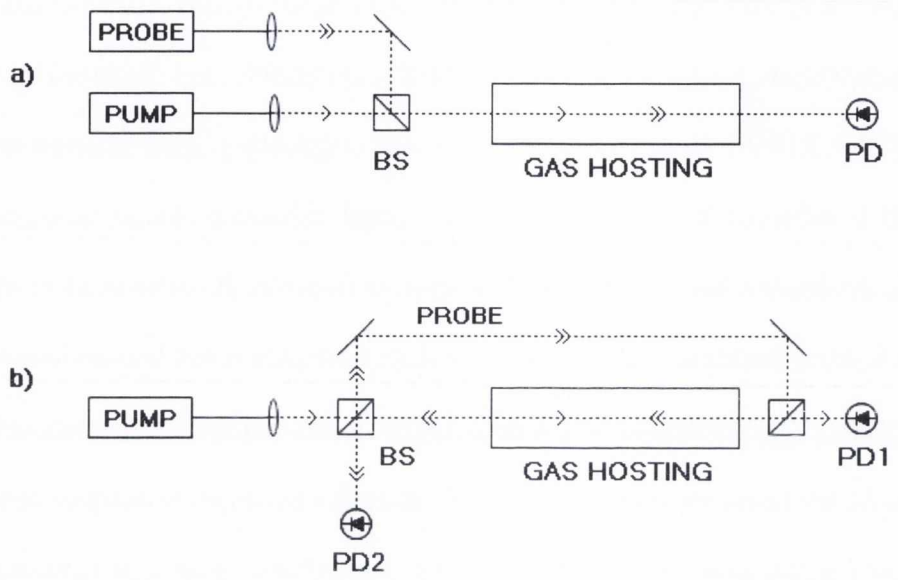

Figure 3-6: *Schematic representation of the most common pump-probe experimental set-ups. a) Independent laser sources with pump and probe beams co-propagating across the gas hosting structure. b) Probe beam extracted from the pump laser and then coupled into the gas hosting structure in a contra-propagating fashion.*

Another issue deserving some attention is that of the gas hosting structure. As mentioned in chapter 2, gas sensing experiments can be carried out in gas cells where gas is injected at a certain pressure and the laser beam undergoes a single or multiple pass along the absorption length. However, Hollow-Core Photonic Bandgap Fibres are well-suited to pump-probe saturation experiments due to their inherent properties: The tight confinement of light in the hollow core greatly increases the optical field power, making it easier to saturate the absorbing transition. In this manner, HC-PBF's present a big advantage as compared to standard gas cells when performing pump-probe experiments. Additionally, the absence of bend losses in these fibres due to the

bandgap guiding principle makes it possible to easily increase the optical absorption length in the gas: a long section of fibre can be coiled occupying only a small volume. A longer interaction path increases the total number of gas molecules saturated before the beam exits the interaction volume, so that the magnitude for the saturation signal will increase as will the Signal-to-Noise Ratio (SNR). If necessary the decay of the pump intensity along the fibre can be theoretically modelled, tailored to the particular information sought. During all of the above, the fibre is usually placed inside a chamber whose gas content can be controlled using suitable gauges and valves. In some cases each of the fibre ends is attached to a different chamber, and the gas diffuses along the fibre when it is injected into either of them [12, 13]. No matter what the final configuration chosen for the pump-probe experiment, all coupling-induced losses must be taken into account and minimised to ensure that enough power to achieve saturation reaches the input of the gas hosting structure.

3.3. EXPERIMENTAL SET-UP

Two different pump-probe experimental schemes have been implemented during the experimental work carried out and are discussed as follows:

3.3.1. SINGLE SATURATION: THE PUMP-PROBE EXPERIMENT

The first case is that of single saturation, where a pump laser targeting a fixed wavelength burns a saturation hole in the gas absorption profile and is observed using the probe laser. This case corresponds to the general description for a pump-probe

experiment given in section 3.2.3. In our case a co-propagating scheme was implemented, making use of two independent laser sources for the probe and pump beams. A schematic of the experimental set-up is presented in figure 3-7.

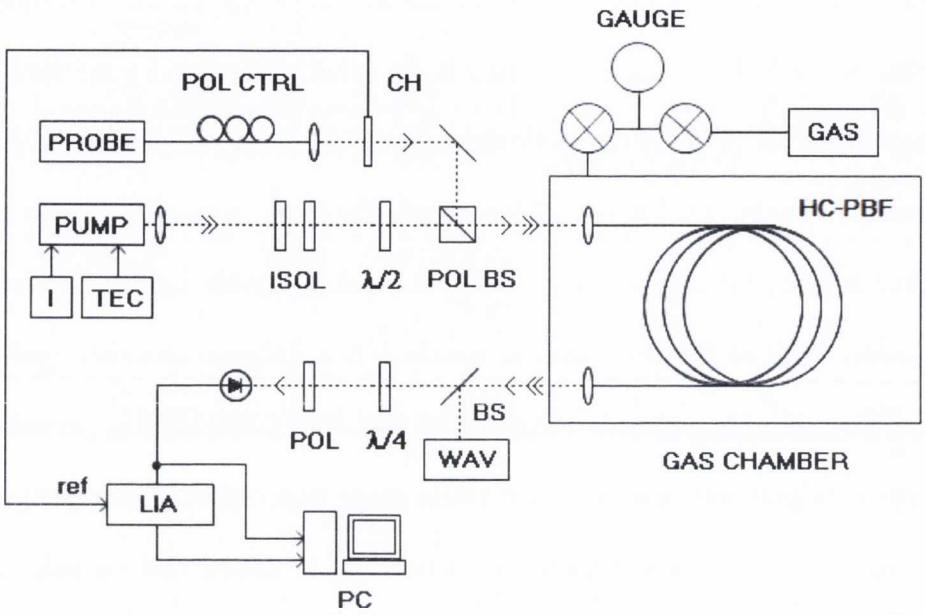

***Figure 3-7**: Schematic illustration of the single saturation co-propagating pump-probe experimental scheme. Main elements and abbreviations used: PROBE = Probe laser; PUMP = Pump laser; TEC = Thermo Electric Cooler; I = Current Source; POL CTRL = Polarization Controller; CH = Chopper; ISOL = Optical Isolator; λ/2 = Half-wave plate; POL BS = Polarizing Beam Splitter; HC-PBF = Hollow-Core Photonic Bandgap Fibre; BS = Beam Splitter; WAV = Wavemeter; λ/4= Quarter-wave plate; POL = Polariser; LIA= Lock-In Amplifier; PC = Personal Computer. All wavelength-dependent elements are designed at a working point of 1.5 μm. The fibre sits inside a vacuum/gas chamber connected to a gas cylinder by means of proper gauges to control the acetylene pressure. The LIA is referenced at the chopper frequency to detect the probe transmission.*

The probe laser is a commercial ECL system with a fiberised optical output that can be fine tuned between 1510 nm and 1590 nm with a resolution better than 1 MHz and power stability better than 1%. Also included is an external modulation facility. The beam is amplitude modulated using a chopper at a frequency f_{CH}. The pump source is

a chip-on-carrier high-power Bookham DFB laser diode with a tuning range of approximately 1.5 nm around 1532.3 nm and a maximum optical output power in excess of 100 mW. It includes an integrated thermistor sensor and is mounted on a heat sink combined with a Peltier element, and operated using external current and temperature control units. The collimated laser emission is protected from back reflections by two optical isolators in series, each carefully adjusted to maximise the transmission (greater than 98%) and minimise the feedback into the laser. The polarizations of the probe and pump beams are adjusted using a polarization controller and a $\lambda/2$ plate respectively. Polarizations are set to be linear and mutually orthogonal, and both beams are then combined using a polarizing beam splitter before coupling into the PBF.

As discussed later within this section, the polarization of the beams changes as they travel along the fibre and some degree of ellipticity is introduced. Thus, a $\lambda/4$ plate is introduced at the chamber output to restore the linear state, and a polariser is then used to separate the beams as required. More details about the effective separation degree achieved are included elsewhere in this section. The Hollow-Core fibre used in the experiment has been already described in chapter 2, a commercial model HC-1550-02 from NKT Photonics with a hollow core of approximately 11 μm in diameter [23]. It is again placed inside the same chamber connected to an acetylene ($^{12}C_2H_2$) cylinder, and the injected amount of gas controlled with the help of a high-speed turbo-molecular pump, vacuum/isolation valves and a pressure gauge. Both laser outputs and the fibre input and output ends are again placed on precision position stages so the coupling into and out of the fibre can be independently optimized. When necessary, a beam splitter is introduced after the chamber output window and reflected light coupled into a fibre connected to a wavemeter. Wavelength readings

are performed with an accuracy of ±1 pm. Light is detected with an InGaAs photodiode (PD) and a Lock-In Amplifier (LIA) referenced at the chopper frequency f_{CH} is used to detect the probe transmission signal. Data are acquired by means of a GPIB personal computer interface.

On the other hand, an additional effect that must be assessed before carrying out the measurements is the effect of any ripples in the transmission spectrum of the fibre. In Hollow-Core Photonic Bandgap Fibres light is trapped in the air core by the photonic bandgap of the cladding structure. The optical field distribution within the bandgap is the result of several modes which propagate along the fibre at the same time. The geometry of the fibre is designed so that under optimum coupling conditions a fundamental mode is peaked at the core of the fibre, while secondary modes only contribute with a small amplitude in the vicinity of the core and are affected by higher propagation losses. This makes the resulting intensity profile propagating across the fibre to be quasi-Gaussian, facilitating the input/output coupling with Gaussian modes associated with single mode fibres used during the experimental work. In the case of our fibre, the optimum fundamental mode exhibits a Quasi-Gaussian profile with >85% shape overlap with the fundamental mode of a conventional fibre [23]. This discussion means that, in practice, coupling of the pump and probe beams into the HC-PBF has to be carefully optimized to get a proper output intensity profile. If coupling is properly adjusted then the fundamental mode at the fibre core is significantly enhanced and the final profile can be regarded Gaussian to a very good extent, providing maximum transmission. In the opposite case, part of the coupled light would contribute to the enhancement of secondary lossy modes propagating in the vicinity of the fibre core. As a result the transmission through the fibre would decrease and the output field distribution would be a combination of more than one

mode. If these effects are not effectively suppressed, then a ripple in the transmission spectrum of the laser light is observed when the wavelength of the laser is scanned across some spectral range. This ripple distorts the real lineshape of the absorption transitions studied, so careful optimization of the input coupling is carried out prior to data acquisition during the experimental work presented in this chapter. An additional method to minimise the effects of multiple modal output from the fibre is to collect the light using large area photodiodes. Because of the inherent degree of birefringence introduced by the fibre, each of the propagating modes would acquire a different polarization state and present a different divergence at the output of the fibre. Focusing the light on large area photodiodes assures collection of all these modes avoiding ripple effects. A detailed analysis of the described effects can be found in [24] for further reference. The previous discussion also applies to the experimental scheme described in the next section without any loss of generality.

3.3.2. DOUBLE SATURATION: EXTENDED PUMP-PROBE EXPERIMENT

In this second case some fundamental modifications are introduced in the previous pump-probe set-up to establish a new approach to the saturation experiment, allowing for saturation effects at two different wavelengths. The experimental scheme presented in the previous section is extended to introduce wavelength modulation techniques as well as an active feedback loop to lock the pump laser emission frequency. These changes are highlighted in red in figure 3-8.

First of all, wavelength modulation of the pump is achieved by connecting an external signal V_{MOD} to the modulation facility integrated in the current control unit of the laser. In our case the voltage signal has a symmetric square shape with a voltage

$\pm V_{MOD}/2$ around zero, so that the emission wavelength of the laser oscillates around the set point reaching the values $\lambda_C \pm \Delta\lambda$. The central point λ_C is set to the pump absorption line centre, so the two operating wavelengths symmetrically target either side of the line. The modulation voltage amplitude determines the exact positions targeted, which can be set anywhere across the absorption line.

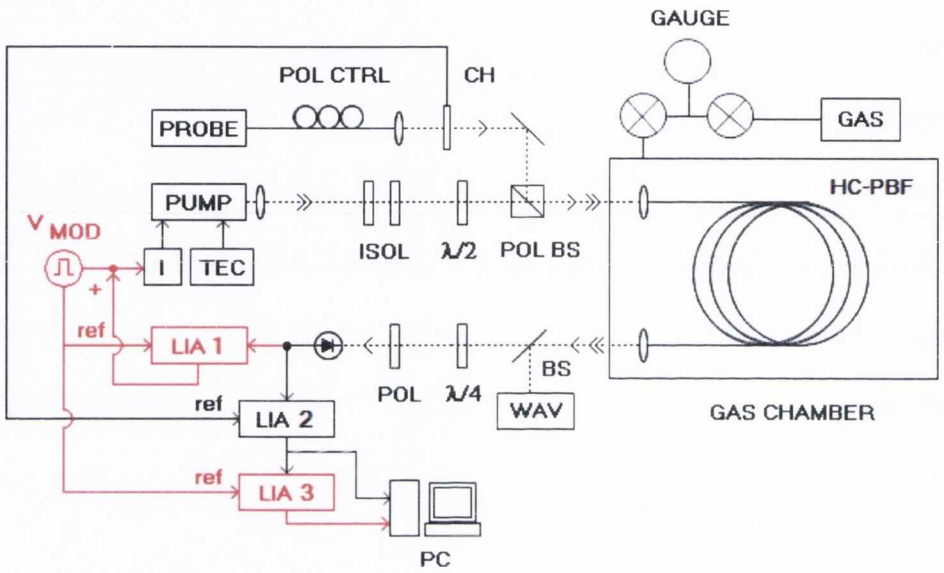

***Figure 3-8**: Scheme for the double saturation co-propagating pump-probe experiment. The set-up is based on that presented in figure 3-7 but has been extended as highlighted in red. The pump laser is now wavelength modulated and a feedback loop is implemented to stabilise its set emission frequency.*

A comparison between the single and double saturation schemes is schematically presented in figure 3-9 for more clarity. Because of the square modulation profile the high saturation power is now alternatively distributed over the two wavelengths $\lambda_C \pm \Delta\lambda$. This means that a saturation hole is now burned at *each* of these wavelength values, and thus we refer to this scheme as the ***double saturation*** pump-probe experiment. Polarization and final spatial separation of the two beams is controlled using the same $\lambda/2$, $\lambda/4$ and polarization controllers than in the previous section.

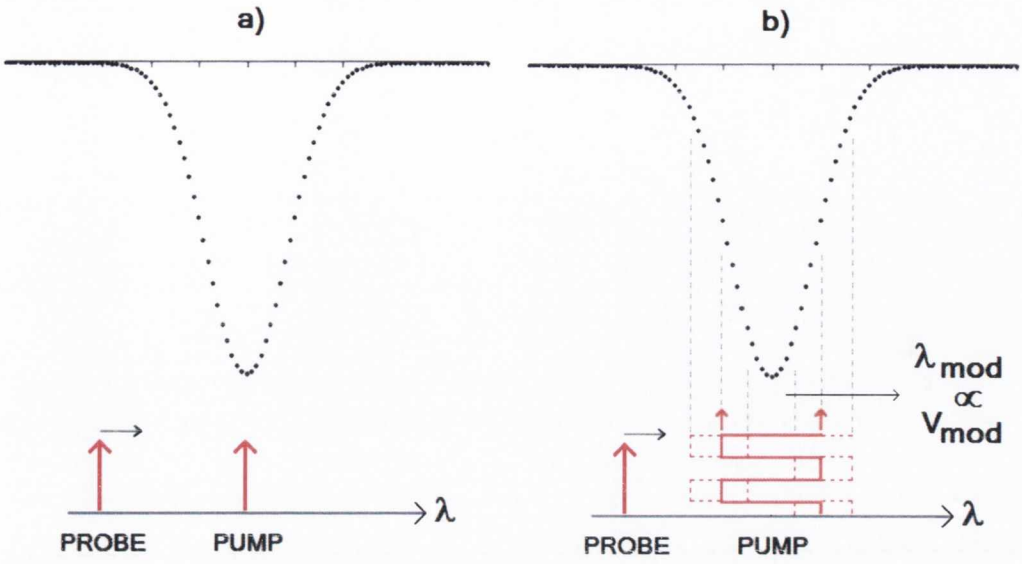

***Figure** 3-9: Schematic comparison between the single and double saturation spectral schemes. In the single saturation case (a) the probe is scanned across the absorption line which is saturated by the pump beam at the centre wavelength. In the double saturation case (b) the pump frequency is modulated with square profile and saturation occurs alternatively at two wavelength points λ_{MOD}, whose distance from the line centre is determined by the modulation voltage V_{MOD}.*

A lock-in amplifier LIA1 referenced to the pump modulation frequency processes the transmitted signal through the fibre. This modulation scheme is essentially equivalent to a WMS technique with the output of the LIA proportional to the first derivative (*1f*) of the transmission, though some differences apply: first of all, the modulation depth is bigger than that of a typical WMS experiment; secondly, the modulation signal has a square shape rather than a sinusoidal one; and third, the set wavelength λ_C of the modulated laser is not tuned across the absorption line. These differences are not a problem to implement a frequency locking loop: They don't affect the output of the lock-in significantly when the loop is closed, and that output is the loop feedback

signal. The frequency of the pump laser is set to the line centre, so the corresponding value of the first derivative amplitude detected by the lock-in is zero. In an ideal case there would be no drift of the pump emission frequency from the set point so the amplitude would be exactly zero at all times. In a real case, however, some finite noise occurs which causes the 1f amplitude to randomly oscillate around zero with a small amplitude (this issue is described in detail in chapter 4). When this signal is connected back to the pump laser injection current control unit with the correct lock-in phase, the laser noise can be effectively nullified and the laser emission frequency locked to the line centre with a high degree of accuracy. In this experiment the locking technique is implemented to assure a symmetric wavelength modulation around the line centre, allowing a double Lorentzian lineshape to fit the recorded data. Then the main saturation parameters can be extracted and discussed in a confident way, facilitating the understanding of nonlinear saturation effects. In the next chapter a similar feedback loop is described again, but this time with a different aim: to characterize the main parameters regarding the frequency stabilization of the laser. For such reasons, a detailed theoretical analysis of feedback loops along with a detailed explanation of the working principles of the locking loop implemented here will be included then. The second lock-in amplifier (LIA2) in the experimental scheme is referenced to the chopper modulation frequency f_{CH} so that its output corresponds to the transmitted probe intensity. Finally, a third lock-in (LIA3) is introduced in series after LIA2, and is referenced at the pump modulation frequency f_{MOD}. Here lies the key to the saturation technique implemented in this case: this third lock-in will detect any signal in the probe transmission which is directly caused by the pump beam, the saturation signal. This signal will be referred as the ***pump-probe (PP)*** signal from now on, and its expected shape can be estimated taking into account the

previous experimental discussion. Firstly, two saturation holes are burned at each wavelength $\lambda_C \pm \Delta\lambda_C$; secondly, because this signal is filtered through a double lock-in scheme, it is directly proportional to the shape of the saturation dip and any sloped background is eliminated (significantly improving the final SNR); thirdly, because the saturation power reaches each of the wavelengths $\lambda_C \pm \Delta\lambda_C$ at alternative times due to the square modulation, there is an effective phase difference of π radians between the two signals detected by the lock-in. This means that the two signals have opposite sign. Details of the specific mathematical expression used to describe this double-peaked lineshape along with theoretical fits of the experimental data are included in section 3.4.2.

3.4. RESULTS AND DISCUSSION

3.4.1. SINGLE SATURATION

The experimental scheme is implemented as explained in section 3.3.1 to study single saturation effects of $^{12}C_2H_2$ overtone rotational transitions in the $\nu_1+\nu_3$ vibrational band around 1.5 μm. According to the notation introduced in section 3.2.2, a non-resonant scheme is used with the pump laser diode targeting the *P(13)* gas line centred at 1532.830 nm and the probe wavelength tuning across the *R(11)* absorption feature at 1519.137 nm. This overtone rotational absorption scheme is essentially a three-level coupled system with a Λ-type *R(J-1) – P(J+1)* interaction, as shown in figure 3-10, where both transitions share the same upper energy level [11]. Using a non-resonant scheme minimises any possible interference between the pump and probe

beams, shifting any beat signal to much higher frequencies away from our targeted region.

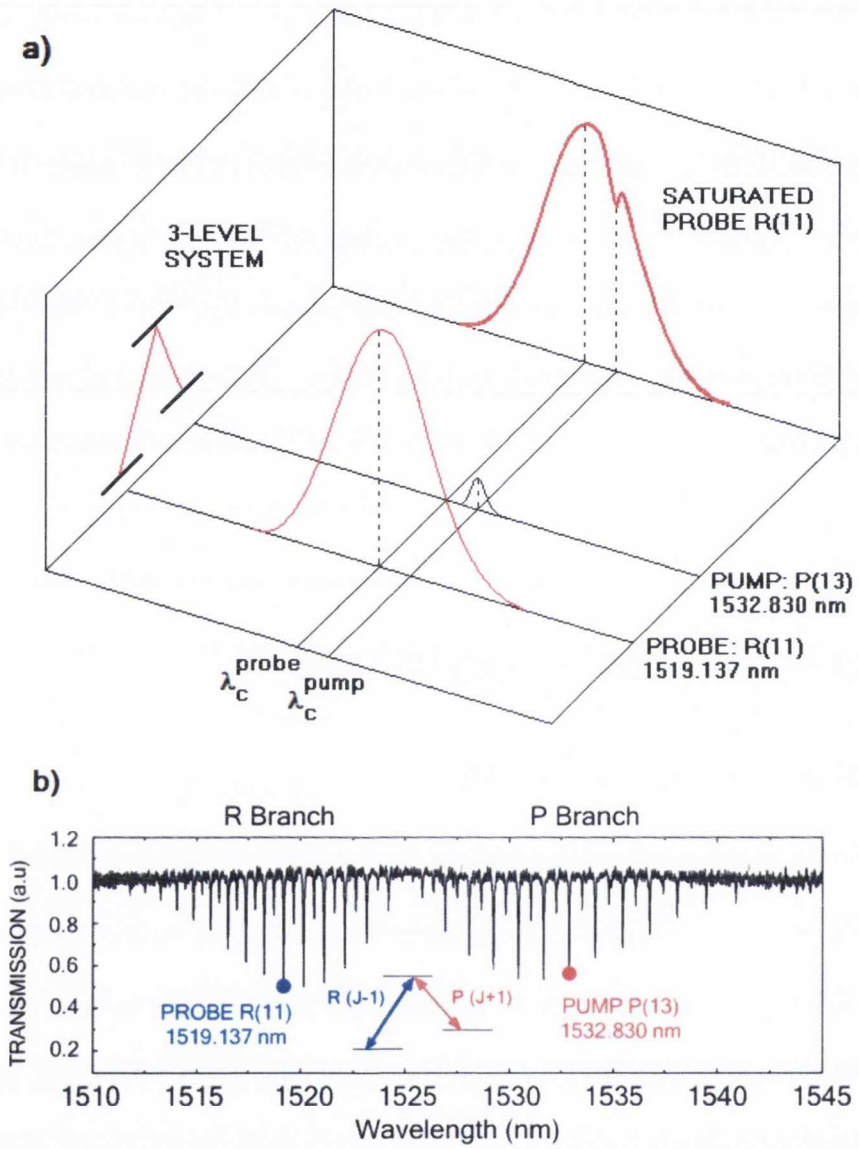

Figure 3-10: *Three- (a) and two-dimensional (b) representations of the non-resonant spectral scheme used in the single saturation pump-probe experiment. The pump laser diode targets the* P(13) *gas line centred at 1532.830 nm and the probe wavelength is tuned across the* R(11) *absorption feature at 1519.137 nm. The pump is shifted from the line centre in the three-dimensional diagram for clarity.*

The measured output powers of the pump and probe lasers are approximately 100 mW and 5 mW respectively while the maximum measured coupling of both lasers into the PBF reaches approximately 50%. Spatial separation of the beams is controlled by means of the polarization components already described, and the free-space optical isolators associated with the pump laser beam are fine tuned to prevent back reflections from distorting its linewidth performance. Separation of the beams is not complete because some properties of the PBF change the polarization state of the coupled lasers as they travel along the fibre. Firstly, because the PBF fibre exhibits some degree of birefringence, the input linear polarizations of both lasers are transformed to an elliptical state. Because the lasers operate at different wavelengths, the degree of ellipticity introduced might be different for each of them. This means that the $\lambda/4$ wave plate cannot transform them back to their original and mutually perpendicular linear polarization state, and the polariser cannot fully separate them. Secondly, because the guiding properties of the fibre are based on photonic bandgap effects (i.e. multiple interference of different electromagnetic modes), more than one mode might be present at the output of the fibre. In that case the polarization state of the beams cannot be defined by a single state, and the original polarization states cannot be recovered. Thus, because the separation is not complete part of the pump beam reaches the photodiode. However, this does not affect our probe measurements because the probe beam is amplitude modulated and detected using a lock-in, effectively filtering the pump signal out of the targeted region. The probe beam is modulated using a chopper at a frequency $f_{CH} = 2.191$ kHz, with the lock-in amplifier referenced to the same frequency in order to detect the transmission signal. The experiment was carried out at a room temperature of T = 22°C and the acetylene gas pressure in the measurement chamber was maintained at $p_{C2H2} \approx 1$ mbar.

The results for the saturation of the three-level system are presented in figure 3-11. Non-resonant saturation of the absorbing transition was achieved and is clearly depicted in the figure inset. For PBF input laser pump powers of around 40 mW, the measured Doppler width is $\Delta\upsilon_D \approx 470$ MHz and a saturation dip is created at the absorption line centre with a measured depth and linewidth of approximately 2% and 50 MHz respectively. It is important to note that the scan rate of the probe laser must be carefully chosen when performing these measurements. The narrow saturation dip created by the pump laser drifts with time around the line centre according to the *1/f* noise from the temperature and current control units connected to the laser (this issue is discussed in more detail in section 4.2 in next chapter). If the scan rate is too slow compared with the drift frequency then an averaging effect will occur and the lineshape of the saturation dip will be effectively broadened.

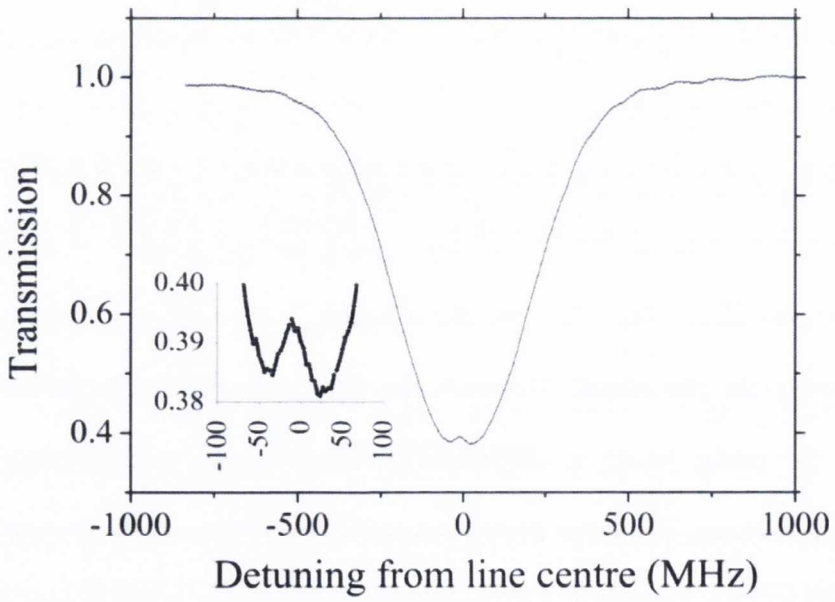

***Figure 3-11**: Non-resonant pump-probe saturation results for 1 mbar of acetylene inside the PBF at an input pump power of 40 mW. The measured Doppler width is $\Delta\upsilon_D \approx 470$ MHz while a saturation dip of around 2% with a linewidth of 50 MHz is observed at the centre of the probe transmission spectrum.*

The narrow measured linewidth of 50 MHz for the saturation dip agrees very well, within experimental error, with the estimated theoretical value of approximately $\Delta\upsilon_{SAT} \approx 48$ MHz. This value is the sum of a Lorentzian collisional broadening contribution [25] of $\Delta\upsilon_{COL} \approx 8$ MHz for a total pressure of 1 mbar plus a transit-time broadening [26] of $\Delta\upsilon_{TT} \approx 40$ MHz. When calculating the transit-time contribution the assumption is made that acetylene molecules cross a Gaussian beam of *1/e* intensity diameter d = 7.5 μm (this value corresponds to the quoted diameter in the fibre datasheet [23]) with a three-dimensional (3D) mean molecular velocity $v_{3D} = \sqrt{(8RT/\pi M)} = 490.3$ ms^{-1} at a temperature of T = 22°C, and a corrected two-dimensional (2D) velocity of $v_{2D} = \sqrt{(2/3)}v_{3D} = 400.3$ m s^{-1} (this correction is introduced because the transit-time broadening is calculated with respect to any direction perpendicular to the fibre axis). The total linewidth of the saturation dip corresponds to the convolution of both effects and exactly equals the sum of the two contributions if both lineshapes are Lorentzian [27]. However, the transit-time broadening follows a Gaussian-like lineshape as explained in section 2.2.3 in chapter 2 [28, 29] so an approximation has been introduced to estimate the total saturation dip linewidth. The estimated result agrees well with those obtained by R.Thapa et al. [14], where acetylene saturated transitions are studied in HC-PBF's of different diameters for various pressure values. Transit-time broadening is commonly the limiting factor for the linewidth, and can be reduced to values of around ≈ 15 MHz by selecting low-velocity molecules (Hald et al., [30]) or down to ≈ 10 MHz using large-core PBF's (Jones et al., [31]). Pressure broadening can be minimised by working at acetylene pressures as low as 0.001 mbar and thus increase the saturation level achieved in HC-PBF's, as reported by Benabid et al. [11].

3.4.2. DOUBLE SATURATION

In the second case the experimental scheme is extended as explained in section 3.3.2. The same Λ-type overtone rotational absorption scheme is used with the probe and pump lasers, as already outlined, targeting the P(13) and R(11) lines around 1.5 μm respectively. The measured optical powers are again approximately 100 mW and 5 mW respectively. The chopper modulates the probe beam at the same frequency f_{CH} = 2.191 kHz, and now the pump is wavelength modulated with a square signal of frequency f_{PUMP} = 90 Hz. The modulation depth is varied in order to scan the saturation wavelength across the absorption line. The polarization of the beams and their spatial separation is carried out in the same fashion, using suitable polarization elements. As explained in the previous section, the separation of the beams is not complete and a small fraction of the pump light still reaches the photodiode. Full separation of the probe and pump beams is commonly desired in pump-probe experiments, but the remaining pump light is an advantage in the present case: it can be detected with the corresponding lock-in amplifier (LIA1) and the signal used to implement the emission frequency locking loop for the pump laser. The probe signal is detected on the other hand with a second lock-in amplifier (LIA2) set in parallel, referenced at the chopper modulation frequency f_{CH}. Finally, because the pump signal is modulated at a frequency much smaller than the probe, its signature goes through the fast lock-in amplifier LIA2 and can be detected in a third one (LIA3) set in series and referenced to the pump modulation frequency f_{PUMP}. It is important to emphasize here a basic but important condition that must be fulfilled whenever two or more different signals are modulated within the same experimental scheme: In order to avoid undesired mixing of the signals during the demodulating stage, the respective modulation frequencies must not match any of the harmonics of each other (a well-

known example is that of avoiding modulation frequencies which are harmonics of the mains frequency f_{MAINS} = 50 Hz, because otherwise some noise would be introduced in the measurements). As before the room temperature is constant at T = 22 °C with the acetylene pressure remaining at p_{C2H2} = 1mbar.

Experimental results are presented in figure 3-12 below, including selected pump-probe traces recorded at different values of the modulation voltage V_{MOD} after consecutive scans. The modulation depth is directly proportional to the modulation voltage, so from now on we will refer to this parameter during our discussions without any loss of generality. A total of fifteen traces at different modulation depths covering the total width of the absorption line were recorded, but only four are shown for clarity reasons.

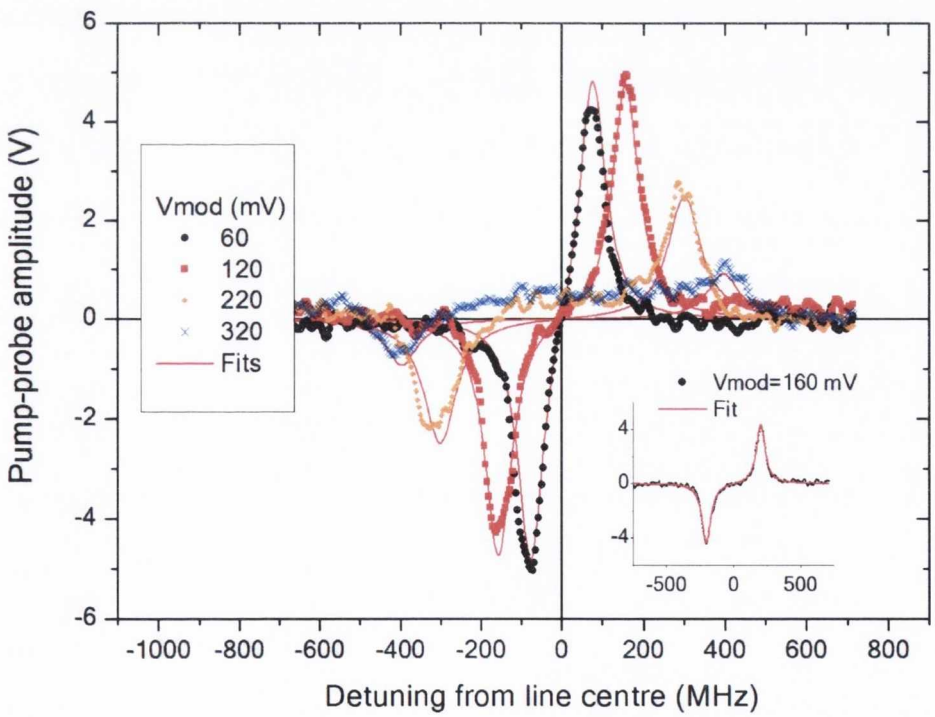

***Figure 3-12**: Selected results for the non-resonant double saturation experiment. A saturation signal is detected at both sides of the absorption line centre with opposite sign, and each trace is fit to a double Lorentzian lineshape to extract relevant parameters, as shown in the inset.*

As expected from the theoretical point of view, each of the obtained pump-probe signals consists of two saturation peaks of opposite sign symmetrically located around the line centre. Because each of the saturation wavelengths only affects a single "molecular-speed" group of the acetylene gas, the saturation peaks are not affected by Doppler broadening but only by homogeneous broadening processes and their lineshape is Lorentzian. Each of the experimental traces can be thus described by a double Lorentzian lineshape of the form $y(x) = L_{RIGHT}(x) - L_{LEFT}(x)$, where the two Lorentzian functions $L_i(x)$ are symmetrically centered at distances $\pm x_C$ from the line centre and share the same area under the curve A and full-width at half maximum (FWHM) parameter w, according to the expression

$$L(x) = \frac{2A}{\pi} \frac{w}{4(x - x_C)^2 + w^2} \tag{3.11}$$

Results for the corresponding fits are presented in table 3-1, along with the corresponding errors ΔW, Δx_C and ΔA for the three extracted parameters. Analysis of the results yields several points. From the qualitative point of view, it first becomes clear from figure 3-12 that the SNR of the pump-probe (PP) signal has dramatically increased compared with that of the single saturation case. Now the saturation signal rests on a flat background rather than on the transmitted signal itself, making the theoretical fit possible with good accuracy. The height of the saturation signal decreases as the modulation depth of the pump laser is increased, as expected due to the molecular absorption decreasing away from the line centre. Some small finite background exists in the region between the two peaks, due to the remaining pump light detected by the two-lock-in amplifier scheme. Only for high modulation depths

the PP signal becomes too low and comparable with this background, decreasing the fit accuracy (note how the error values increase with modulation voltage in table 3-1).

Table 3-1 · Double saturation experimental fit results

V_{MOD}	W	ΔW	Xc	ΔXc	A	ΔA
mV	MHz	MHz	MHz	MHz	MHz V	MHz V
60	39.25	0.96	75.98	0.56	317.56	6.54
80	36.51	0.82	103.54	0.50	291.51	4.99
100	39.03	0.85	125.24	0.53	304.02	4.91
120	39.99	0.85	156.18	0.55	302.82	4.69
140	38.04	0.83	177.90	0.55	279.17	4.40
160	38.73	0.88	203.75	0.59	268.18	4.36
180	43.01	1.16	232.52	0.78	236.91	4.58
200	42.11	1.19	248.15	0.80	221.71	4.48
220	46.80	1.45	277.85	0.98	213.75	4.72
240	48.88	1.71	301.08	1.16	192.10	4.81
260	46.14	2.22	326.29	1.52	134.51	4.61
280	47.73	3.11	351.35	2.13	101.15	4.68
300	47.76	3.47	371.33	2.38	90.48	4.66
320	48.78	4.58	396.48	3.15	70.51	4.70
340	47.70	6.66	406.99	4.59	46.80	4.64

***Table 3-1**: Fitting results for the non-resonant double saturation traces presented in figure 3-12. The row highlighted in blue approximately corresponds to the half-width points of the overall Doppler-broadened absorption line ($x_C \approx 250$ MHz, $FWHM_{DOPPLER} \approx 470$ MHz).*

On the other hand, a quantitative analysis for the linewidth (w) and area under the curve (A) parameters can be performed according to the fit results. Plots for these two parameters versus the location fit parameter x_C are included in figures 3-13 and 3-14 to further illustrate the discussion. The parameter x_C is chosen for the x-axis because it is expressed in frequency units and thus can be directly compared to the overall width of the absorption line.

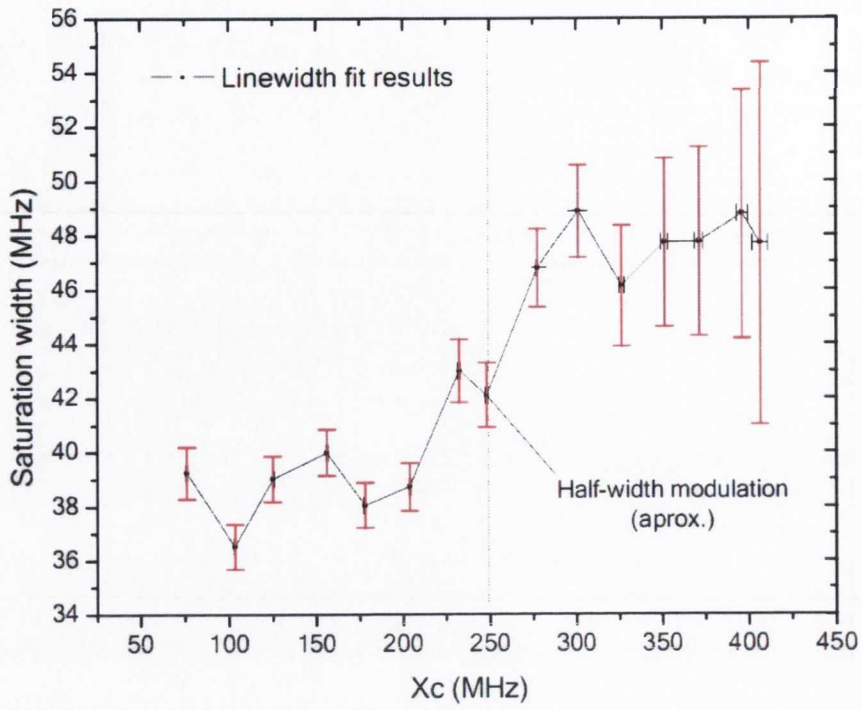

***Figure 3-13**: Plot for the saturation width of the pump-probe signal versus the location parameter according to the fit results presented in table 3-1.*

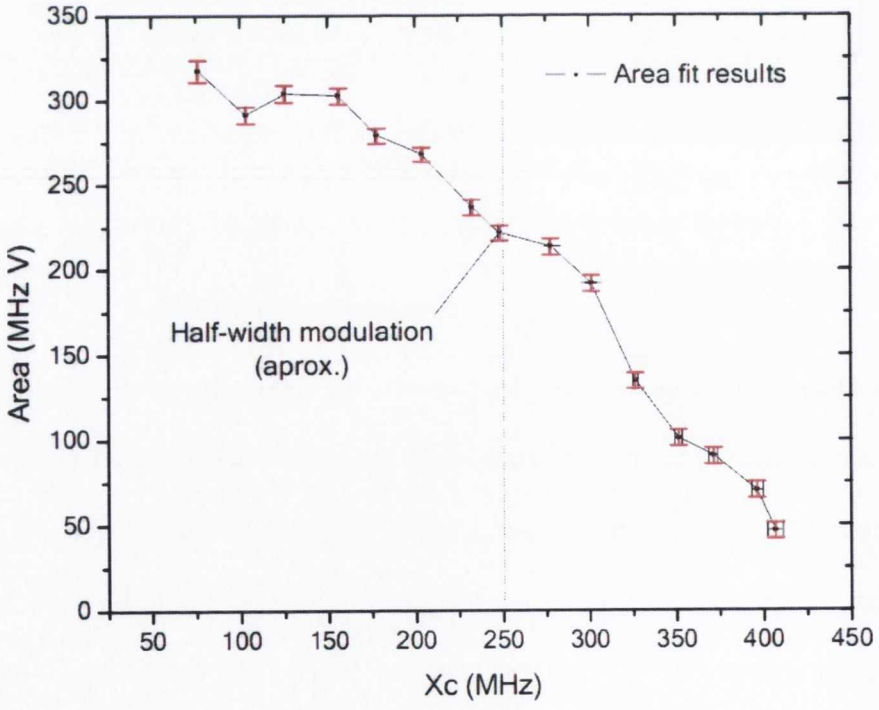

***Figure 3-14**: Plot for the area parameter (A, area under the curve) of the Lorentzian curves used to model the pump-probe signal versus the location parameter, according to the fit results presented in table 3-1.*

The linewidth data presented in figure 3-13 illustrate an interesting result. As can be observed, the results suggest an increasing trend for the linewidth of the pump-probe signal with modulation depth of the pump laser. Values for the linewidth lie now approximately within the (38-50) MHz interval. The theoretical estimation of $\Delta\upsilon_{SAT} \approx$ 48 MHz presented in the previous section 3.4.1 lies within the same interval, but the change of the linewidth value requires further analysis. On the other hand the results for the area under the curve parameter (A) presented in figure 3-14 point out an additional issue. The area under the curve is directly proportional to the degree of saturation achieved by the pump laser, so the plot indicates that the saturation is decreasing as we move away from the line centre. This can be understood by the fact that the absorption of the gas line at the wings is smaller than at its centre, leading to a decrease of the saturation power affecting the molecular transition.

The effect of the saturation power in the linewidth of saturation signals has been theoretically treated and experimentally tested in the literature, utilising set-ups with co-propagating beams where the pump laser frequency was fixed at the centre of the absorption line. Javan et al. present a detailed theoretical analysis for a three-level system in [32], where it is shown that at low saturation powers the linewidth of the Lamb dip at the probe absorption line centre is proportional to the square root of the input power. Both Benabid et al. [11] and Gosh et al. [12] have reported experimental results in good agreement with theoretical predictions targeting acetylene hosted in hollow-core PBF's at the 1.5 μm spectral region. In the case of Gosh et al. [12], for example, the linewidth of the saturation signal varies within the (30-60) MHz range for optical powers of (75-300) mW at the output of the fibre, at gas pressures between 10-200 mTorr. Our experimental scheme differs from these examples in several ways.

First, the pump frequency is modulated and alternatively targets two values at either side of the line; second, the change in saturation power is due to a decrease in molecular absorption rather than due to a change of the operating conditions of the laser itself. This will require further theoretical analysis in the future.

3.5. CONCLUSIONS

In this chapter we have described the successful extension of the gas sensing scheme in HC-PBF's to the nonlinear region, where saturation effects take place. These fibres present several advantages for saturation experiments compared with other gas hosting structures, including the relaxation of laser power requirements. The presented experiments have been carried out using laser diodes readily available from industry. In the first part results for the single saturation of a non-resonant combination of two absorbing transitions have been presented. A pump-probe experimental scheme has been employed, the main saturation parameters have been characterized and successfully compared with theoretical estimations. These results prove the saturation capabilities of this microstructure. In the second part a novel approach to the pump-probe scheme has been introduced, extending the experimental scheme in order to increase the SNR and improve the accuracy of the saturation results. Wavelength modulation techniques and two-lock-in amplifier detection techniques were included in the pump-probe scheme. Saturation of the pump absorbing transition at two different wavelengths was proposed and demonstrated. The SNR of the saturation signal was dramatically increased by several orders of magnitude due to the implemented wavelength modulation and two-lock-in detection technique. This technique could be applied to the single saturation case if the pump

laser was also amplitude modulated, but then the optical power reaching the HC-PBF would decrease and thus the saturation effect. Using the proposed double saturation scheme no loss of optical power occurs, with the full saturation power reaching the gas molecules hosted in the fibre. In addition, an active feedback loop has been implemented to lock the pump laser frequency to the centre of the corresponding gas absorption line. This allows for consistent symmetry of the experimental results that facilitates mathematical fitting to extract the relevant parameters. Moreover, the saturation at two different wavelengths opens up the possibility for the study of new saturation features. The results obtained applying this novel scheme suggest that the modulation technique affects the saturation degree for the targeted molecular transition, modifying the linewidth properties of the saturation profiles. Similar effects have been investigated from a theoretical and experimental point of view by several authors regarding different experimental schemes, so future work should focus on further theoretical analysis to explain these interesting results.

3.6. REFERENCES

1. J. C. Knight, "Photonic crystal fibres," Nature **424**, 847-851 (2003).

2. P. S. J. Russell, "Photonic-Crystal Fibers," Lightwave Technology, Journal of **24**, 4729-4749 (2006).

3. A. M. Cubillas, J. Hald, and J. C. Petersen, "Optical heterodyne saturation spectroscopy in ammonia filled hollow-core photonic bandgap fibers," in *Lasers and Electro-Optics, 2008 and 2008 Conference on Quantum Electronics and Laser Science. CLEO/QELS 2008. Conference on*(2008), pp. 1-2.

4. J. Henningsen, J. Hald, and J. C. Peterson, "Saturated absorption in acetylene and hydrogen cyanide in hollow-core photonic bandgap fibers," Opt. Express **13**, 10475-10482 (2005).

5. A. M. Cubillas, J. Hald, and J. C. Petersen, "High resolution spectroscopy of ammonia in a hollow-core fiber," Opt. Express **16**, 3976-3985 (2008).

6. F. Benabid, F. Couny, J. C. Knight, T. A. Birks, and P. S. J. Russell, "Compact, stable and efficient all-fibre gas cells using hollow-core photonic crystal fibres," Nature **434**, 488-491 (2005).

7. J. Tuominen, T. Ritari, H. Ludvigsen, and J. C. Petersen, "Gas filled photonic bandgap fibers as wavelength references," Optics Communications **255**, 272-277 (2005).

8. C. S. Edwards, H. S. Margolis, G. P. Barwood, S. N. Lea, P. Gill, and W. R. C. Rowley, "High-accuracy frequency atlas of 13C2H2 in the 1.5 um region," Applied Physics B: Lasers and Optics **80**, 977-983 (2005).

9. P. Minutolo, C. Corsi, F. D. Amato, and M. D. Rosa, "Self- and foreign-broadening and shift coefficients for C2H2 lines at 1.54 um," The European Physical Journal D **17**, 175-179 (2001).

10. K. Nakagawa, M. de Labachelerie, Y. Awaji, and M. Kourogi, "Accurate optical frequency atlas of the 1.5 um bands of acetylene," J. Opt. Soc. Am. B **13**, 2708-2714 (1996).

11. F. Benabid, P. Light, F. Couny, and P. Russell, "Electromagnetically-induced transparency grid in acetylene-filled hollow-core PCF," Opt. Express **13**, 5694-5703 (2005).

12. S. Ghosh, J. E. Sharping, D. G. Ouzounov, and A. L. Gaeta, "Resonant Optical Interactions with Molecules Confined in Photonic Band-Gap Fibers," Physical Review Letters **94**, 093902 (2005).

13. K. Knabe, R. Thapa, O. L. Weaver, B. R. Washburn, and K. L. Corwin, "Comparison of Saturated Absorption Spectra of Acetylene Gas Inside Photonic Bandgap Fibers," in *Tech. Digest, Symposium on Optical Fiber Measurements (SOFM 2006), Sep 19-20, 2006* (NIST Special Publication 1055, Boulder, CO, 2006), pp. 55-58.

14. R. Thapa, K. Knabe, M. Faheem, A. Naweed, O. L. Weaver, and K. L. Corwin, "Saturated absorption spectroscopy of acetylene gas inside large-core photonic bandgap fiber," Opt. Lett. **31**, 2489-2491 (2006).

15. W. Demtröder, *Laser Spectroscopy: Basic Concepts and Instrumentation, 2Ed* (Springer, 1996).

16. V. S. Letokhov, and V. P. Chebotayev, *Nonlinear Laser Spectroscopy* (Springer-Verlag, 1977).

17. W. Demtröder, "3.1.3. Natural Linewidth of Absorbing Transitions," in *Laser Spectroscopy: Basic Concepts and Instrumentation, 2Ed*(Springer, 1996).

18. M. Fleischhauer, A. Imamoglu, and J. P. Marangos, "Electromagnetically induced transparency: Optics in coherent media," Reviews of Modern Physics **77**, 633 (2005).

19. J. Gea-Banacloche, Y.-q. Li, S.-z. Jin, and M. Xiao, "Electromagnetically induced transparency in ladder-type inhomogeneously broadened media: Theory and experiment," Physical Review A **51**, 576 (1995).

20. S. E. Harris, "Electromagnetically Induced Transparency," Physics Today **50**, 36-42 (1997).

21. H. R. Gray, R. M. Whitley, and J. C. R. Stroud, "Coherent trapping of atomic populations," Opt. Lett. **3**, 218-220 (1978).

22. C. N. Banwell, and E. M. McCash, "Chapter 3: Infra-Red Spectroscopy," in *Fundamentals of Molecular Spectroscopy* (McGraw-Hill, 1994).

23. NKT photonics, "HC-1550-02 fibre datasheet," http://www.nktphotonics.com/side5334.html.

24. G. Humbert, J. Knight, G. Bouwmans, P. Russell, D. Williams, P. Roberts, and B. Mangan, "Hollow core photonic crystal fibers for beam delivery," Opt. Express **12**, 1477-1484 (2004).

25. O. Svelto, *Principles of Lasers 4th Ed., Ch. 2, pp. 44-45* (Springer, 1998).

26. K. Shimoda, *High-Resolution Laser Spectroscopy, Ch.2, pp. 12-14* (Springer-Verlag, 1976).

27. J. Elijah Kannatey-Asibu, "Broadening mechanisms," in *Principles of Laser Materials Processing*, J. W. Sons, ed. (2009), pp. 90-92.

28. P. F. Bernath, "Transit time broadening," in *Spectra of atoms and molecules*, O. U. P. USA, ed. (2005), pp. 31-33.

29. W. Demtröder, "3.4. Transit-Time Broadening," in *Laser Spectroscopy: Basic Concepts and Instrumentation, 2Ed*(Springer, 1996).

30. J. Hald, J. C. Petersen, and J. Henningsen, "Saturated Optical Absorption by Slow Molecules in Hollow-Core Photonic Band-Gap Fibers," Physical Review Letters **98**, 213902-213904 (2007).

31. M. J. Andrew, K. Kevin, L. JinKang, T. Rajesh, T. Karl, C. Francois, S. L. Philip, B. Fetah, R. W. Brian, and L. C. Kristan, "Stability of Optical Frequency References Based on Acetylene-Filled Kagome-Structured Hollow Core Fiber," in *Frontiers in Optics*(Optical Society of America, 2008), p. FWF7.

32. A. Javan, O. Kocharovskaya, H. Lee, and M. O. Scully, "Narrowing of electromagnetically induced transparency resonance in a Doppler-broadened medium," Physical Review A **66**, 013805 (2002).

CHAPTER 4

SATURATION-BASED LASER FREQUENCY STABILISATION

4.1. INTRODUCTION

Laser spectroscopy is nowadays a vast research area covering a huge number of topics and applications, with multiple types of laser sources and instrumentation available and necessary in each particular case [1]. Experimental work concerning gas sensing, utilising affordable laser diodes readily available from the telecommunications industry, was investigated and is reported in this thesis. Hollow-Core Photonic Bandgap fibres [2, 3] are used due to their advantages in these experiments [4-6]. The basic properties and sensing capabilities of these fibres have been presented in chapter 2, while characterization of the main properties of saturated transitions and demonstration of a novel experimental scheme under a nonlinear absorption regime have been covered in chapter 3.

One of the most important requirements in some laser spectroscopy and gas sensing experiments is the high stability of the laser optical frequency. This characteristic plays a crucial role and some particular applications based on HC-PBF fibres are extremely dependent on it, such as wavelength referencing [7, 8]. Frequency stability of the laser output is usually limited by current and temperature induced

effects related to the laboratory equipment necessary to operate a laser diode device. Low-noise equipment to increase frequency stability is expensive and thus not always accessible for research, so frequency stabilization techniques based in standard laboratory equipment are of great interest. In order to achieve this goal, nonlinear absorption effects become very useful because of the narrow spectral width of the profiles involved. Nonlinear effects are easily obtained using Hollow-Core Photonic Bandgap Fibres and have been extensively studied [9], making these fibres very good candidates to implement new stability techniques. Several laser locking techniques have been investigated, based on saturation effects and implementation of active feedback loops. These techniques typically involve a pump-probe scheme where an Erbium-Doped Fibre Amplifier (EDFA) is used to provide the high optical power for the pump laser beam. This beam is usually split and a small fraction is frequency or amplitude modulated, in order to obtain a feedback signal to stabilise the laser frequency. Some examples include stabilization of External Cavity Lasers (ECL) using piezo-locking in acetylene-filled Fabry-Pérot cavities [10, 11], Rubidium saturation spectroscopy [12], ECL locking in Rubidium and metastable Argon reference cells using differencing techniques [13], Distributed Feedback (DFB) laser stabilization using third-harmonic techniques [14, 15] and modulation transfer spectroscopy [16] in acetylene gas cells. In addition, large-core HC-PBF's in conjunction with Frequency Modulation (FM) techniques have been used in recent experiments to stabilise fibre lasers [17, 18]. Each of these techniques has strengths and weaknesses and can be selected depending on the particular application to be used.

In this chapter a novel application of Wavelength Modulation (WM) techniques [19] to modulation-free laser stabilization is presented, based on the non-resonant

saturated transitions of acetylene in HC-PBF's presented in chapter 3. The former pump-probe experimental scheme is extended and wavelength modulation of the probe laser is used to produce an error signal to lock the pump laser. The use of laser diodes makes it easy to apply modulation techniques, due to the versatility of these readily available laser sources. As opposed to other stabilization techniques, the pump laser beam is neither split nor modulated at any experimental stage in our case. This is a novel feature which improves the optical power available for optical saturation, as well as simplifying the experimental scheme to a significant extent. No EDFA is necessary to achieve saturation and the required locking electronics remain very basic. The locking capabilities of the technique are demonstrated here for both constant and variable temperatures of the pump DFB laser diode, but are applicable to other types of laser sources. In addition, frequency locking of the laser is demonstrated utilising a non-saturation standard technique. This makes it possible to compare the results and emphasize the significant improvement achieved with our novel technique.

4.2. BACKGROUND

4.2.1. LASER WAVELENGTH TUNING AND STABILITY

An ideal laser is designed to provide a monochromatic output of a certain optical frequency v. Parameters such as the resonance cavity length, gain medium and reflectors are carefully chosen to fulfil the gain and phase conditions necessary for lasing. The phase condition depends on the cavity length L and the effective refractive index (n) [20, 21] $n_{eff} = n'_{eff} + jn''_{eff}$ yielding a set of available modes within the cavity of wavelengths [22]

$$\lambda_M = 2n'_{eff}L/M \tag{4.1}$$

where M is the mode order. Lasing starts for the cavity mode with minimum mirror losses, because it is the first mode for which the roundtrip cavity gain equals one. On the other hand the ability to tune the laser output over a certain frequency range is desirable in some cases, such as in spectroscopy experiments. From equation 4.1 it follows that two of the methods to achieve wavelength tuning are a) changing the value for the real part of the effective refractive index n'_{eff} and b) changing the cavity length L.

In the first case, wavelength of the laser can be tuned because both the mirror losses and the condition for the wavelength λ_M of the cavity modes depend on the effective refractive index. One example relying on refractive index change is that of a uniform grating where the value of n_{eff} is modulated with a period Λ, causing light reflections at every index-step interface. Constructive interference of the reflections and thus lasing takes place when the Bragg condition is fulfilled,

$$\lambda_{laser} \approx \lambda_{bragg} = 2\Lambda n'_{eff} \tag{4.2}$$

Tuning can be achieved by changing the real part of the effective refractive index n'_{eff} giving rise to a wavelength shift

$$\Delta\lambda = \left|\Delta n'_{eff}\right| / n'_{eff}\lambda_{B,0} \tag{4.3}$$

with $\lambda_{B,0}$ being the unperturbed Bragg wavelength. A schematic comparison between the lasing properties of a Fabry-Pérot structure and a Distributed Bragg Reflector (DBR) laser is presented in figure 4-1 to illustrate the previous discussion. The effective refractive index is changed by some bandgap effects due to current injection and temperature variation. They are described in more detail in [22] but

can be neglected during our experimental work, as explained in this section. On the other hand the value for the laser cavity length is directly related to the emission wavelength of the laser according to equation 4.1 above. When the cavity length changes due to thermal expansion effects, the emission wavelength is automatically affected. Both the refractive index change and cavity length effects are ultimately related to the current injection and temperature tuning methods described next.

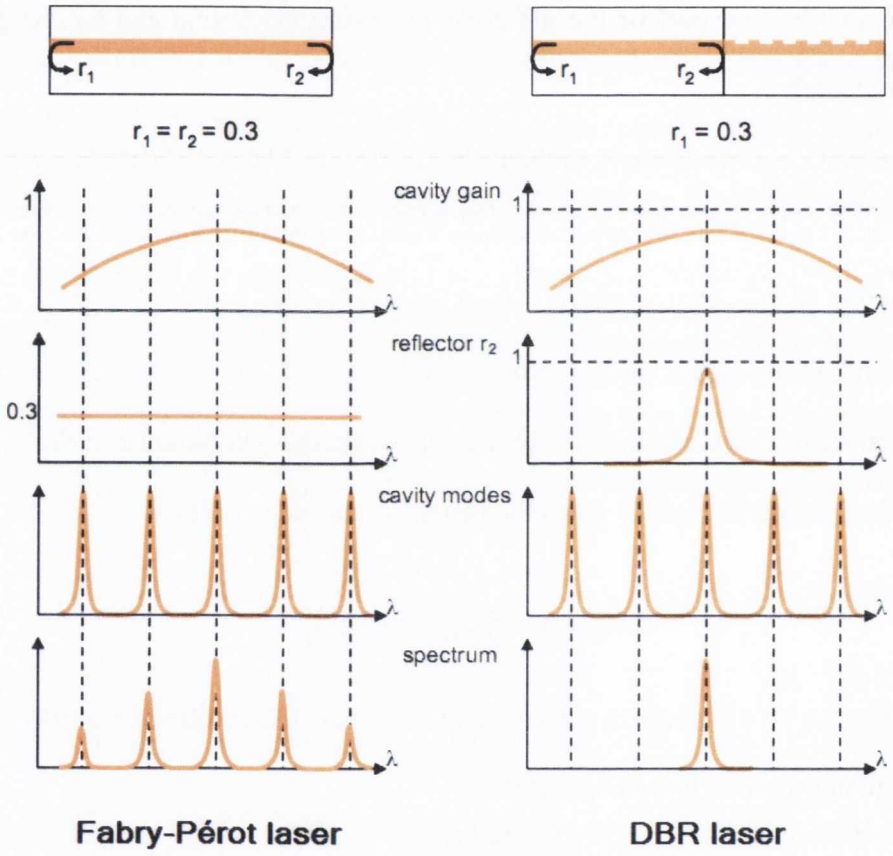

***Figure 4-1**: Lasing in a Fabry-Pérot laser and a Distributed Bragg Reflector (DBR) laser with a wavelength selective reflector. The output lasing wavelength for the DBR laser can be tuned by changing the refractive index of the grating.*

Injection current tuning

The current injected into the laser by the control unit gives rise to two different effects. First, some bandgap effects changing the effective refractive index take

place as described in [22]. Second, the injected current produces a temperature increase of the laser and gives rise to thermal expansion of the cavity. Under normal operational conditions the expansion effect on the emission wavelength is much larger than the bandgap-induced variation, so the latter can be neglected. Only when the injected current into the laser is modulated at very high frequencies are the thermal effects effectively negligible. A well-known rule of thumb is that the emission wavelength of an InP telecom laser emitting around 1550 nm changes at a rate of about 0.01nm/mA.

Thermal tuning

The second effect is that produced by temperature variations of the laser source. These variations can occur due to noise in the thermo-electric cooler unit connected to the laser, or else due to current induced thermal effects as explained above. Thermal expansion of the cavity changes its length, automatically affecting the emission wavelength of the laser. The overall effect is a wavelength increase with increasing temperature, at a rate of approximately 0.1nm/K for a single-mode InGaAs/InP laser emitting in the 1550nm region.

In this manner, it becomes clear how stability of the output wavelength of a laser highly depends on the fluctuations in current or temperature associated with the current and temperature controllers. Low-noise battery-operated current controllers can be used to improve the wavelength stability but still limit the maximum attainable accuracy. Further stability can be obtained by applying locking techniques such as that to be presented in this chapter. Note that these locking techniques compensate for the 1/f noise of the controllers, but do not reduce the linewidth of the stabilised laser source itself. The linewidth of the utilised laser diodes mainly arises as a result of random phase fluctuations due to spontaneous

emission processes within the active region of the lasers. This will be treated in more detail in the next chapter of the thesis.

4.2.2. SATURATION AND THE WM TECHNIQUE

Experimental work presented in this chapter is based on the non-resonant saturation effects and pump-probe experiment described in chapter 3, but an additional feature is included in this case in order to implement a novel laser stabilization technique. This feature consists of merging together the WMS techniques described in chapter 2 and the pump-probe saturation scheme, thereby extending modulation spectroscopy to nonlinear absorption regimes where saturation occurs. Modulation of the laser wavelength at a frequency f produces a well-defined response for each of the detected harmonics at frequencies nf when laser light interacts with the absorbing medium, each of the lineshapes being directly proportional to the n^{th} derivative of the transmitted beam. As an example, experimental curves for the second harmonic response of a WM laser beam probing Gaussian absorption features were presented in figure 2-11 in chapter 2.

However, when switching to the high-power regime saturation of the absorbing transition by the pump control beam occurs and nonlinear absorption takes place. The equilibrium molecular populations of the energy levels involved in the transition are distorted and the resulting absorption lineshape is thus modified, presenting a saturation dip at the gas absorption line centre if the pump spectrally targets that exact resonant value. This has been experimentally confirmed using a pump-probe scheme and results presented in figure 3-11 in chapter 3. If the pump laser was modulated in the same manner as discussed in section 3.3.2 and the optical power was increased then a total of two saturation dips would be observable,

one at each side of the absorption line. Discussion will be limited here to the unmodulated case, but the principles remain valid for both cases. Hence, the key point in evaluating the theoretical WMS harmonic lineshape under these conditions is to clearly understand the role of each of the lasers in the pump-probe experimental set-up. Recalling section 3.3.1 in chapter 3 it becomes clear that both lasers are independent of each other, the pump beam providing enough optical power at the right wavelength to saturate the absorbing transition and the probe beam independently scanning the absorption line (one must remember that the pump and probe lasers can target different gas lines as discussed in section 3.2.2, depending on whether a resonant or non-resonant scheme is used). Thus, because the pump is the beam responsible for creating the saturation feature at the central wavelength and the probe responsible for scanning the spectral absorption profile sensing the nonlinear effect, the clear choice is to use the latter as the modulated source to detect the WMS signature of the saturation dip. Following the same reasoning as presented at the beginning of this section modulation of the probe and detection of the n^{th} harmonic will cause the final signal to be proportional to the n^{th} derivative of the absorption profile, but in this case the profile includes the saturation dip. Because the shape of the saturation dip is also bell-like, but orders of magnitude smaller than the overall absorption line and inverted, the related WMS signature will have the same shape as that of the overall absorbing transition but with opposite sign. That is, the final shape of the n^{th} harmonic of the saturated absorption profile is similar to the superposition of two signals of similar shape, but different scale and opposite symmetry. Note that the shape of such a harmonic is not strictly the superposition of two signals, but only proportional to the n^{th} derivative of the absorption profile that has been modified in the nonlinear regime.

The mathematical description of these harmonics depends on the gas pressure regime targeted during experimental work. As discussed in chapter 2, the lineshape of an absorbing transition at low pressures is described by a Gaussian function *G(x)*, because in that case Doppler broadening dominates and is proportional to the Gaussian-shaped Maxwell-Boltzmann molecular speed distribution of the gas. At high pressures a Lorentzian function *L(x)* applies because collisional broadening dominates and is described by a Lorentzian lineshape. In our case the low-pressure Gaussian lineshape applies, because we are working at values of few mbar. On the other hand the lineshape of the saturation dip is given by a Lorentzian function $L_{SAT}(x)$ to a first approximation, as discussed in section 3.4.1 in chapter 3. Hence, the final lineshape $L_{FINAL}(x)$ of the saturated absorption profile can be described either by a Lorentz-Lorentz (*L-L*) model or a Gauss-Lorentz (*G-L*) model, according to the relations

$$L_{FINAL}^{L-L}(x) = L_{LORENTZ}(x)[1 - L_{SAT}(x)] \tag{4.4}$$

$$L_{FINAL}^{L-G}(x) = G(x)[1 - L_{SAT}(x)] \tag{4.5}$$

where the generic Lorentzian and Gaussian lineshapes are respectively given by

$$L(x) = \frac{2A}{\pi}\frac{w}{4(x - x_C)^2 + w^2} \tag{4.6}$$

$$G(x) = Aexp\left[\frac{-(x - x_C)^2}{(w/2\sqrt{ln2})^2}\right] \tag{4.7}$$

The parameters *A*, *w* and x_C respectively correspond to an amplitude scaling factor, full-width at half maximum (FWHM) and independent variable central point (an assumption is made that both the Lorentz/Gauss and saturation Lorentzian functions are centred around the same value). These models, illustrated in figure 4-2, include theoretical curves for the first (*1f*) and second (*2f*) harmonics of a saturated

absorption lineshape (*0f*) centred at $x_C = 0$ for both Lorentz-Lorentz and Gauss-Lorentz models, with the amplitude and width factors chosen so that $A_{LORENTZ,\ GAUSS} = 1$, $w_{LORENTZ,,GAUSS} = 1$, $A_{LORENTZ,GAUSS}/A_{SAT} = 3$ and $w_{LORENTZ,GAUSS}/w_{SAT} = 10$. As discussed above, the Gauss-Lorentz model applies in our experimental case.

On the other hand, a very important issue to take into account when applying WMS techniques is the dependence of the final lineshape on the modulation depth of the modulated laser. As discussed in section 2.2.6 in chapter 2, the amplitude of any 1f and *2f* signals obtained applying this technique depends on the modulation depth of the corresponding laser source, making it possible to optimize the signal of interest for a given set of experimental conditions. Maximum amplitude is achieved when the modulation depth is of the same order of magnitude of the linewidth of the absorption feature, decreasing otherwise. In the case of a saturated absorption line two different features are involved: the overall broadened gas line, of the order of hundreds of MHz wide at few mbar of pressure, and the narrow saturation dip, of the order of tens of MHz wide at the same pressure values. Taking this into account, there can be two different scenarios for the final 1f lineshape of the saturated absorption line: if the modulation depth is of the order of magnitude of the overall gas line, then the amplitude of the overall 1f will be maximum and the amplitude of the saturated 1f at the line centre will be significantly reduced; in the opposite case, the amplitude of the overall 1f will decrease and that of the 1f of the saturation dip in the line centre will increase. The final decision depends on the characteristic of interest for a given experiment and conditions, providing the best output in each case.

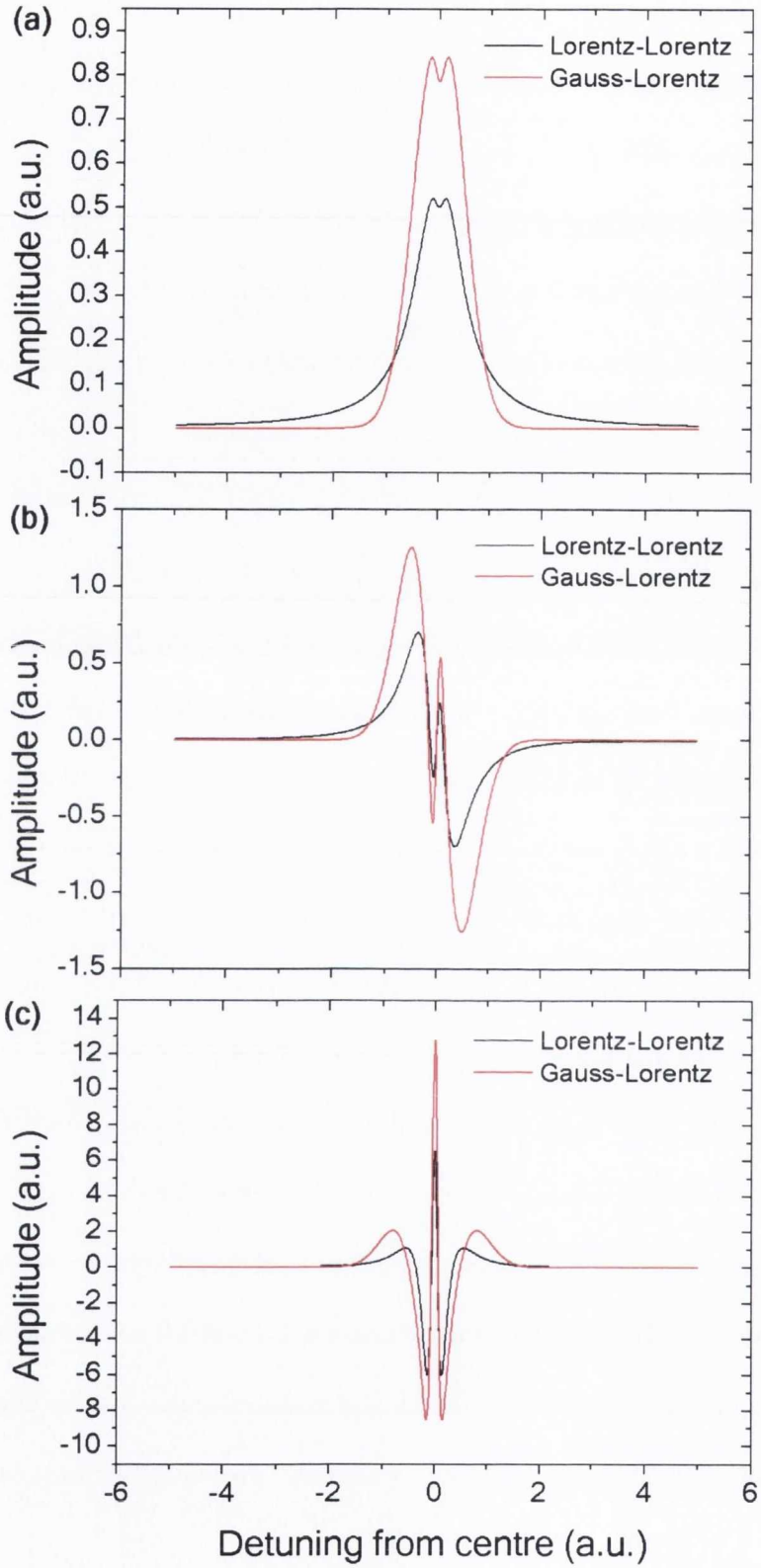

***Figure 4-2**: Theoretical curves for Lorentzian L(x) and Gaussian G(x) lineshapes centred at $x_C = 0$ presenting a Lorentzian saturation dip $L_{SAT}(x)$ at the line centre (a) and the corresponding first (b) and second (c) harmonics.*

Regarding the laser stabilization technique presented in our case, modulation depth is chosen to maximise the amplitude of the first harmonic of the saturation. This improves the overall locking response of the locking technique as discussed in the upcoming section 4.3.2 and illustrated in figure 4-9.

4.2.3. FEEDBACK CONTROL LOOPS AND LASER LOCKING

Feedback control loops

It is common to find dynamic physical systems where one or more of the outputs drift with time and need to be stabilised to a reference value. These kind of systems are widely spread both at macroscopic and microscopic scales with examples including temperature regulation in buildings, microscopes where vibrations need to be minimised and effectively suppressed or cruise speed control associated with different means of transport such as cars or ships. In order to stabilise the desired output a certain signal is chosen which contains the relevant information to assess the stability, and then processed before being fed back to the system *S* implementing a loop structure. A schematic diagram corresponding to a simple case is presented in figure 4-3, where only one time-dependent output parameter needs to be stabilised and its magnitude *y(t)* become exactly equal to that of a chosen reference value *r(t)* at all times.

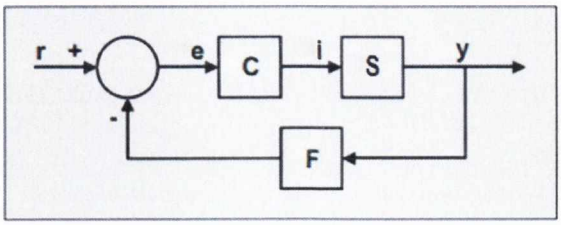

***Figure 4-3**: Schematic diagram for a feedback control loop to stabilise a dynamic system S.*

In the ideal case where the output is stable in time the condition $y(t) = r(t)$ holds. However, under normal operation conditions the magnitude of the output of interest drifts with time from the desired value. In that case the output signal is collected by a sensor scheme F and subtracted from the reference signal, defining a finite error signal $e(t) = r(t) - y(t)$. This signal is a measure of the departure of the system from its stable state and its magnitude relative to the output is typically small. A controller C receives this error signal and generates the input value $i(t)$ to be finally fed back to the system S. In the ideal case of successful implementation of a stabilization loop this input value compensates the undesired system drift. The error value asymptotically approaches zero within some stabilizing time interval, which will be characteristic of the physical process involved in the system and can be defined as the system time constant τ_{SYS}. It is customary to define such an arrangement as an ***active feedback loop***. Small signal analysis is usually applied in this type of loops as the magnitude of the error signal is much smaller than the system output, and compensation for the undesired drift thus carried out in a linear regime. Transient behaviour becomes important when the loop is initially closed, and conditions must be chosen to assure that the magnitude of the error signal does not exceed a certain limit during the associated transient time scale. On the other hand the frequency response of the loop is determined by its effective time response τ_{SYS}, as introduced elsewhere in this section, and the active loop will be only able to compensate system drifts whose associated time scale τ_{DRIFT} is longer than that effective response. The reference value in the feedback loops implemented during our experimental work is equal to zero, simplifying the required experimental arrangement as presented in sections 4.3.1 and 4.3.2.

Laser frequency locking

Active feedback loops can be applied to stabilization of a laser output frequency, extending the previous discussion to this particular physical system. The emission frequency of a laser source exhibits some finite drift in time under normal operation conditions, mainly due to *1/f* noise in the laser controllers as discussed in section 4.2.1. This becomes a serious drawback in fields where frequency stability plays a crucial role (such as optical metrology or precise frequency referencing), so active feedback loops can be applied to minimise such noise effects.

Figure 4-4 below includes the experimental scheme to implement an active feedback loop in order to lock the optical frequency $\upsilon(t)$ of a laser source, making use of a spectral feature of gas in an absorption cell. According to the terminology introduced in the previous discussion this frequency is now the output of the system to be stabilised $y(t) = \upsilon(t)$.

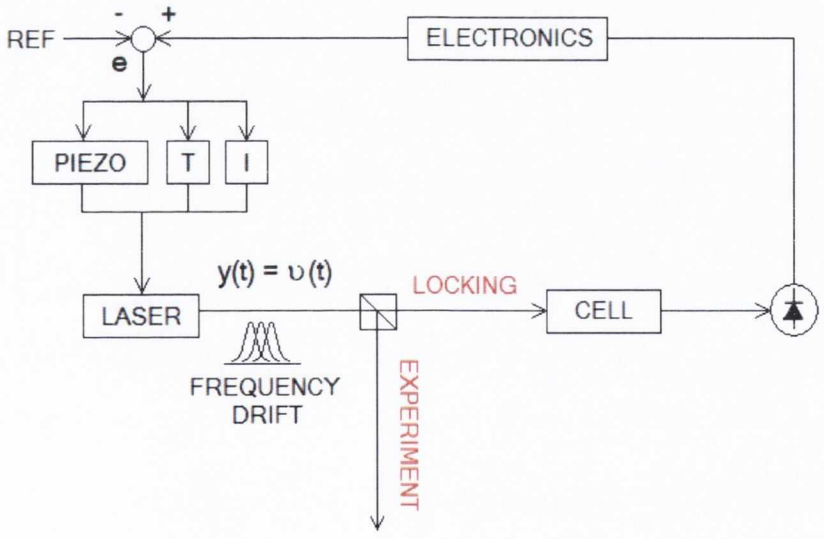

***Figure 4-4**: Schematic representation of an experimental scheme including an active feedback loop to lock the operating frequency of a laser, based in a gas absorption cell.*

A usual arrangement is that where the main beam is divided in two with the help of a suitable splitting element and a small fraction used for locking purposes, while the remaining light is sent towards the main experiment to be carried out. In order to implement the locking loop, the correspondent beam first travels through the gas absorption cell. This gas absorption feature acts as a frequency discriminator, and the output light is detected with a high-speed photodiode (equivalent to the sensor measurement F in figure 4-3). The photodiode output signal usually needs to be processed by locking electronics (also equivalent to the sensor measurement block F in figure 4-3), that provides some control voltage to be mixed with the reference value to extract an error signal e. This signal is finally fed back to the laser input control system via a controller C in order to counteract for any undesired drift. As shown in figure 4-4, several possibilities arise for implementation of this controller depending on each specific case: External Cavity Lasers (ECLs) can be stabilised by feeding the control signal back to the piezo controller associated with the external grating or the laser optical cavity length [10, 11]; Distributed Feed Back (DFB) lasers can be stabilised by feeding the signal to the Thermo-Electric Cooler (TEC) unit controlling its temperature and thus the cavity length, or more usually connecting the control signal to the laser input current unit. Performances of each of these methods vary in the frequency domain; conventional ECL's have piezo resonances of the order of 1 kHz which can limit the locking bandwidth; temperature and current stabilization of DFB lasers depend on the modulation bandwidth of the corresponding control units.

4.3. EXPERIMENTAL SET-UP

4.3.1. UNSATURATED LASER STABILISATION

In the first part of our experimental work the laser frequency stabilisation technique is implemented under a non-saturation regime. This will illustrate and prove the basic working principles of the locking method and help with the understanding of the saturation-based approach presented in the next section. The experimental arrangement implemented is shown in figure 4-5 below, involving only one single laser as opposed to the two-laser pump-probe scheme presented in chapter 3. In order to maintain the same experimental conditions during our research period, the original pump-probe set-up was not dismantled but one of the beams is simply blocked.

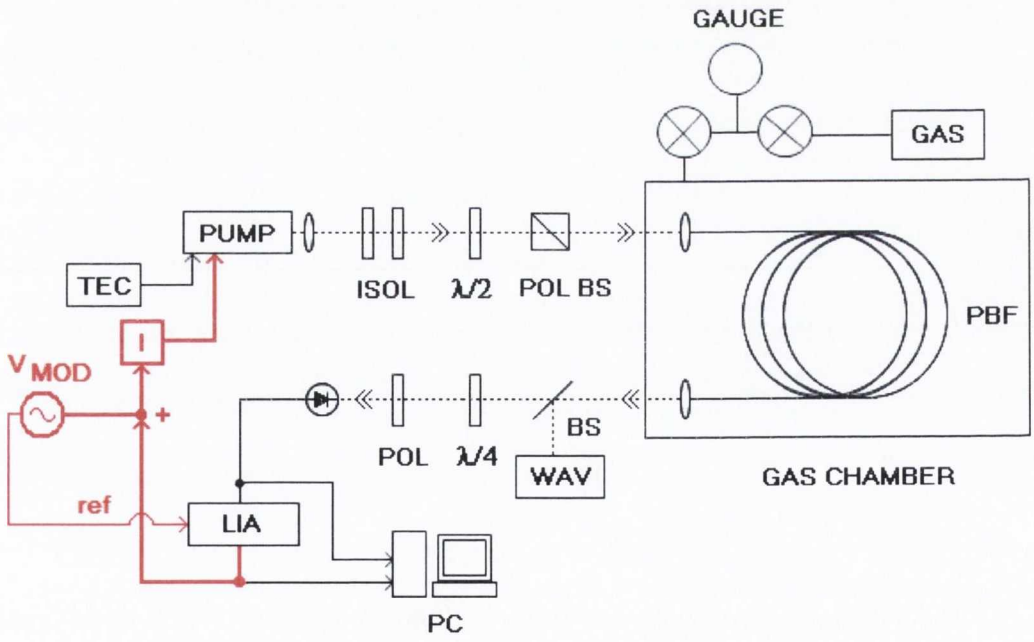

***Figure 4-5**: Schematic diagram for the set-up used to stabilise the pump laser emission frequency without saturation effects.*

Because we are interested in the frequency stabilisation of the high-power DFB laser diode used as the pump, the blocked beam is that of the probe. The polarisation-dependent elements previously used to separate both beams still remain in place but do not affect the stabilisation results in this case. They were readjusted for maximum transmission of the pump laser in this case. Because this technique is applied under a non-saturation regime, the pump laser optical power is now decreased.

In this new scheme Wavelength Modulation (WM) techniques and an active feedback loop are introduced, as discussed in sections 4.2.2 and 4.2.3. The pump laser emission frequency is modulated with a signal V_{MOD} connected to the modulation facility input of the current control unit *I*. The output signal from the photodiode is fed to a lock-in amplifier (LIA), referenced at the modulation frequency f_{MOD} so that its output $y(t)$ (following the notation introduced in section 4.2.3) corresponds to the first derivative of the input signal $1f(t)$. On the other hand, an active feedback locking loop is implemented by connecting the lock-in voltage output to the modulation facility integrated in the precision low-noise current source driving the pump laser. This modulation facility generates an output current proportional to the input voltage, so the total current eventually injected into the pump laser is a combination of both the set point plus this additional contribution. In essence, the aim of the locking technique is to provide the conditions under which the frequency drift related to the laser is counteracted and effectively nullified by such a loop contribution. Given this experimental set-up, the key point in order to achieve frequency stabilization is to set the pump emission frequency at the corresponding absorption line centre so that $y(t) = 1f(t)_{CENTRE}$. In the ideal case where the frequency does not drift in time the $1f$ amplitude at the line centre is zero

according to figure 4-2b and the condition $y_{IDEAL}(t) = 1f_{CENTRE} = 0$ applies. This defines the reference value for the control loop to be $r(t) = y_{IDEAL}(t) = 0$ so that the error signal satisfies $e(t) = y(t) - r(t) = y(t)$ and corresponds directly to the lock-in output. However, in the real case, the emission wavelength of the pump laser drifts in time due to temperature and current perturbations and a non-zero error signal $e(t) \neq 0$ is generated. In order to compensate for this drift the relative shape of the 1f signal is chosen so that a negative drift of the laser frequency $\Delta\upsilon_{PUMP} < 0$ corresponds to a positive output amplitude $y(t) > 0$ and vice versa. This is achieved by manually setting the sign for the lock-in gain, and in this manner the frequency correction introduced by the control loop counteracts the former laser drift as illustrated in figure 4-6 below.

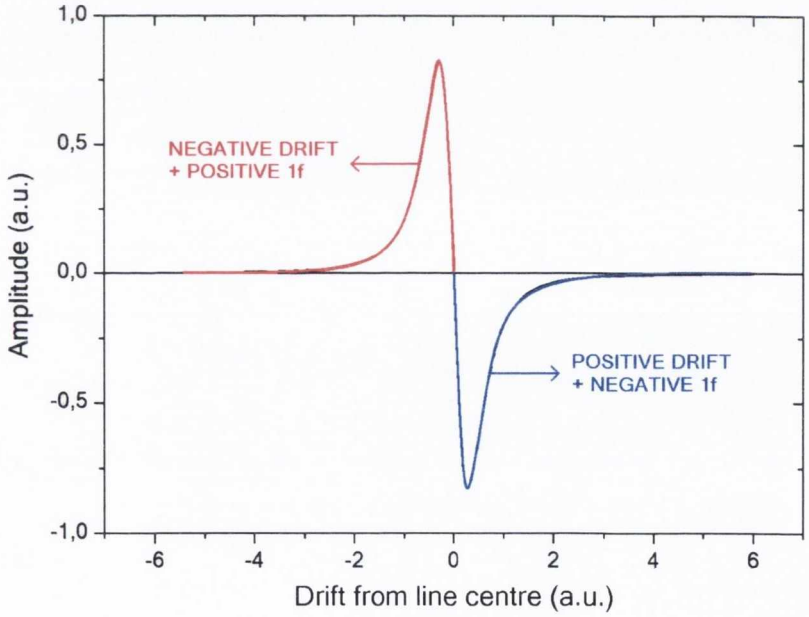

***Figure 4-6**: Schematic representation for the stabilization behaviour introduced by the feedback loop without saturation effects. When the pump frequency drifts in a positive manner the magnitude of the unsaturated 1f feature at the line centre becomes negative and vice versa.*

This technique allows for the emission frequency of a laser to be stabilised, though it presents a major drawback: frequency stabilisation is achieved at the expense of having to modulate the frequency itself. This decreases the attainable accuracy for absolute frequency stabilisation, thus limiting the number of potential applications based on this technique. The saturation-based stabilisation scheme presented in the next section overcomes this disadvantage, significantly improving the absolute frequency stabilisation results.

4.3.2. SATURATED LASER STABILISATION

The second laser stabilisation scheme makes use of saturation effects, and is essentially an extended pump-probe set-up (similar to that used in chapter 3, figure 3.7). The new configuration is presented in figure 4-7 below.

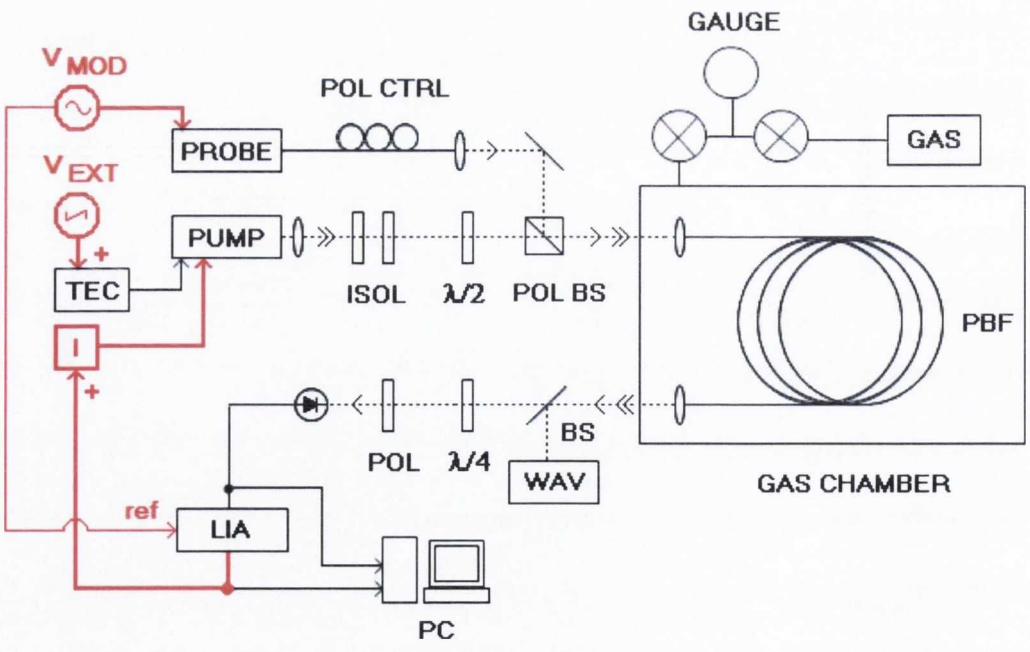

***Figure 4-7**: Schematic diagram for the extended pump-probe set-up used to implement WMS detection techniques and an active feedback loop to stabilise the pump emission frequency. The set-up is based on that presented in figure 3-7 but has been modified, with additional components shown in red for clarity.*

In this extended scheme two laser sources are used, corresponding to the same ECL laser (probe) and the high-power DFB laser diode (pump). The frequency of the ECL laser is now modulated by means of an external signal V_{MOD} applied to the modulation facility integrated into the laser module. This allows for application of WMS techniques using a lock-in amplifier LIA, which is referenced to the probe modulation frequency f_{MOD}. The lock-in output $y(t)$ thus corresponds to the amplitude of the first-harmonic of the input signal, $y(t) = 1f(t)$. Polarization of the beams is again controlled using suitable optical components and the relative polarisation of the beams is set in the same way as explained in chapter 3 to block the pump beam before reaching the measuring photodiode. The locking loop is implemented in a similar fashion as in the unsaturated experimental scheme, but now there is a fundamental difference: the output of the lock-in is not fed back to the modulated laser, but rather connected to the modulation facility input of the unmodulated source –the pump laser. The total current driving the pump laser is now a combination of the feedback contribution plus the set point, and the aim of the feedback loop remains the same as that stated in the previous section: both contributions must cancel each other and effectively nullify any pump laser frequency drift.

In order to achieve this cancellation, both the probe and pump laser frequencies are set to their respective absorption line centres. Because the pump is now operated at high optical powers, this means that a reduction in absorption (a saturation dip) is created at the centre of the probe transmission spectrum. The result is that the output of the lock-in corresponds to the signal at the centre of the first harmonic of the saturation dip, $y(t) = 1f_{CENTRE}^{SAT}(t)$. From this point on the same working principle applies for the feedback locking loop as with the unsaturated case: the generated

error signal $e(t) = y(t)$ is fed back to the pump current control unit; in the ideal case there is no pump frequency drift and $e(t) = 0$ for all times; in the real case a small amplitude $e(t) \neq 0$ is generated, and introduces an extra contribution to the total current driving the pump laser. The shape of the saturated 1f signal is chosen so that the frequency change introduced by this extra current counteracts the former laser drift, and frequency stabilization is achieved. A very important difference applies in this case: this technique allows for the emission wavelength of the pump laser to be stabilised **without** any modulation applied to it, a novel feature as pointed out in the chapter introduction. This is a major improvement as compared with the unsaturated scheme presented in section 4.3.1, allowing for high-accuracy absolute frequency stabilisation of a high-power laser source. Figure 4-8 illustrates the present discussion in an equivalent way as figure 4-6 does for the unsaturated case.

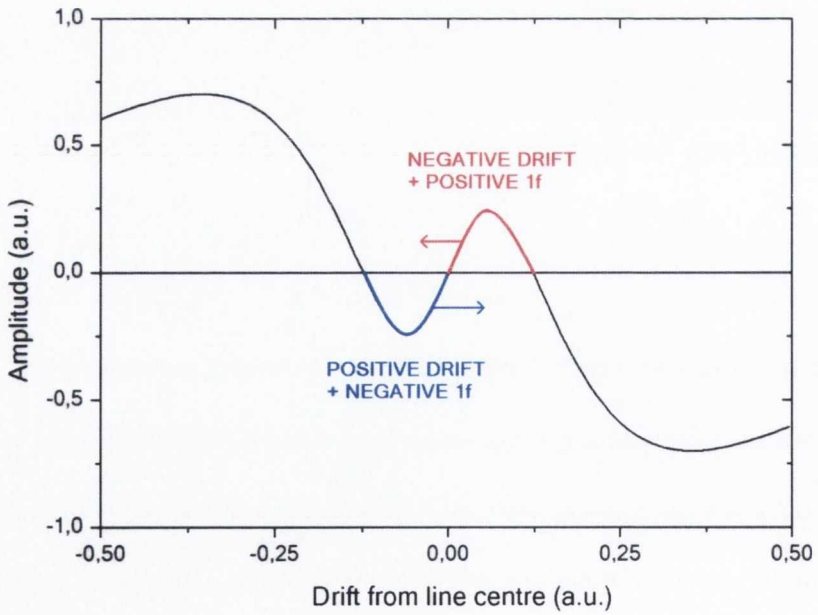

***Figure 4-8**: Schematic representation for the stabilization behaviour introduced by the saturation-based feedback loop. Only the central region containing the saturated 1f signature is shown for clarity reasons, as its spectral width is much narrower than that of the overall 1f signal.*

Note that in the saturated case the pump laser frequency noise causes the narrow 1f feature at the line centre to move across the overall static probe 1f lineshape, while in the unsaturated case the whole 1f lineshape remains unperturbed.

The response of the frequency locking loop can be further optimised by adjusting the modulation depth applied to the probe laser. The value for the modulation depth determines the peak amplitude of the first harmonic of the saturation dip, so it can be maximised as discussed in section 4.2.2. Because such signal corresponds to the error signal fed back to the pump laser current control unit, increasing its peak amplitude means that bigger noise signals V_{NOISE} affecting the laser can be nullified. Figure 4-9 below illustrates the current discussion comparing two traces with different 1f saturation amplitudes.

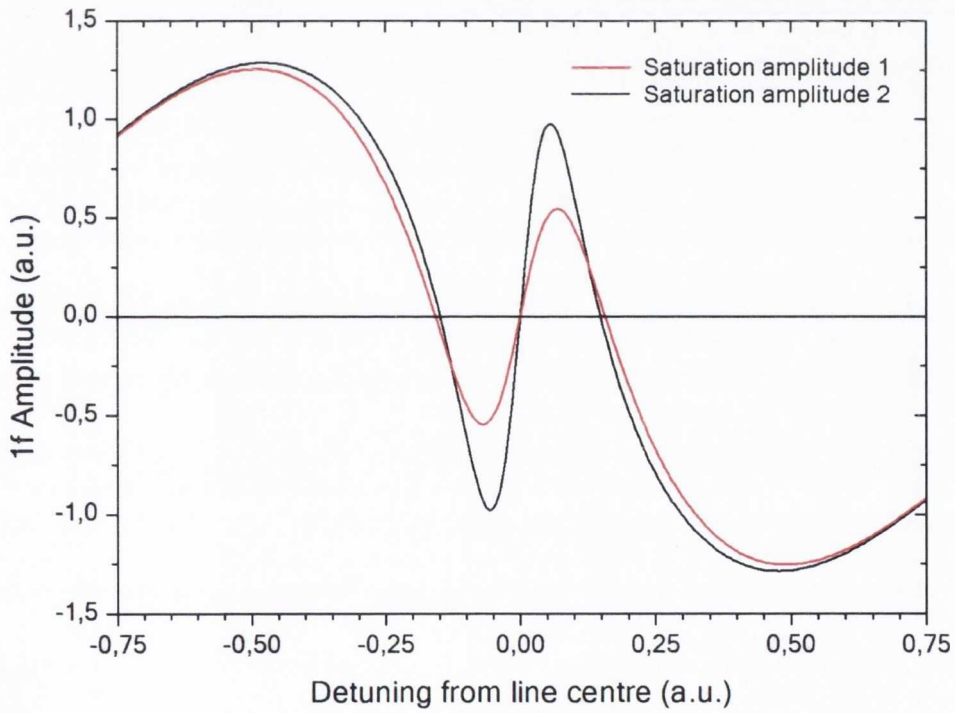

***Figure 4-9**: Theoretical curves for the first harmonic (1f) of a Gaussian absorption profile exhibiting a Lorentzian saturation dip of two different amplitudes at the line centre.*

Note that the experimental scheme described in this section is used to obtain the WMS results presented in section 4.4.1 by simply disconnecting the active feedback loop.

4.4. RESULTS AND DISCUSSION

4.4.1. WMS SATURATION OF NON-RESONANT TRANSITIONS

The first part of this experiment is based on the non-resonant saturation results presented in chapter 3 so similar experimental conditions apply, with the pump laser diode still targeting the P(13) gas line centred at 1532.830 nm and the probe wavelength tuned across the R(11) line at 1519.137 nm. As previously mentioned in section 4.3.2 the experimental set-up corresponds to that presented in figure 4-7, but in this case the active feedback loop is not closed. The measured output powers of the pump and probe lasers are again approximately 100 mW and 5 mW respectively and maximum coupling into the PBF of approximately 50% is achieved. The coupling was optimised to avoid transmission ripple effects as discussed in section 3.3.1 in chapter 3. Under optimum coupling the central peak of the quasi-Gaussian intensity profile in the core of the PBF is enhanced and transmission becomes maximum. In order to apply WMS techniques the probe laser is now modulated with a sinusoidal signal of frequency f = 2.430 kHz, which also references the processing lock-in. Modulation depth is on the other hand optimised to achieve the maximum amplitude for the 1f signature of the saturation dip as discussed in the previous section 4-3, improving the locking response. The gas temperature and

Acetylene gas partial pressure are respectively T = 22°C and 1 mbar while the total pressure in the gas chamber including the residual air present is 3 mbar.

Results for the first-harmonic WMS detection of the saturated transition are presented in figure 4-10 below, with a lineshape in very good agreement with the theoretical curves shown in figure 4-2b.

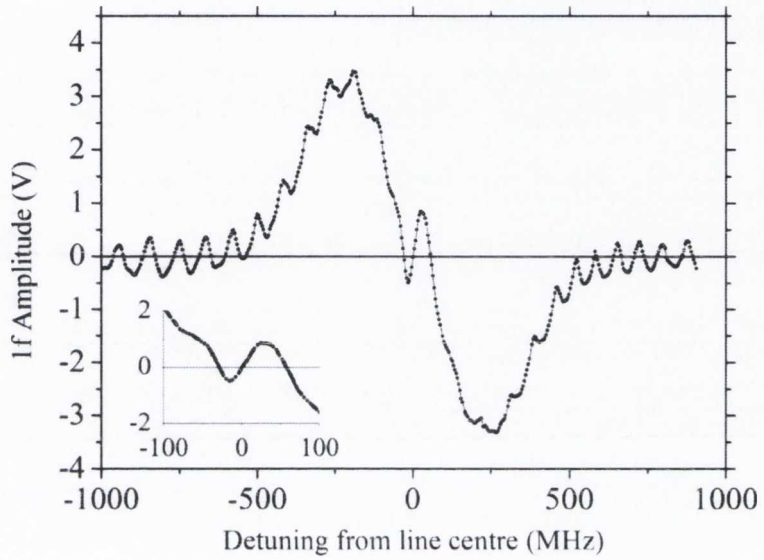

***Figure 4-10**: Experimental results for the first-harmonic WMS signal of the saturated probe transmission spectrum at a partial pressure of 1 mbar of Acetylene. Residual coupling reflections together with ripples in the transmission spectrum of the PBF account for the observed interference pattern in the background.*

As discussed in section 4.2.2 the overall lineshape is proportional to the first derivative of the probe transmission spectrum including the saturation dip, and consists of the 1f signature from the Doppler broadened gas line with the narrow saturation dip. The zero-crossing of the saturation dip can be clearly observed approximately at the line centre, with a measured peak-to-peak width of approximately $\Delta\upsilon^{1F}{}_{SAT} \approx 50$ MHz as clearly shown in the inset. Residual coupling

reflections in the system account for the periodic pattern in the background. The scan rate for the probe frequency was chosen to avoid effective averaging effects due to *1/f* noise present in the system, as discussed in section 3.4.1 in chapter 3.

4.4.2. LASER STABILIZATION

Unsaturated laser stabilisation

The experimental scheme is set following the description in section 4.3.1 and the optical power of the pump laser beam decreased to a value of approximately $P_{PUMP} \approx 5$ mW at the input of the fibre. This produces a red-shift of the operating wavelength of the laser, so now the P(11) absorption gas line at 1531.588 nm is targeted within the P-branch of the acetylene v_1+v_3 absorption band. The current of the DFB pump laser is tuned and the first harmonic of the transmitted spectrum recorded as shown in figure 4-11. As can be observed the signal profile is in good agreement with that presented in figure 4-6, a necessary condition to implement the frequency locking loop. A finite shift of the baseline from its expected zero-value can be observed, and is attributed to a residual offset introduced by the measuring lock-in amplifier.

The feedback loop to lock the pump laser frequency to the centre of the absorption line is then implemented. The laser frequency is set to the P(11) line centre and the output of the measuring lock-in connected back to the laser current control unit, as discussed in section 4.3.1. A small fraction of the PBF output beam is directed to a wavemeter using a beamsplitter to monitor the wavelength.

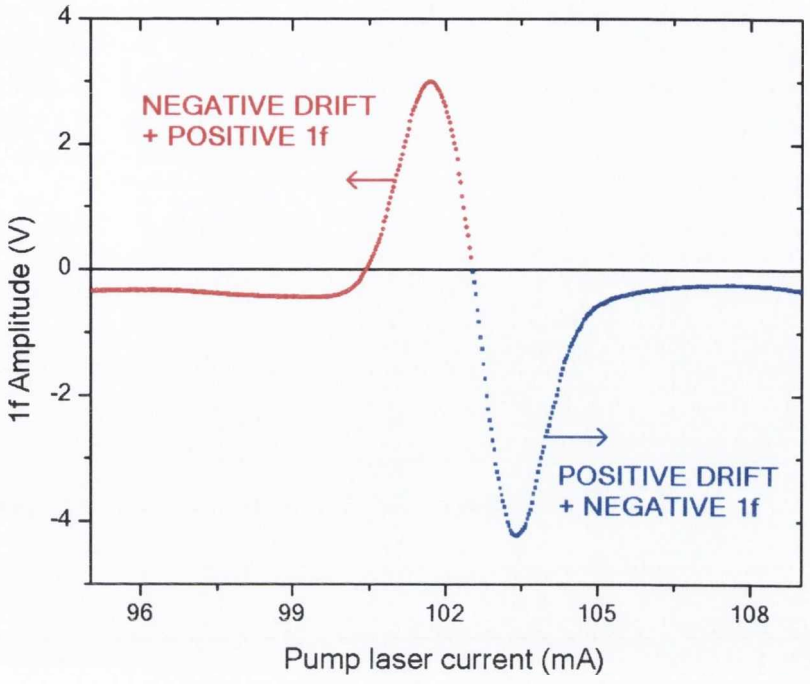

***Figure 4-11**: Experimental trace for the first harmonic of the pump laser P(11) absorption line. The signal exhibits an appropriate shape to implement a frequency loop, counteracting the laser drift. The observed shift of the baseline from its ideal zero value attributed to a residual lock-in offset.*

Results for the successful implementation of the locking loop are presented in figures 4-12 and 4-13. In order to assess the proper functioning of the frequency locking loop, the feedback signal is first disconnected and the temperature of the pump laser increased. This leads to a linear increase in the emission wavelength of the laser, as shown in the corresponding trace of figure 4-12. When the locking loop is closed the temperature-induced wavelength change is compensated by the feedback signal and the wavelength remains constant, as observed in the second trace in the same figure. The working principle of the locking loop, discussed in section 4.3.1, is now illustrated in figure 4-13. Starting at a set point T_{SET} = 21.5 °C the temperature is raised up to T_{SET} = 21.9 °C; the temperature is changed in 0.1°C steps, maximum precision achievable with the corresponding thermo-electric cooler

controller connected to the pump laser. For each of the 0.1°C intervals the temperature changes with time and asymptotically reaches its steady value, as observed in the corresponding trace. On the other hand, the error signal introduced by the locking loop compensates for this temperature-induced wavelength change as shown in figure 4-13. The shape of the error signal exactly replicates that of the temperature change, but with an opposite sign. This effectively nullifies the laser drift and stabilises its emission wavelength to the line centre. As discussed in section 4.3.1, the drawback of this technique is the necessity of modulating the emission wavelength itself to implement the locking loop.

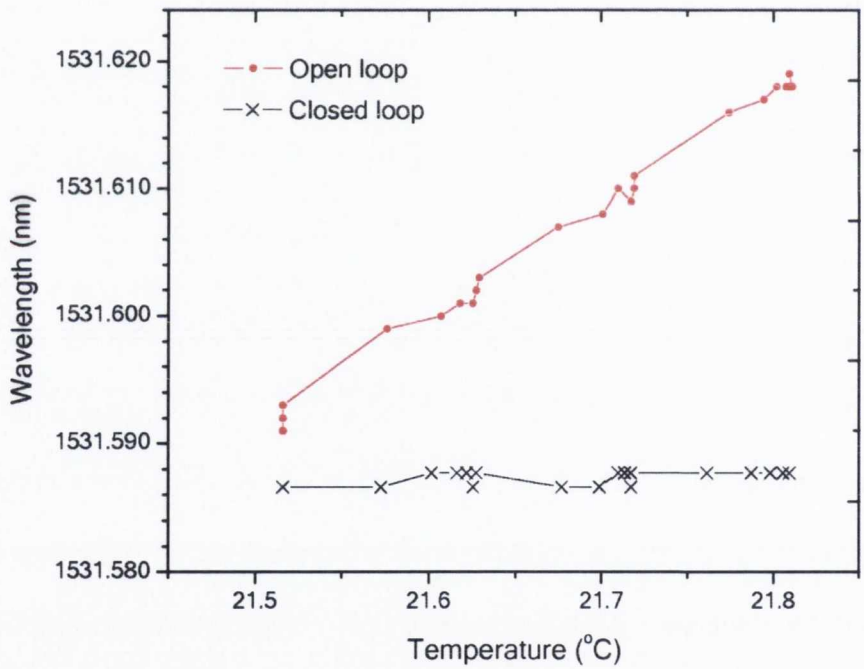

***Figure 4-12**: Comparison of the pump laser emission wavelength at different laser temperatures for an open and closed feedback locking loop. When the loop is open (dots, red) the wavelength of the laser increases linearly with temperature. When the loop is closed (crosses, black) the temperature-induced wavelength change is counteracted by the loop and the wavelength remains constant. Precision of wavelength measurements is limited to ±1pm by the measuring wavemeter.*

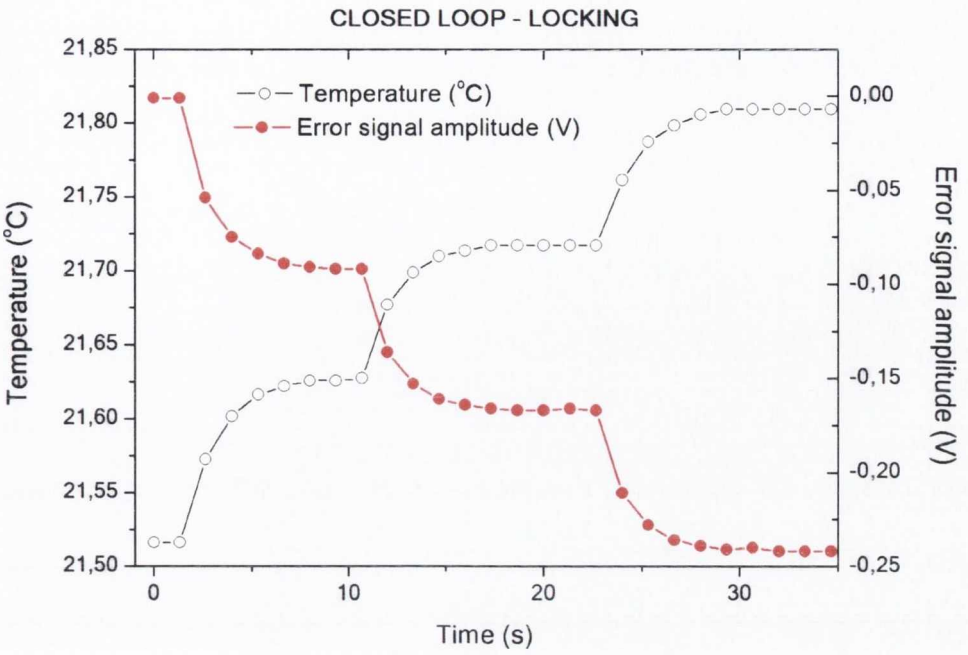

***Figure 4-13**: Comparison of the induced laser temperature change and corresponding error signal introduced by the frequency locking loop when it is closed. The temperature (open dots, black) is changed in 0.1°C steps and asymptotically reaches its steady value for each interval. The error signal (solid dots, red) exactly replicates the behavior of the temperature curve but carries an opposite sign. This compensates for the temperature-induced emission wavelength change and stabilises the wavelength value to the centre of the absorption line, as measured in figure 4-12.*

Saturated laser stabilisation

In the second part of the experiment both the probe and pump lasers are used and the experimental scheme implemented as described in section 4.3.2. The probe laser targets the R(11) absorption line centre at 1519.137 nm within the v_1+v_3 absorption band of acetylene while the pump laser is again operated at high optical powers and now targets the P(13) line centre at 1532.830 nm. The measured optical powers at the fibre input are approximately 5 mW and 40 mW respectively. The frequency locking loop is implemented as described in section 4.3.2 by connecting the output

of the lock-in amplifier LIA to the modulation facility integrated in the low-noise current controller unit driving the pump laser. Experimental results for the first harmonic of the saturated absorption profile presented in figure 4-10 show that the feedback signal has the appropriate shape to implement the frequency stabilization loop, with figure 4-14 below in good agreement with the corresponding theoretical trace shown in figure 4-8. This signal has a peak-to peak width of approximately 50 MHz, while some existing schemes achieve widths of ≈ 10 MHz (large core HC-PBF's, Radio Frequency (RF) techniques [17]) or ≈ 700 kHz (ECL lasers and Fabry-Pèrot cavities, [10]), but they usually require more complex experimental set-ups.

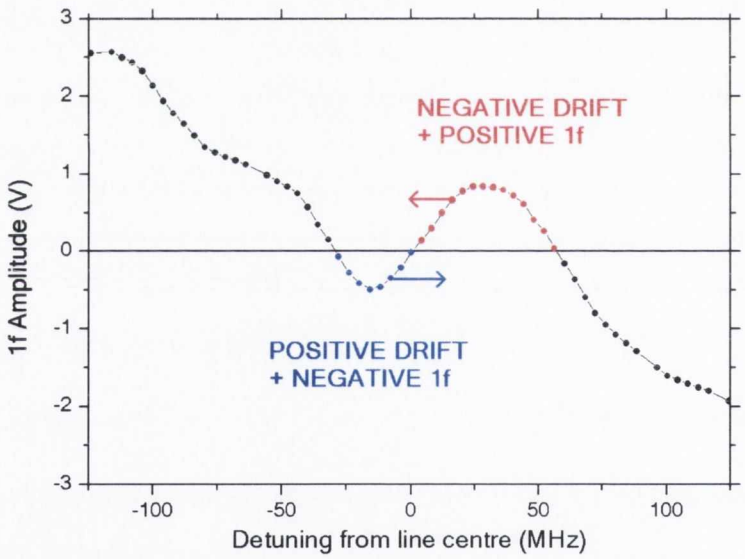

***Figure 4-14**: Central region of the experimental trace presented in figure 4-10 for the first harmonic of the saturated probe transmission spectrum. The saturated 1f signal at the line centre is used as the feedback signal to implement the saturated locking loop.*

Results for the successful implementation of this technique for a steady pump laser temperature are presented in figure 4-15. The temperature of the high power DFB

laser diode is set at T = 21.5°C and the frequency drift is first measured when the active feedback loop is open. The DFB wavelength drift in time without any control loop is measured by coupling the laser beam into a single mode fibre and sending it to a calibrated gas cell containing 5 mbar of Acetylene and 5 mbar of HCN. The laser emission wavelength is set at the Acetylene P(13) absorption line centre and the diode is externally modulated with a sinusoidal signal at a frequency of f = 2.4 kHz in order to apply WMS detection techniques. The amplitude of the 1f trace at the line centre is then recorded in time, being directly proportional to the laser drift according to the discussion in section 4-2. This measuring technique also makes the frequency drift measurement insensitive to any finite coupling-induced power changes that might take place, because the signal amplitude at the 1f centre is zero and small changes in the optical power coupled into the gas cell do not significantly change the slope of the first harmonic trace at the line centre. Typical DFB laser drifts of more than 10 MHz are measured as presented in figure 4-15 and then significantly reduced to a root mean square (RMS) value of $\Delta\upsilon_{RMS} = \sqrt{1/N \sum_{i=1}^{N} \Delta\upsilon_i^2} = \mathbf{180\ kHz}$ around the line centre when the feedback loop is closed for a total time greater than 2 minutes. Deliberate perturbations of the pump DFB temperature were introduced in the system by changing the air flow surrounding the chip-on-carrier mounted laser diode while the feedback loop was closed. These perturbations (at approximately 28 seconds and 55 seconds) were compensated by the control loop while keeping the laser emission wavelength constant at the gas line centre, as shown in the corresponding trace.

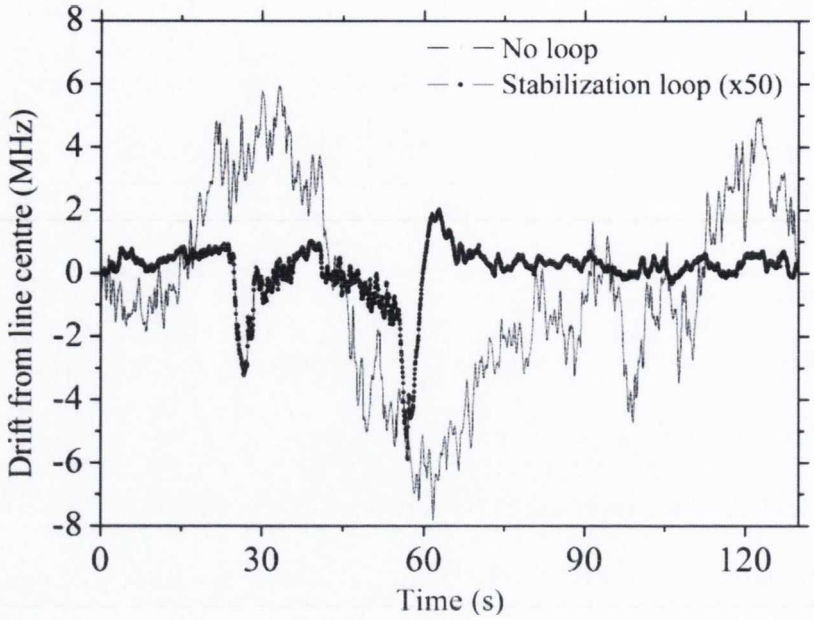

***Figure 4-15**: Comparison of pump laser emission frequency drift at constant laser temperature with and without implementation of a control loop. Slight temperature perturbations at approximately 28 s and 55 s are compensated as observed in the corresponding trace (amplified by a factor of 50 for clarity).*

In order to further demonstrate the stabilization capabilities of this technique, the laser diode temperature was changed in a controlled manner while the feedback loop was in operation. The Thermo-Electric Cooler unit responsible for controlling the pump laser temperature allows a minimum temperature change of 0.1°C when operated remotely via a GPIB interface, so additional resolution is needed in order to change the laser temperature in small increments. To achieve such fine temperature control a simple external electronic circuit was connected to the external thermistor input facility integrated in the unit. The circuit consists of a DC voltage source of maximum value V_{EXT} = +10 V which can be remotely tuned plus a resistor of magnitude R=5 kΩ connected in series so that the output voltage provided by the circuit is reduced to the mV scale. This voltage is directly connected to the terminals of the thermistor voltage reading in the TEC unit, so that

the total voltage magnitude sensed by the instrument is the sum of the real signal originated from the thermistor in the laser diode chip plus an external contribution equivalent to a *virtual* temperature change. In this way the response of the unit and thus the pump laser temperature can be precisely controlled by varying the external voltage supplied.

Successful results for the implementation of such a technique are presented in figure 4-16, which shows the error signal amplitude increasing in time to compensate for a total temperature change of the DFB laser of $\Delta T = 0.05°C$.

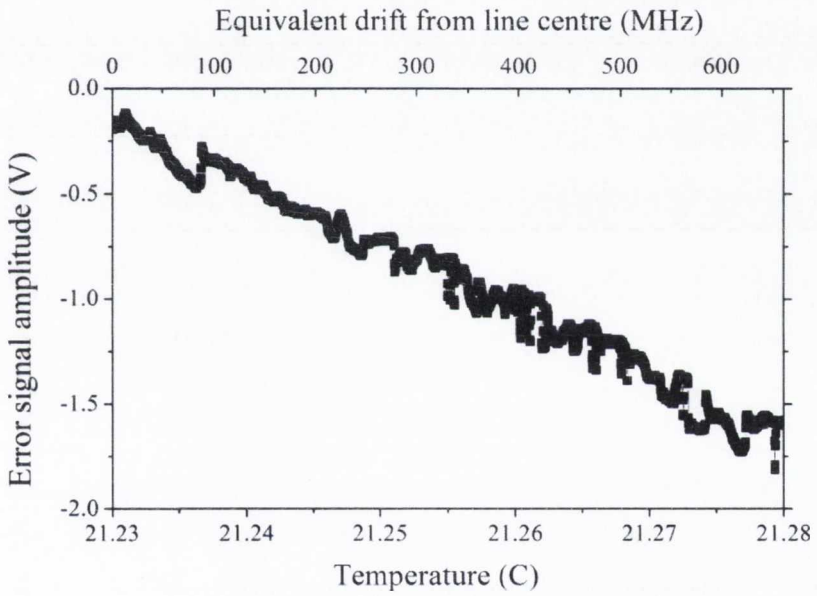

***Figure 4-16**: Error signal amplitude as a function of pump laser temperature with the stabilization loop implemented.*

This error signal exactly counteracts the frequency drift introduced by the temperature change of the laser, included in the figure as an additional scale after calibration. The total drift corresponding to the temperature change of $\Delta T = 0.05°C$ exceeds 650 MHz, significantly bigger than the measured absorption line Doppler linewidth of $\Delta\upsilon_D = 470$ MHz. In this way the locking loop can stabilise the laser

emission frequency even under the presence of slight temperature variations that might be present under normal operational conditions. Comparable experimental results using saturated acetylene transitions in gas cells include those by Balling et al, where the optical frequency of a high-power DFB laser is stabilised to a value of ≈ 10 kHz using third-harmonic techniques [14, 15], as well as Nakagawa et al who managed to stabilise a high-power DFB narrow linewidth laser diode with an absolute frequency accuracy of ≈ 20 kHz [16]. However, these experiments required more complex schemes and the stabilised laser was split at some experimental stage. In the case of Balling et al construction of several gas cells and splitting of the pump beam for modulation and generation of third harmonics was required. The experimental scheme used by Nakagawa et al requires additional Radio Frequency (RF) components, an EDFA amplifier and Electro- and Acusto-Optical Modulators (EOM, AOM). As opposed to these cases, our results report a remarkable improvement for the frequency stability of the stabilised laser using a simple experimental scheme.

4.5. CONCLUSIONS

A novel technique for modulation-free laser frequency stabilization based on saturation effects of gas absorption transitions and WMS techniques in HC-PBF's was demonstrated in this chapter. Application of such a detection technique to a pump-probe saturation scheme has been successfully implemented in the first part, characterizing the main saturation parameters of Acetylene absorbing transitions yielding a saturation level of about 2% and 50 MHz linewidth for fibre input powers of approximately 40 mW. In the second part a novel laser stabilization technique has been proposed and demonstrated for a high-power DFB laser diode, where the

stabilised laser beam is neither modulated nor split at any experimental stage in contrast to other available techniques. Stabilization of the emission frequency of the laser is achieved to a RMS value of 180 kHz for both constant laser temperature and over a range of 0.05°C. This novel technique can be extended to different types of saturation media and lasers providing a very useful way of stabilizing the operating wavelength in saturation spectroscopy experiments. The significant stabilization attained could be further improved by optimizing parameters such as the gas pressure or fibre geometry, maintaining the simple set-up and achieving stabilization figures similar to other more complex schemes. Note that, on the other hand, a drawback of saturation-based locking techniques using HC-PBF's is the amount of optical power lost due to gas absorption along the fibre. This effectively reduces the total optical power available at the output of the stabilised laser, though the power requirements in frequency referencing experiments are normally fulfilled.

4.6. REFERENCES

1. W. Demtroder, *Laser Spectroscopy: Basic Concepts and Instrumentation, 2Ed* (Springer, 1996).

2. J. C. Knight, "Photonic crystal fibres," Nature **424**, 847-851 (2003).

3. P. S. J. Russell, "Photonic-Crystal Fibers," Lightwave Technology, Journal of **24**, 4729-4749 (2006).

4. J. B. Jensen, J. Riishede, J. Broengx, J. Laegsgaard, T. Tanggaard Larsen, T. Sorensen, K. Hougaard, E. Knudsen, S. B. Libori, and A. Bjarklev, "Photonic crystal fibers; fundamental properties and applications within sensors," in *Sensors, 2003. Proceedings of IEEE*(2003), pp. 269-278 Vol.261.

5. T. Ritari, H. Ludvigsen, and J. C. Petersen, "Photonic Bandgap Fibers in Gas Detection," Spectroscopy **20**, 30-34 (2005).

6. T. Ritari, J. Tuominen, H. Ludvigsen, J. Petersen, T. Sørensen, T. Hansen, and H. Simonsen, "Gas sensing using air-guiding photonic bandgap fibers," Opt. Express **12**, 4080-4087 (2004).

7. J. C. Petersen, and J. Hald, "Frequency and wavelength standards based on gas filled HC-PBF's," in *Lasers and Electro-Optics, 2008 and 2008 Conference on Quantum Electronics and Laser Science. CLEO/QELS 2008. Conference on*(2008), pp. 1-2.

8. J. Tuominen, T. Ritari, H. Ludvigsen, and J. C. Petersen, "Gas filled photonic bandgap fibers as wavelength references," Optics Communications **255**, 272-277 (2005).

9. J. M. Dudley, and J. R. Taylor, "Ten years of nonlinear optics in photonic crystal fibre," Nat Photon **3**, 85-90 (2009).

10. M. d. Labachelerie, K. Nakagawa, Y. Awaji, and M. Ohtsu, "High-frequency-stability laser at 1.5 μm using Doppler-free molecular lines," Opt. Lett. **20**, 572-574 (1995).

11. A. Onae, K. Okumura, J. Yoda, K. Nakagawa, A. Yamaguchi, M. Kourogi, K. Imai, and B. Widiyatomoko, "Toward an accurate frequency standard at 1.5 μm based on the acetylene overtone band transition," Instrumentation and Measurement, IEEE Transactions on **48**, 563-566 (1999).

12. J. E. Debs, N. P. Robins, A. Lance, M. B. Kruger, and J. D. Close, "Piezo-locking a diode laser with saturated absorption spectroscopy," Appl. Opt. **47**, 5163-5166 (2008).

13. C. I. Sukenik, H. C. Busch, and M. Shiddiq, "Modulation-free laser frequency stabilization and detuning," Optics Communications **203**, 133-137 (2002).

14. P. Balling, M. Fischer, P. Kubina, and R. Holzwarth, "Absolute frequency measurement of wavelength standard at 1542nm: acetylene stabilised DFB laser," Opt. Express **13**, 9196-9201 (2005).

15. P. Balling, and P. Křen, "Development of wavelength standard at 1542 nm: acetylene stabilised DFB laser," in *WDS'05 Proceedings of Contributed Papers: Part III - Physics*, J. Šafránková, ed. (Matfyz press, Charles University, Prague, 2005), pp. 590-594.

16. K. Nakagawa, Y. Sato, M. Musha, and K. Ueda, "Modulation-free acetylene-stabilised lasers at 1542 nm using modulation transfer spectroscopy," Applied Physics B (Lasers and Optics) **B80**, 479-482 (2005).

17. M. J. Andrew, K. Kevin, L. JinKang, T. Rajesh, T. Karl, C. Francois, S. L. Philip, B. Fetah, R. W. Brian, and L. C. Kristan, "Stability of Optical Frequency References Based on Acetylene-Filled Kagome-Structured Hollow Core Fiber," in *Frontiers in Optics*(Optical Society of America, 2008), p. FWF7.

18. K. Knabe, A. Jones, K. L. Corwin, F. Couny, P. S. Light, and F. Benabid, "Saturated absorption spectroscopy of C2H2 inside a hollow, large-core kagome photonic crystal fiber," (Institute of Electrical and Electronics Engineers Inc., San Jose, CA, United states, 2008).

19. J. M. Supplee, E. A. Whittaker, and W. Lenth, "Theoretical description of frequency modulation and wavelength modulation spectroscopy," Appl. Opt. **33**, 6294-6302 (1994).

20. D. R. Paschotta, "Encyclopedia of Laser Physics and Technology - effective refractive index," (RP Photonics Consulting GmbH, 2004), http://www.rp-photonics.com/effective_refractive_index.html2009.

21. D. R. Paschotta, "The Photonics Spotligh - Effective Refractive Index: Correcting a Common Belief," (RP Photonics Consulting GmbH, 2007), http://www.rp-photonics.com/spotlight_2007_10_07.html2009.

22. R. Laroy, "New concepts of wavelength tunable laser diodes for future telecom networks," in *Vakgroep Informatietechnologie (INTEC), Faculteit Ingenieurswetenschappen*(Universiteit Gent, Gent, Belgium, 2006).

CHAPTER 5

LASER LINEWIDTH ANALYSIS AND SPHERICAL MICROCAVITIES

5.1. INTRODUCTION

Over the previous two chapters of this thesis experimental work has been presented regarding spectroscopic studies of acetylene hosted in a Hollow-Core Photonic Bandgap Fibre (HC-PBF, [1, 2]), with special emphasis in Laser Diode (LD) frequency stability applications. Absorption properties of this gaseous species have been investigated under linear and nonlinear absorption regimes, taking advantage of some of the optical properties of the microstructured fibre to enhance the molecular interactions with light. The main parameters of both linear and nonlinear absorption transitions have been successfully characterized, and some of the experimental results under the nonlinear regime have lead to the proposal and demonstration of a novel laser frequency stabilisation technique. These results are an example of how some novel photonic microstructures, in conjunction with LD's available from the telecommunications industry, can be effectively utilised to design and implement new schemes with very useful applications in both gas sensing research and accurate laser stabilisation.

During the present chapter, attention will be directed towards a second type of optical microstructure, namely *optical microspheres* or *micro-resonators* [3]. Yet these microspheres are geometrically very simple and they can be easily fabricated by just melting the tip of a silica optical fibre, they exhibit some complex but very interesting properties. Under appropriate conditions, light coupled into microspheres gives rise to the so-called *Whispering Gallery Modes* (WGM's) [3], a special type of light guidance mode based on total internal reflection in which light travels around the equator of the sphere with almost negligible losses. When **high** surface quality microspheres are utilised the excited WGM's can exhibit extremely narrow linewidths (of the order of tens of MHz), which is the key feature for our purposes: the spectral intensity profile of such microsphere modes becomes *extremely* sensitive to frequency noise perturbations, including those originated in the laser source. Thus, this opens up the possibility of investigating the linewidth characteristics of our NIR laser diodes using this type of microspherical structures. An appropriate theoretical description of the main concepts and relations relevant to such an investigation is first included in this chapter, followed by the corresponding presentation and discussion of the experimental results obtained in our case.

5.2. BACKGROUND

5.2.1. LASER LINEWIDTH AND LASER FREQUENCY STABILITY

In an ideal laser the optical output is purely monochromatic, with a phase coherent light beam of optical frequency $\upsilon(t)$ emitted. In the case of tuneable laser sources

several mechanisms exist to tune such optical frequency across some spectral interval, which can be as large as tens of nanometres in laser structures such as the SG-DBR or DFB laser diodes described in section 2.2.5 in chapter 2. As discussed in section 4.2.1 in chapter 4, the most extended methods to tune the emission frequency of laser diodes are based in controlling the laser temperature and injection current. Temperature variations of the laser cavity give rise to changes in its length L due to thermal expansion, ultimately affecting the emission frequency according to the phase condition for the wavelength of the M^h order mode [4]

$$\lambda_M = 2n'_{eff}L/M \tag{5.1}$$

On the other hand current injected into the laser changes the effective refractive index n'_{eff} of the laser cavity due to bandgap effects [4], as well as contributing to heating of the active region which again affects the cavity length. As discussed in section 4.2.1 in chapter 4 the bandgap effects can be neglected during our experimental work, so that the stability of an *ideal* laser source operated using *realistic* temperature and current controllers is determined by the low-frequency 1/f noise associated with such controllers.

However, in a real laser source the spectral output from the active region is not purely monochromatic but exhibits some frequency spread. At each time t the instantaneous frequency $\upsilon(t)$ of the laser beam differs from the ideal value $\upsilon_0(t)$ by some finite amount $\delta\upsilon(t)$. Such difference eventually determines the particular amplitude profile of the output power spectrum of the laser, which can be thus described by a specific lineshape and ***laser linewidth*** $\Delta\upsilon_{LAS}$. Calculations for the specific shape of the power spectrum associated with a particular type of laser source require a detailed analysis of

all the physical mechanisms affecting the *frequency departure* value $\delta v(t)$. A brief summary of the analysis carried out by Henry in [5] regarding semiconductor lasers will be thus presented here, emphasizing the most important results relevant to our work.

The power spectrum of a laser source emitting at an optical frequency $v(t)$ and corresponding angular frequency $\omega(t)=2\pi v(t)$ is directly proportional to the power spectral density of the laser $W_\beta(\omega)$ given by

$$W_\beta(\omega) = \int_{-\infty}^{\infty} \langle \beta(t) * \beta(0) \rangle \exp(i\omega t)\, dt \tag{5.2}$$

where $\beta(t)$ gives the time dependence of the optical field of the laser $E(x,t)$ according to

$$E(x,t) = B[\beta(t)\Phi(x) + \beta(t)^* \Phi(x)^*] \tag{5.3}$$

and B is a constant. The linewidth of the laser Δv_{LAS} is obtained by measuring the power spectrum of the laser, and the results for the spectral profile in the two most important operational regimes are presented next.

I) <u>*Operation below threshold*</u>

When the laser is operated below threshold, both intensity noise and phase noise contribute to the final linewidth of the laser. The power spectral density exhibits a Lorentzian lineshape given by

$$W_\beta(\omega) = \frac{R}{[\omega_0 + \alpha \Delta G/2 - \omega]^2 + (\Delta G/2)^2} \tag{5.4}$$

where $\alpha = \Delta n'/\Delta n''$ is the ratio of the changes in the real and imaginary parts of the refractive index of the laser cavity with change in carrier number, and $G = R - A$ is the difference between the rates of emission and absorption. The laser linewidth is given by

$$\Delta v_{LAS}^{I} = \frac{-\Delta G}{2\pi} = \frac{R}{2\pi I} \tag{5.5}$$

where $I = |\beta(t)|^2$ is the light intensity. When I is related to optical power we obtain the well-known result first reported by Schawlow and Townes [6].

II) *Operation above threshold*

The intensity fluctuations become stabilised when operating above threshold and can be neglected (this assumption indeed holds for laser diodes operating in this regime), and the main contribution to the laser linewidth arises from phase noise. Phase fluctuations arise as a result of spontaneous emission processes which can be shown to follow a Gaussian distribution, and calculations show that the power spectrum of the laser follows again a Lorentzian lineshape with a modified linewidth of

$$\Delta v_{LAS}^{II} = \frac{R}{4\pi I}(1 + \alpha^2) \tag{5.6}$$

This result differs from that in (5.5) by a factor ½, which accounts for the suppression of intensity fluctuations, and a factor $(1 + \alpha^2)$ which is related to the increased phase changes brought on by that suppression.

Thus, the laser diodes utilised above threshold during our experimental work exhibit a Lorentzian power spectrum. This laser *linewidth* discussion complements the laser *stability* description included in section 4.2.1 in chapter 4 and briefly summarized at the beginning of the current section. It is very important to clearly understand that both of these descriptions refer to physical processes of different nature and sources: The laser *linewidth* $\Delta\upsilon_{LAS}$ is a result of spontaneous emission processes taking place within the laser cavity itself and affects the laser emission frequency at all times. The laser *stability* is mainly a result of 1/f electronic noise in the temperature and current controllers external to the laser, and makes the whole Lorentzian distribution of linewidth $\Delta\upsilon_{LAS}$ to drift in time. The aim of this chapter is to ultimately determine the value for the laser linewidth utilising a novel scheme, minimising the 1/f noise to achieve it. Further references for the relationship between the lineshape of the laser power spectrum and the frequency noise can be found in Stephan et al. [7], while a more comprehensive study of the topic of laser diode modulation and noise has been published by Petermann [8]. An introductory book on the general topic of *Noise* has been published by Connor [9], very useful to clearly understand the basic ideas and fundamental theory of this field.

5.2.2. NARROW LINEWIDTH SLOTTED LASERS

Part of the experimental work presented in this chapter was carried out utilising a special type of laser diode, different than the SG-DBR and DFB laser structures

discussed in previous chapters. The new laser diode is referred to as a *Discrete Mode* (DM) laser diode, with the most important difference relevant to our experimental purposes as compared to the former laser sources being a very narrow emission linewidth. Results for the linewidth measurement $\Delta\upsilon_{DM}$ of the particular DM laser diode utilised during our experimental work are presented in section 5.4.1, while a brief overview of the laser structure and working principles is included here.

The DM laser is essentially a Fabry-Perot (FP) laser cavity where a fundamental difference is introduced: Some slots are etched along the ridge waveguide cavity at specific positions, as illustrated in figure 5-1. The aim of such etched slots is to effectively introduce perturbations in the refractive index of the laser structure. These slots manipulate the FP cavity mirror loss spectrum, and their specific positions along the waveguide determine which of the available FP cavity modes is enhanced over all others. Carefully designing the distribution of the etched features, as well as their depth, thus permits the design of a DM laser diode with a single mode operating wavelength at some desired value. The essential improvement of this type of cavities as compared with other structures is that the ridge and slots can be etched in the laser structure during **the same** processing stage. Epitaxial re-growth stages used in other laser fabrication techniques are avoided, simplifying the experimental process. In the particular DM laser utilised in our case, this relaxation of the fabrication requirements allows for the choice of materials which eventually help enhancing the laser output linewidth. The structure of our DM laser is based in AlGaInAs quantum wells.

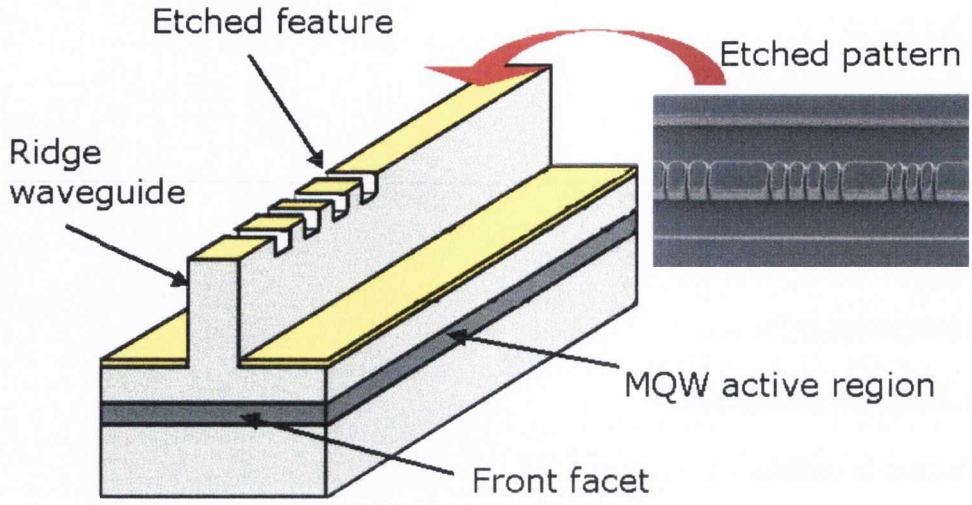

***Figure 5-1**: Schematic view of an AlInGaAs/InP Multi Quantum Well DM laser diode, along with an example for a SEM image of a particular etched feature pattern (inset). The etched slots can be grown during the same etching stage as the ridge waveguide, and their position ultimately determines the emission wavelength of the DM laser (reprinted from [13] with permission).*

Our DM laser is designed to emit at a wavelength of $\lambda \approx 1537$ nm at a temperature of T = 25 °C and current of I = 150 mA, and can be tuned by temperature or injection current effects as described in the previous section 5.2.1. An example of the optical spectrum recorded under such conditions for the DM laser is shown in figure 5-2, where the characteristic single mode emission pattern can be clearly observed.

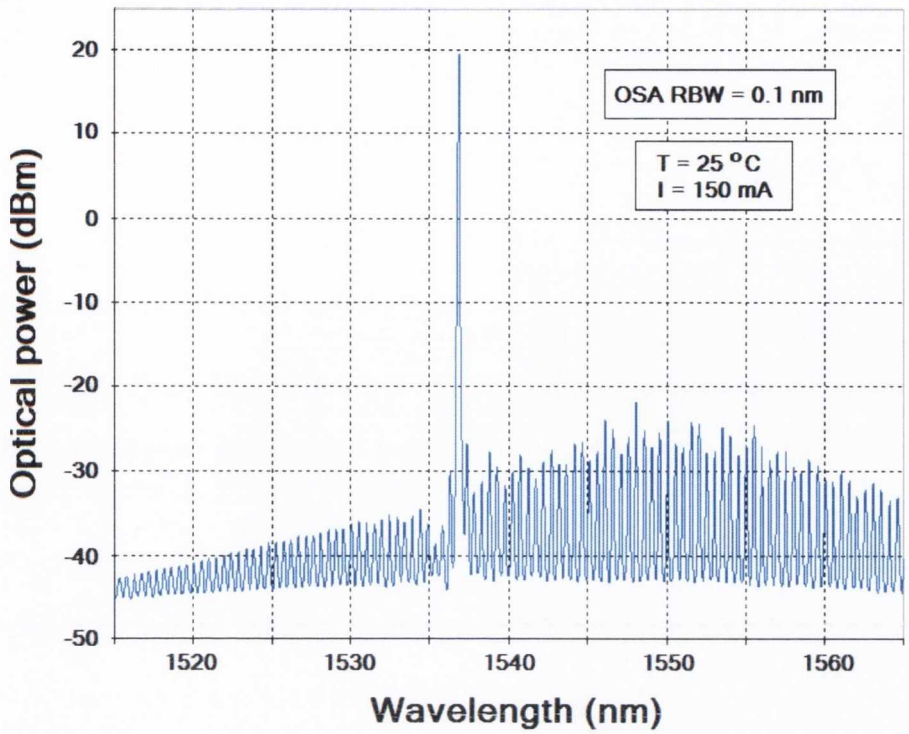

***Figure 5-2**: Optical spectrum for the DM laser diode utilised during our experimental work, measured at a laser temperature and injection current values of T = 25 °C and I = 150 mA respectively. The laser clearly emits in a single mode fashion, with the emission wavelength centred around $\lambda \approx 1537$ nm (measurement carried out by Eblana Photonics, printed with permission).*

The narrow linewidth characteristics of this laser are a key feature for the experimental work presented in upcoming sections. Further details about the fabrication process and general properties of DM lasers, along with the linewidth and tuning characterization of similar lasers as the one used in our case, can be found in [10-13].

5.2.3. LASER LINEWIDTH MEASUREMENT TECHNIQUES

As described in section 5.2.1, measurement of the linewidth of a laser source is usually achieved by recording the optical power spectrum utilising some appropriate experimental scheme. Acquired data can be then fit to a suitable lineshape curve, which in the case of laser diodes operating above the threshold correspond to a Lorentzian profile. Several schemes exist to achieve this goal, but attention will be directed here towards two of the most commonly used methods in order to understand their working principles.

Self-Homodyne Technique

The set-up corresponding to this technique is schematically presented in figure 5-3. In this scheme the fiberised output of a laser source with a linewidth $\Delta\upsilon_{IN}$ and operating optical frequency υ_0 is connected to a fibre interferometer with two arms of different path lengths.

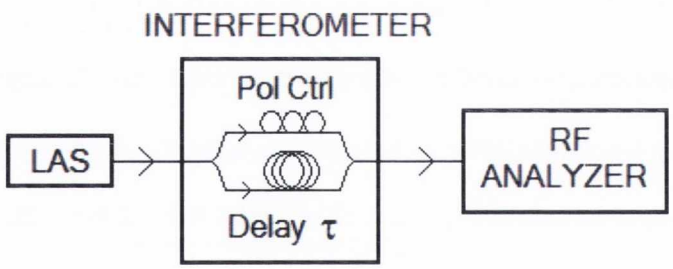

Figure 5-3 *Schematic set-up for self-homodyne laser linewidth measurements.*

The same optical power is directed along each of the arms, and the difference in path lengths gives rise to a constant time delay τ between the two beams before they recombine at the interferometer output. An integrated polarisation controller can be manually adjusted in order to optimize the relative polarisation of the beams and

provide optimum output intensity. Essentially, the effect of the time delay is to effectively remove any correlation between the two laser beams that would otherwise remain in phase since they are derived from the same laser source. If the path length difference between the interferometer arms is chosen so that the related time delay τ exceeds the coherence time of the laser $\Delta\tau_C$ ($\tau > \Delta\tau_C$), then the two beams can be effectively regarded as coming from two independent laser sources with the same characteristics when they are mixed together again. The output of the fibre interferometer is then sent to a Radio Frequency (RF) analyser in order to acquire the corresponding optical power spectrum of linewidth $\Delta\upsilon_{OUT}$. The lineshape of this spectral power profile will be proportional to the convolution of the power spectrum of the two beams, i.e. of two exactly equal replicas of the original spectrum of the laser source. It can be demonstrated that the convolution of two Lorentzian lineshapes yields a Lorentzian profile whose linewidth equals the sum of those of the original lineshapes [14], so in the case of our laser diodes it follows that

$$\Delta\upsilon_{OUT} = 2\Delta\upsilon_{IN} \tag{5.7}$$

Where the input linewidth equals that of the laser, $\Delta\upsilon_{IN} = \Delta\upsilon_{LAS}$. This allows us for extraction of the linewidth of the utilised laser source from the acquired data by using the simple relation

$$\Delta\upsilon_{LAS} = \Delta\upsilon_{OUT}/2 \tag{5.8}$$

It should be noted that the experimental spectrum obtained with an RF analyser shows only half of the profile, because this measurement technique only considers the absolute value of the frequency deviation from the carrier. The near-DC component of

the spectrum is not either observable up to a *cut-off frequency* f_{CUT} determined by the interferometer: according to the previous discussion, any beam components undergoing an effective delay smaller than τ will be still correlated and thus become *invisible* by the RF analyser, thus yielding a value for the equivalent cut-off frequency of $f_{CUT} = 1/\tau$. Results for the self-homodyne linewidth measurements for the lasers used during the experimental work are presented in section 5.4.1, using a fibre interferometer with a delay of $\tau = 25$ μs, $f_{CUT} \approx 40$ kHz. The special case where a short delay comparable to the laser coherence time is used has been analysed in detail by Ludvigsen et al. in [15].

Heterodyne technique

The second linewidth measurement technique to be discussed is essentially based on the same working principle as the self-homodyne case presented above. As sketched in figure 5-4 the main difference between both techniques is that, in the heterodyne case, the outputs from **two** different laser sources are combined and then sent directly to an RF analyser

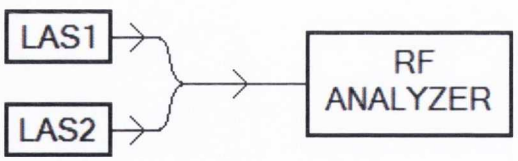

***Figure 5-4**: Schematic set-up for heterodyne linewidth measurements, where two lasers are used (LAS1 and LAS2).*

A reference laser with a known *narrow* linewidth $\Delta\upsilon_{REF}$ is usually chosen and mixed with the target laser source whose linewidth $\Delta\upsilon_{IN} >> \Delta\upsilon_{REF}$ is to be determined. The target laser operates at a frequency υ_0 while the reference source emits at a close

frequency $\upsilon_0+\Delta\upsilon$ ($\Delta\upsilon<<\upsilon_0$). Interference of these closely-spaced optical frequency sources yields an output spectrum consisting of a carrier frequency peak centred at υ_0 surrounded by intensity peaks symmetrically located at values $\upsilon_0 \pm \Delta\upsilon$. According to the discussion in the self-homodyne case, when laser diode sources exhibiting a Lorentzian power spectrum are utilised the linewidth of both the carrier and side peaks is given by

$$\Delta\upsilon_{OUT} = \Delta\upsilon_{REF} + \Delta\upsilon_{IN} \approx \Delta\upsilon_{IN} \tag{5.9}$$

where the condition $\Delta\upsilon_{REF} << \Delta\upsilon_{IN}$ has been taken into account. Some important conclusions can be drawn from relation (5.9): *The linewidth of the acquired power spectrum directly corresponds to the linewidth of the targeted laser source.* In addition, there is a fundamental difference in this measurement technique as compared with the self-homodyne scheme. We can acquire the power spectrum of the side peak centred at the beat frequency $\Delta\upsilon$, with two immediate consequences:

1. This spectrum is now double-sided, somewhat facilitating the corresponding theoretical fit.
2. The spectrum is recorded at higher frequencies, thus eliminating part of the 1/f noise associated with the laser sources (the beat frequency $\Delta\upsilon$ is usually chosen to lie in the 1 GHz region).

The total accuracy attainable when implementing the heterodyne measurement technique is on the other hand limited by various factors. First, the linewidth of the reference laser $\Delta\upsilon_{REF}$ must be known itself with a high accuracy. Second, and more important, the stability of the beat frequency $\Delta\upsilon$ is limited by the 1/f noise affecting

both of the laser sources. The value for the beat frequency corresponds to the difference between the emission frequencies of the two lasers, so any drift of these values automatically shifts the central frequency for the side peak. This can severely limit the attainable measurement accuracy, so good quality, narrow linewidth External Cavity Lasers (ECLs) are commonly chosen as the reference to minimise the effect.

A special case of this heterodyne scheme is illustrated in figure 5-5 below and can be referred as the ***self-heterodyne*** technique.

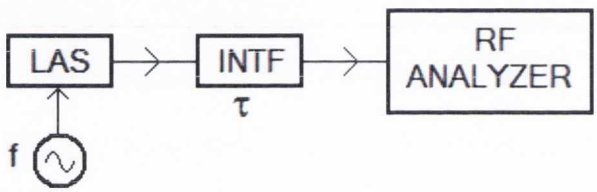

***Figure 5-5**: Schematic set-up for self-heterodyne linewidth measurements.*

In this case a single laser source of linewidth $\Delta\upsilon_{IN}$ and operating frequency υ_0 is used. The laser frequency is modulated using a sinusoidal wave at a frequency f in the 1 GHz regime, giving rise to the appearance of multiple spectral sidebands of order n separated from the carrier frequency υ_0 by an amount nf [16]. These sidebands are exact replicas of the carried frequency peak and exhibit the same linewidth, while the modulation depth can be chosen so that only the first sideband is produced. In such a case both the carrier peak and the first sideband enter the fibre interferometer and become uncorrelated before being recombined, so that they can be effectively regarded as coming from two independent laser sources with the same linewidth $\Delta\upsilon_{IN}$. The same analysis as in the heterodyne case applies so that the recorded spectrum on the RF analyzer presents both a one-sided Lorentzian peak centered at zero frequency

plus a sideband peak centered at the modulating frequency f, both of them with an approximate linewidth of

$$\Delta\upsilon_{OUT} = \Delta\upsilon_{IN} + \Delta\upsilon_{IN} = 2\Delta\upsilon_{IN} \tag{5.10}$$

Thus, the sideband spectrum can be then recorded and fitted to a Lorentzian lineshape to estimate the target laser linewidth $\Delta\upsilon_{LAS} = \Delta\upsilon_{IN}$ according to the relation

$$\Delta\upsilon_{LAS} = \Delta\upsilon_{OUT}/2 \tag{5.11}$$

Note that these measurement techniques usually require the use of fast photodiodes, with suitable response characteristics in the high-frequency region targeted in each case. A rigorous theoretical analysis of both optical heterodyne and homodyne measurement techniques by Nazarathy et al. can be found in [17] for further references.

5.2.4. OPTICAL MICROSHPERES AND WGM MODES

The experimental work presented in this chapter is based on a special type of optical microcavities, namely *optical microspheres* or microresonators. In a similar fashion as other types of optical resonators, the main interest of these microstructures relies on the fact that light can be confined within a small volume with almost negligible losses for long periods of time. A particular case is that where such excited *modes* are confined close to the surface of the microspheres with minimum losses, and are referred to as ***Whispering Gallery Modes*** **(WGM's)**. The interesting properties of these modes can be applied to many different fields, among which we can locate our

experimental purpose of investigating linewidth properties of laser sources. Thus, it becomes necessary to understand the main features and properties of this type of microstructures and modes relevant to our research before presenting and discussing further experimental schemes and results. Much theoretical work has been done to characterize the structure and main properties of optical microspheres, as well as a large amount of experimental work to control, modify and exploit such properties to improve existing applications or establish new ones. Thus, a brief summary of the review presented by Chiasera et al. [3] will be included in this section, referring to further material when needed.

Structure and fabrication

Spherical microspheres are micron-size spherical structures with a diameter of typically ten to a hundred micrometers. The most extended type of microspheres are made from silica glass, though some experiments have been carried out with liquid microdroplets [18-20]. Glass microspheres can be fabricated using melting processes by simply targeting the end tip of a silica fibre (this corresponds to our case, described in detail in section 5.3.1), while some other methods are based in sol-gel processing [21]. In some cases specific coatings are applied, and some degree of ellipticity may apply (which in practice does not affect our results). Our experimental procedure to fabricate microspheres allowed us to routinely achieve reproducible results.

Light coupling

Light coupling into microspheres is commonly achieved using evanescent-field schemes. Some optical structures are used that exhibit an evanescent field decaying into the air at some position over their geometry, and the microresonators then

carefully located within overlap distance with that field (of the order of hundreds of nanometres). When the coupling conditions are fulfilled (usually related to phase matching across the microsphere surface), light is coupled into the microcavity. Examples of the most extended evanescent-field coupling schemes are shown in figure 5-6, including tapered fibres (a), waveguides (b), optical prisms (c) or angle polished fibres (d).

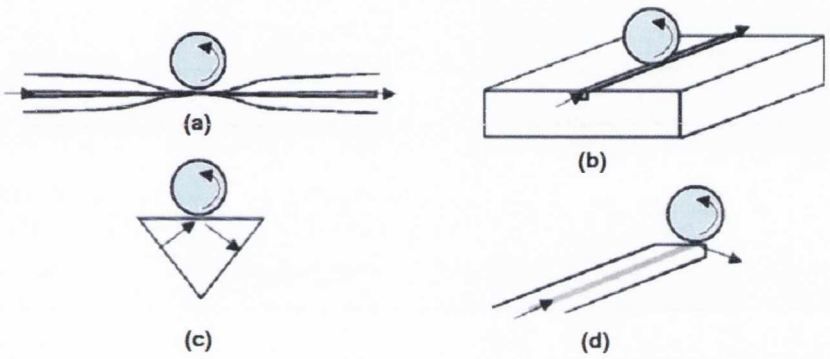

***Figure 5-6**: Schematic illustration of the most extended microsphere light coupling geometries. The evanescent field from a tapered fibre (a), waveguide (b), optical prism (c) or angle-polished fibre (d) is coupled into the microsphere when the phase matching condition is fulfilled (adapted from [3]).*

During our experimental work an optical prism scheme was utilised, allowing for fine control of the coupling geometry. Further details for the set-up are included in section 5.3.1, while optimization of coupling into microspheres is further discussed in [22].

Total internal reflection and WGM's

If light of wavelength λ is coupled into a microsphere of radius a and refractive index n under the appropriate conditions, a special guidance mechanism takes place. In a so-called *Whispering Gallery Mode (WGM)*, light is guided along the equator of the

microsphere due to Total Internal Reflection (TIR). Light travels very close to the microsphere surface with a small fraction evanescently decaying into the surrounding medium (usually air). In terms of the *size parameter x*, the coupling condition can be expressed as

$$x \equiv 2\pi a/\lambda = l/n \tag{5.12}$$

where l is an integer. Different modes can be excited exhibiting a different radial and angular field distribution depending on both the polarization of the incoming field and coupling geometry. Some quantum numbers r –radial- and l, m –angular- are used to describe the field distribution (using r rather than the usual notation n for the radial quantum number to avoid misunderstandings with the refractive index). This leads to the concept of *mode bands*, corresponding to groups of WGM's of similar characteristics. A pseudo-free spectral range (FSR) can be defined to describe the constant separation between modes with the same polarization and radial number r but differing in one unit of l (assuming no ellipticity),

$$FSR_l \equiv \Delta\upsilon_{r,l}^{\Delta l} \approx \frac{c}{2\pi na} \tag{5.13}$$

In the case of two adjacent modes with same numbers r, l but different polarizations Transverse-Electric (TE) and Transverse-Magnetic (TM),

$$FSR_{pol} \equiv \Delta\upsilon_{r,l}^{TE,TM} \approx \frac{c}{2\pi na}\frac{\sqrt{n^2-1}}{n} \tag{5.14}$$

Examples of experimental traces of excited WGM bands during our experimental work are included in figures 5-13 and 5-14 in section 5.4.2. Observing the structure of

the complete band is very important for our purposes, as it allows us to select the strongest WGM to be targeted and improve the achieved SNR. It is also important to note that, in practice, all the modes belonging to the same band observed during our experimental work exhibited the same width within experimental error, relaxing the conditions when selecting a particular mode.

Q factor

The so-called *Q-factor* is a measurement of the *quality* of the microsphere in terms of its associated optical losses. The Q-factor is defined by the ratio of the optical frequency υ of the guided light and the resonance width of the excited WGM $\delta\upsilon$,

$$Q = \frac{\upsilon}{\delta\upsilon} \tag{5.15}$$

The value for the *intrinsic* Q_0 factor for an isolated microsphere is a combination of radiative (curvature), bulk (material) and surface losses. Our measured high-Q values are of the order of $Q \approx 10^7$, as detailed in section 5.3.1. It is critical for our linewidth investigation purposes that high quality microspheres are routinely fabricated.

Thermal effects

When light is coupled into a WGM thermal effects must be taken into account (unless the light level is extremely low). As light travels around the equator absorption of light by the Silica microsphere occurs and the absorbed power builds up inside the cavity, increasing the sphere temperature proportionally to its thermal capacity and the amount of optical power coupled in. This induces thermal expansion of the microcavity increasing the original diameter, which effectively changes the resonant

condition (5.12) for the incoming field, affecting coupling of the light into the system. This effect takes place on a time scale corresponding to the thermal response of the microspheres and can become very significant depending on the experimental conditions. Details on the origin and minimisation of thermal effects during our experimental work are included in section 5.3.2. Note that thermal effects also apply when the temperature of the microsphere decreases and the diameter is reduced. A detailed analysis on the effects of both size and refractive index changes in the resonant frequency of a microsphere has been published by Schweiger et al. in [23] for further reference.

On the top of the previous points, the resonant frequency of WGM's can be tuned based on mechanical- or thermal-induced deformation of the sphere size. An example of mechanical-based tuning can be found in [24], though during our experimental research no tuning of the resonant frequency was either implemented or desired.

5.3. EXPERIMENTAL SET-UP

5.3.1. SPHERICAL MICROCAVITIES FABRICATION

Fabrication of the spherical microcavities used in the experiment was carried out in a systematic and reproducible fashion, following a series of well defined steps in order to provide good quality micro-resonators. This allows for data consistency during experimental research, a condition which must be fulfilled in order to carry out analysis and extract meaningful conclusions. The fabrication process is based on the principle of fibre melting and sphere formation due to surface tension forces. When a solid material is melted under standard laboratory conditions, two main forces act on the liquid phase material during the process: gravity and surface tension. On one hand,

in order to minimise the total surface energy associated with the system and thus fulfil the stability condition, the melted material acquires a spherical shape corresponding to minimum surface area for a given volume V. On the other hand the gravity acts on the melted volume pulling it down, the additional force distorting the ideally spherical surface. The final microsphere shape is determined by both effects, generally giving rise to an almost perfectly spherical shape because the surface tension forces on this scale are orders of magnitude greater than the force due to gravity.

The experimental set-up corresponding to the melting technique implemented is presented in figure 5-7. In the first step a piece of a single mode (SM) Silica fibre is immersed in Acetone for approximately 20 minutes in order to soften the outer protective coating layer (≈250 μm) and then strip it. This leaves the fibre cladding (≈125 μm) exposed and minimises the amount of impurities that might be present due to the plastic coating, which would otherwise eventually limit the attainable Q-factor for the microresonator. Then the fibre is attached to a two-directional positional stage which allows both vertical and horizontal (out of the plane corresponding to figure 5-7) translation. The fibre is held in a vertical position and a CO_2 laser is set with its output beam horizontally traversing the fibre a few centimetres from its bottom end. The laser emits at 10.6 μm with a maximum optical power of 20W and the beam is focused on the fibre with the help of a suitable lens. The output power of the laser is manually controlled and measured with a power meter placed after the beam waist. This allows for centring the fibre in the beam by operating at low optical powers and minimizing the meter reading while the position of the fibre is adjusted.

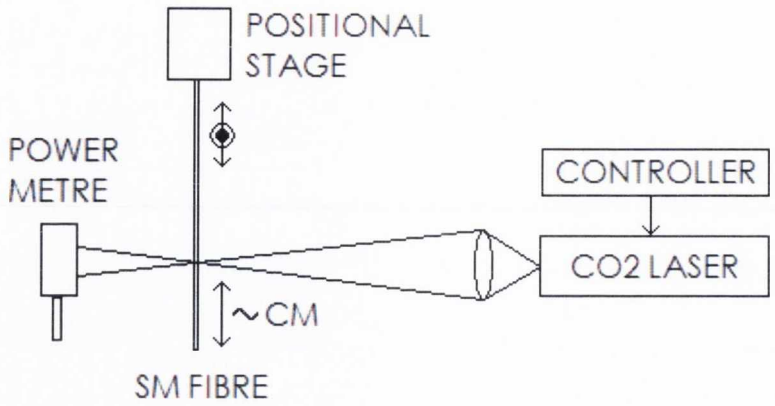

***Figure 5-7**: Experimental set-up for microsphere fabrication. A single-mode (SM) fibre is attached to a two-directional positional stage allowing for vertical and horizontal (out of the plane) position adjustment. The power-controlled output from a CO_2 laser is focused on the fibre and measured with a power metre.*

Once the fibre and laser are properly aligned the optical power of the laser is increased until the fibre approaches the melting point, as observed using a microscope. Then, as outlined in figure 5-8a, the fibre is manually pulled down from the bottom end using appropriate tweezers so that a narrow tapered section is created (tens of μm of diameter). The fibre position is then adjusted until the laser beam is focused on its bottom, untapered section. The optical power of the laser is then increased to start the melting process. As the microsphere is formed at the tip of the fibre, its vertical position is adjusted in real time so that the whole untapered section gets melted. The schematic diagram for this step corresponds to figure 5-8b. At this point the optical power of the laser is decreased avoiding melting effects, and the fibre position adjusted so that the beam is focused tens of millimetres from the microsphere. Then the optical power of the laser is increased again, giving rise to a bending of $\approx 90°$ of the fibre as sketched in figure 5-8c. This bending facilitates coupling of the light at the equatorial plane of the microsphere, minimizing

interference with the supporting fibre stem. A sample microsphere obtained with this process is included in the same figure, in very good agreement with the expected shape as described above.

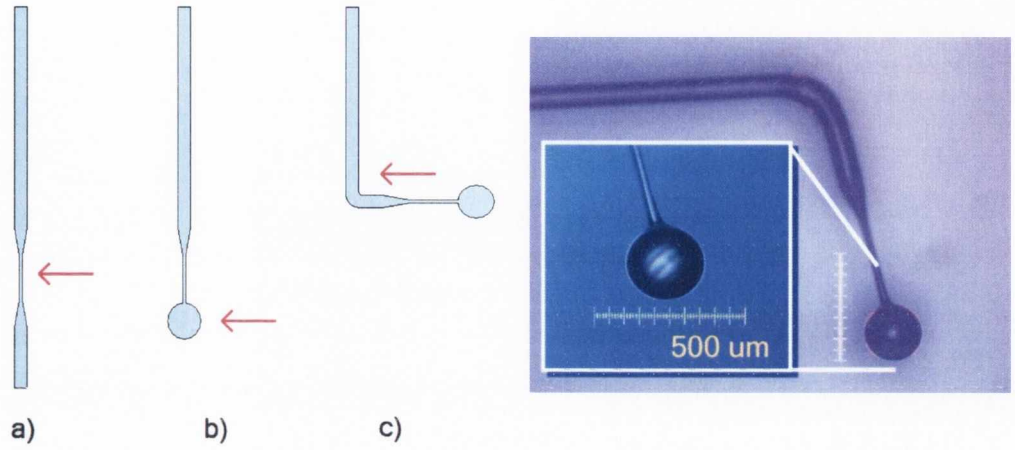

***Figure 5-8**: Schematic illustration for the microsphere fabrication process. (a) Fibre tapering. (b) Fibre melting and microsphere creation. (c) Fibre bend of ≈ 90 °C to facilitate experimental coupling. A microscope image of a sample microsphere created using this process is included, in very good agreement with the expected shape. The microsphere, of ≈ 250μm diameter, sits at the end of a tapered stem of a SM fibre with an original cladding diameter of ≈ 125 μm.*

5.3.2. WGM EXPERIMENTAL SCHEME

A schematic representation for the experimental set-up used to study the WGM properties in the spherical microresonators is shown in figure 5-9. A tuneable laser source is set so that the output wavelength can be tuned across the microsphere resonant value by ramping the driving current source with a voltage signal V_{MOD} at a frequency f_{MOD}. Two different laser sources will be used as described in upcoming sections, and the polarization adjusted in both cases using a suitable polarization controller.

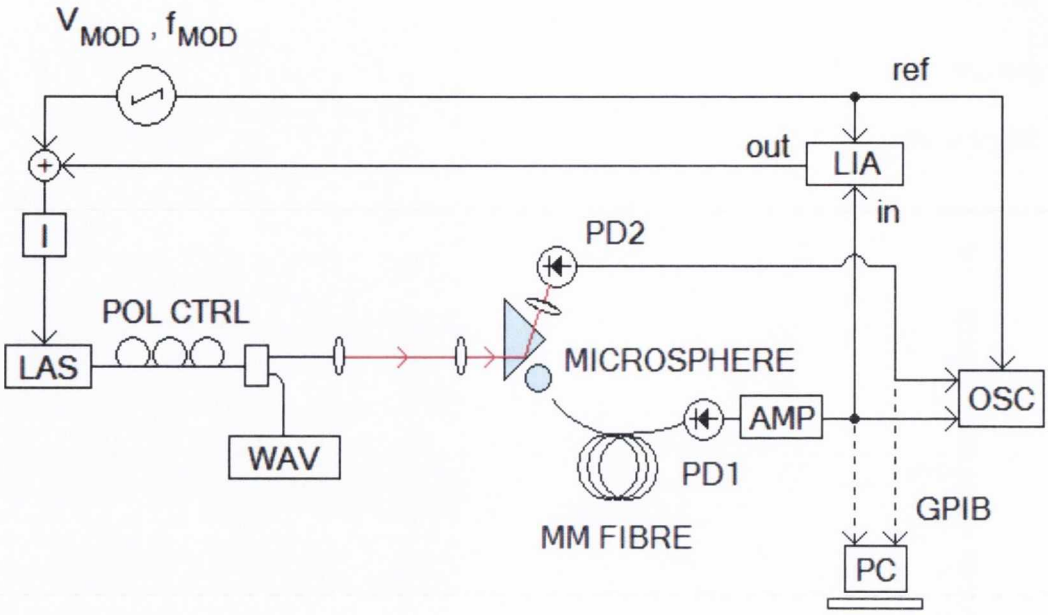

***Figure 5-9**: Scheme of the set-up implemented for the microspherical resonators WGM experimental work. Abbreviations used correspond to: polarization controller (POL CTRL), wavemeter (WAV), multimode fibre (MM FIBRE), photodetector (PD), optical amplifier (AMP), oscilloscope (OSC), Lock-In Amplifier (LIA), Personal Computer (PC).*

As explained in section 5.2.4 different WGM bands can be excited within the micro resonator depending on the polarization state of the coupled beam, so proper control of this parameter becomes crucial for optimum excitation of WGM's in the microsphere. Coupling depends on polarization of the input light via the continuity equations for the electromagnetic field across two media, though this effect was not observed in practice and thus neglected. Light is collimated and focused onto an optical prism using a lens system positioned on precision translation stages for coupling optimization. An additional piezo controller was also introduced in the set-up for fine tuning of the coupling distance. A fraction of the laser beam (typically 5-10%) can be split off and sent to a wavemeter if necessary. A detailed scheme of the prism coupling is shown in figure 5-10.

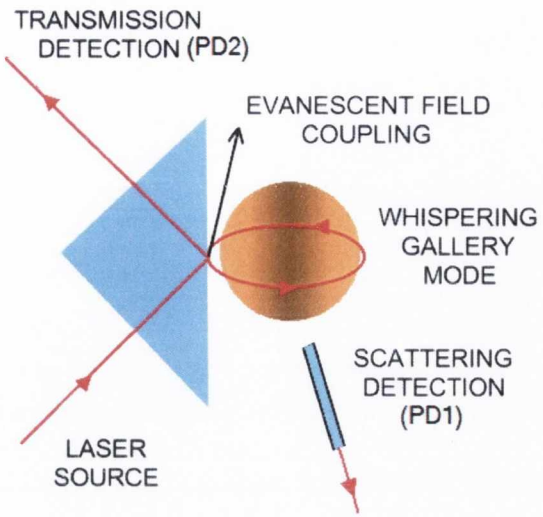

***Figure 5-10**: Detailed scheme for the evanescent field WGM prism coupling into the micro spherical resonator.*

The laser beam is focused onto one face of the prism so that part of the optical field evanescently decays into the surrounding air. The detection system consists of two independent photodetectors that record the transmitted light through the optical prism (PD2) and the scattered light from the spherical surface (PD1), the latter collected by a multimode fibre whose position can be precisely controlled. Because of the small amount of scatter detected, a low-noise transimpedance optical amplifier is introduced after the corresponding photodetector in order to improve the Signal-to-Noise Ratio (SNR) of the scattered signal (this amplifier works at gain and bandwidth values of $2x10^8$ V/A and 100 kHz respectively). Signal amplification relaxes the requirements for the total optical power coupled into the microsphere, somewhat making easier the challenging coupling process in prism-based coupling schemes. The bandwidth of the amplifier produces some effective averaging of the collected data but does not affect the results and subsequent discussion to be presented in section 5.4. The signals from

both photodetectors are then acquired using a high-frequency digital oscilloscope referenced to the modulation frequency f_{MOD}. Ramping the optical frequency υ of the laser in this way means that the scattered signal from the microsphere surface is directly proportional to the WGM intensity profile $I(\upsilon)$, while the signal collected after the prism corresponds to the associated $I_0 - I(\upsilon)$ *absorption* profile (note that light is not strictly *absorbed* by the microsphere, but only coupled in; I_0 corresponds to the intensity of the laser beam incident at the prism inner surface). This experimental scheme allows for the profile of one or several microsphere modes to be observed in real time on the oscilloscope, depending on the value for the modulation depth applied to the laser source. The WGM signal $I(\upsilon)$ is at the same time acquired by a Lock-In Amplifier (LIA) referenced to the modulation frequency f_{MOD}. The output of this lock-in is used to implement an active feedback loop in order to lock the laser emission frequency to the centre of the WGM, explained in more detail next.

WGM line centre locking loop

A very important feature of the set-up scheme presented in figure 5-9 is that of the active feedback loop implemented during experimental work. This loop is used to lock the operating frequency of the laser source to the central frequency of the excited mode that is being targeted. This has significant consequences which facilitate both collection and subsequent analysis of data, and will be discussed at the end of this section. The set-up for the locking loop essentially replicates those presented in sections 3.3.2 and 4.3.1 during chapters 3 and 4, working on the same principle. The loop is implemented by connecting the output of the lock-in described above to the input of the modulation facility integrated in the laser current control unit *I*. As detailed in section 2.2.6 of chapter 2, this modulation scheme ensures that the output

signal of the lock-in is proportional to the first derivative (1f) of the input signal. In the particular case described here, the 1f signal detected is thus proportional to the first derivative of the WGM scattering signal with respect to υ. Because the intensity profile of the microsphere mode follows a Lorentzian lineshape, the corresponding first derivative presents a zero-crossing at the WGM line centre. Hence, when the central wavelength of the modulated laser is set to the centre of the microsphere mode, the output of the lock-in equals zero. Summarizing the detailed explanation included in section 4.3.1 of chapter 4, we have for the lock-in output $y(t) = 1f(t)_{CENTRE}$. In the ideal case where the frequency of the laser does not drift in time from its set value we have $y_{IDEAL}(t) = 1f_{CENTRE} = 0$, and the reference value for the control loop can be defined to be $r(t) = y_{IDEAL}(t) = 0$. The error signal for the active feedback loop, defined as $e(t) = y(t) - r(t)$ in section 4.2.3, thus reads $e(t) = y(t) - 0 = y(t)$ and corresponds directly to the lock-in output. In the real case the optical frequency of the laser drifts in time due to temperature and current perturbations and a non-zero error signal $e(t) \neq 0$ is generated. The total voltage signal injected to the modulation facility of the current control unit of the laser thus corresponds to the modulation ramp voltage V_{MOD} plus a DC value equal to the error signal amplitude $e(t)$. The aim of the locking technique is to provide the conditions under which the frequency drift related to the laser is counteracted and effectively nullified by the loop contribution, as illustrated in figure 5-11 (this figure corresponds to figure 4-6 in chapter 4, as it essentially describes the same principle). The phase of the lock-in must be carefully chosen to fulfil such a condition or otherwise the loop will further perturb the laser frequency stability.

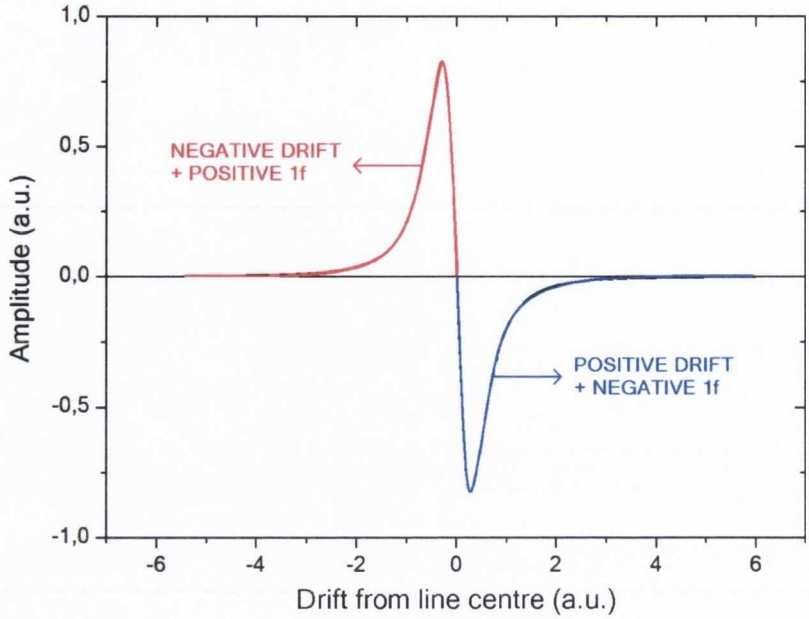

***Figure 5-11**: Schematic representation of the operational principle for the active feedback loop implemented in the WGM experiment. The 1f signal has the appropriate lineshape to counteract for the laser frequency drift. The figure corresponds to figure 4-6 in chapter 4, but has been included here because it essentially describes the same locking principle.*

At this point it is useful to distinguish between the two possible modulation regimes applied during our experimental work and describe the active feedback loop behaviour in each case.

A) Low modulation depth: Only one WGM is excited within the microsphere and the scattered signal is zero elsewhere across the modulation interval. This case is analogous to the modulation schemes implemented in sections 3.3.2 and 4.3.1, with the error signal almost equal to zero. The drift of the laser is compensated by the loop and the emission frequency is locked to the central frequency of the WGM mode. Experimental results presented in sections 5.4.1

and 5.4.2 were obtained under this regime, with the modulated interval of the order of few picometers.

B) High modulation depth: When the modulation depth is increased a wider wavelength interval is covered. If this interval exceeds the Free Spectral Range (FSR) value for the WGM's targeted in the experiment (FSR ≈ 10 pm in our case, high modulation depth interval of the order of hundreds of picometers), then more than one mode within the working band is excited. In this case several Lorentzian profiles of different intensities populate the scanning region and the output of the lock-in is not zero. The magnitude of this error signal is a result of the contribution of all modes, each of the error amplitudes directly proportional to the corresponding mode intensity. The net result is that the value for the error signal is mainly determined by the strongest mode within the band, and the locking loop thus shifts the operating frequency of the laser towards that specific mode centre. The emission frequency of the laser gets eventually locked to that value. In practice, we found this method to significantly facilitate the experimental preparation stage. A high modulation depth is initially applied to the laser, coupling distance and polarization of the laser optimized, and several modes are excited and observed in the oscilloscope. A certain mode within the band was routinely observed to be strongest, with additional weaker modes spread over the modulation interval. Then the locking loop was closed, and the locking effect automatically observed: the band of modes shifted in real time with the central frequency consecutively *jumping* from one mode to the nearest stronger one, until eventually being stabilised to the strongest mode previously observed. No

extra adjustment was needed once the locking loop was closed, and the emission frequency of the laser was effectively locked to the centre of the strongest mode. Two examples of the WGM band structure obtained when applying a high modulation depth to the laser are presented in figures 5-13 and 5-14 in section 5.4.2. After the laser frequency was locked to the strongest mode within the band the modulation depth was decreased, and the strong mode investigated under a low modulation depth regime.

WGM locking loop vs gas line locking loop

Successful implementation of the locking loop described above means that the emission frequency from the laser is locked to the targeted WGM centre. As mentioned during the previous discussion this locking method is in some ways similar to the gas-based locking techniques implemented in sections 3.3.2 and 4.3.1 presented in previous chapters. However, some fundamental differences apply that must be understood and will be clearly described now. The main difference is related to the resonant frequency for the corresponding gas absorption line or microsphere mode. In the gas-absorption-based locking techniques the resonant frequency of the absorption line is **fixed** at some specific value, which is determined by the corresponding molecular physics analysis of the targeted gas. On the other hand, in the whispering-gallery-mode-based locking technique the value of the resonant frequency for the mode arises from a geometrical requirement (the relationship between the wavelength of the incoming light and the radius of the microspherical resonator). Here lies the key point which determines the fundamental difference between both methods: the size of the microsphere can change during experimental work due to thermal effects, so the resonant value for the mode is **no longer fixed**. We can easily estimate the effect of a small change in the microsphere size on the resonant WGM wavelength by taking the

derivative of the coupling condition (5.12). Such calculation leads to a relation $d\lambda/\lambda = da/a$ for the relative variations of the microsphere radius a and the wavelength λ of the incoming light, which for our measured values of a $\approx$ 125 μm and $\lambda \approx 1.5$ μm yields $d\lambda \approx 6\ 10^{-3} da$. This means that a change of 1 μm in the radius would lead to a shift of the resonant wavelength of $\approx$ 6 nm, several orders of magnitude bigger than the typical width of a WGM in a high-Q microsphere (as an example, our measured sphere modes presented in section 5.4 have widths of the order of sub-picometres). Thus, these thermal effects can be thought as being low-frequency noise sources that ultimately limit the frequency stability of our system and need to be minimised. The different processes giving rise to thermal effects during our experimental work are analysed next, and can be split in two categories: *External* or *laser-related.*

- **EXTERNAL: INDEPENDENT OF THE LASER SOURCE.**

  - *Room temperature*: If the room temperature significantly changed during experimental work, the corresponding temperature of the microsphere would be affected and the coupling condition would change. The laboratory is kept at a constant temperature of T = 22 °C so these variations can be neglected.
  - *Coupling distance*: The coupling distance between the microsphere and prism determines the fraction of the evanescent field from the prism which overlaps with the resonator. When the coupling distance decreases a bigger percentage of the laser field is coupled into the microsphere, increasing the optical power within the microcavity and thus raising its temperature. The coupling distance was only changed during our experimental work prior to data acquisition once the laser frequency was locked to the centre of the targeted WGM. The locking loop maintained the laser frequency aligned to the WGM centre as the distance was

varied, allowing for optimization of the SNR of the WGM signal. The coupling distance can be regarded constant during data acquisition time.

- **LASER-RELATED: DEPENDENT ON THE LASER SOURCE.**

  - *Modulation depth*: When the modulation depth applied to the laser decreases from a high- to a low-modulation depth regime at a fixed modulation frequency, the laser light spends on average more time within the WGM coupling interval. Hence, the optical power coupled during scanning time increases and the temperature of the microcavity raises, changing its size and shifting the resonant frequency. The modulation depth is changed during our experimental work as described earlier in this section, with the locking loop again keeping the laser frequency at the resonant value at all times.
  - *Modulation frequency*: The particular value for the modulation frequency when the modulation depth applied to the laser is fixed also determines the thermal response. If the scan frequency is very low, the laser light spends more time within the cavity thus increasing its temperature and shifting the resonant frequency. This effect is effectively suppressed by increasing the modulation frequency of the ramp, so that the scan time is much faster than the microsphere thermal response. Experimental traces demonstrating this effect are presented in upcoming section 5.4.1.
  - *Current sweep*: When the optical frequency of the laser is tuned across some interval (applying a modulation ramp or just sweeping the set current), a well-known effect in laser diodes takes place: The optical power of the laser output does not remain constant, but linearly increases with increasing current. This makes the optical power coupled into the microsphere during the sweep to

increase. This effect is much smaller than the effects previously described, and does not affect our measurements in practice.

On top of these thermal effects another type of frequency noise must be considered: the emission frequency of the laser changes in time from its set value due to 1/f noise associated with the laser current and temperature controllers, as well as due to mains noise at 50 Hz or higher harmonics. This effect has been treated in detail in section 4.2.1 of chapter 4, and produces frequency shifts much smaller than in the thermal cases described above (these thermal effects can be thought as effectively being low-frequency noise sources also affecting the laser output).

As becomes clear from the previous discussion, the thermal response of our system is a combination of many individual effects simultaneously/alternatively taking place. A rigorous treatment would require further theoretical analysis but it is not necessary in our case: the implemented locking loop, along with an appropriate choice of the modulation frequency, effectively compensates for all of these effects in practice. The laser emission frequency is locked to the WGM centre during our experimental work. Note that this locking loop is not an **absolute** frequency locking loop such as that presented in section 4.3.2 in chapter 4, but exhibits the same *drawback* as the locking technique presented in section 4.3.1: the laser frequency is modulated itself. However this is not a real *drawback* for our purposes, because we are not searching for an absolute frequency locking loop. The aim is to lock the central laser frequency to the centre of the WGM mode at all times, in order to investigate the properties of the whispering gallery mode itself. During all of our experimental work the locking method was routinely implemented in a successful manner for long periods of time (of the order of hours), facilitating data acquisition to a very significant extent.

5.4. RESULTS AND DISCUSSION

5.4.1. SELF-HOMODYNE LINEWIDTH MEASUREMENTS

The linewidths of the two laser sources used during our experimental work have been measured utilising the self-homodyne technique described in section 5.2.3. As discussed there such measurement technique avoids the 1/f frequency noise introduced by the current and temperature control units associated with the lasers, improving the measurement accuracy. The experimental scheme presented in figure 5-3 is implemented, making use of a fibre interferometer with a fixed delay of τ=25μs between its two arms. This corresponds to a cut-off frequency of approximately f_{CUT} (INT) $\approx 1/\tau = 40$ kHz, while light is detected using a photodetector of cut-off frequency f_{CUT} (PD) $\approx$ 10 kHz. As discussed in section 5.2.3 the intensity profile of the detected signal follows a Lorentzian lineshape of the form

$$L(\upsilon) = L_0 + \frac{2A}{\pi}\frac{\Delta\upsilon_L}{4(\upsilon - \upsilon_C)^2 + \Delta\upsilon_L} \tag{5.16}$$

with a FWHM ($\Delta\upsilon_L$) equal to twice the linewidth of the laser source, $\Delta\upsilon_L = 2\Delta\upsilon_{LAS}$. Thus, acquired data are fit to a Lorentzian curve and the linewidth of the laser is obtained from the simple relation

$$\Delta\upsilon_{LAS} = \Delta\upsilon_L/2 \tag{5.17}$$

Results for the two laser sources utilised (DM and DFB LD's) are presented in figure 5-12.

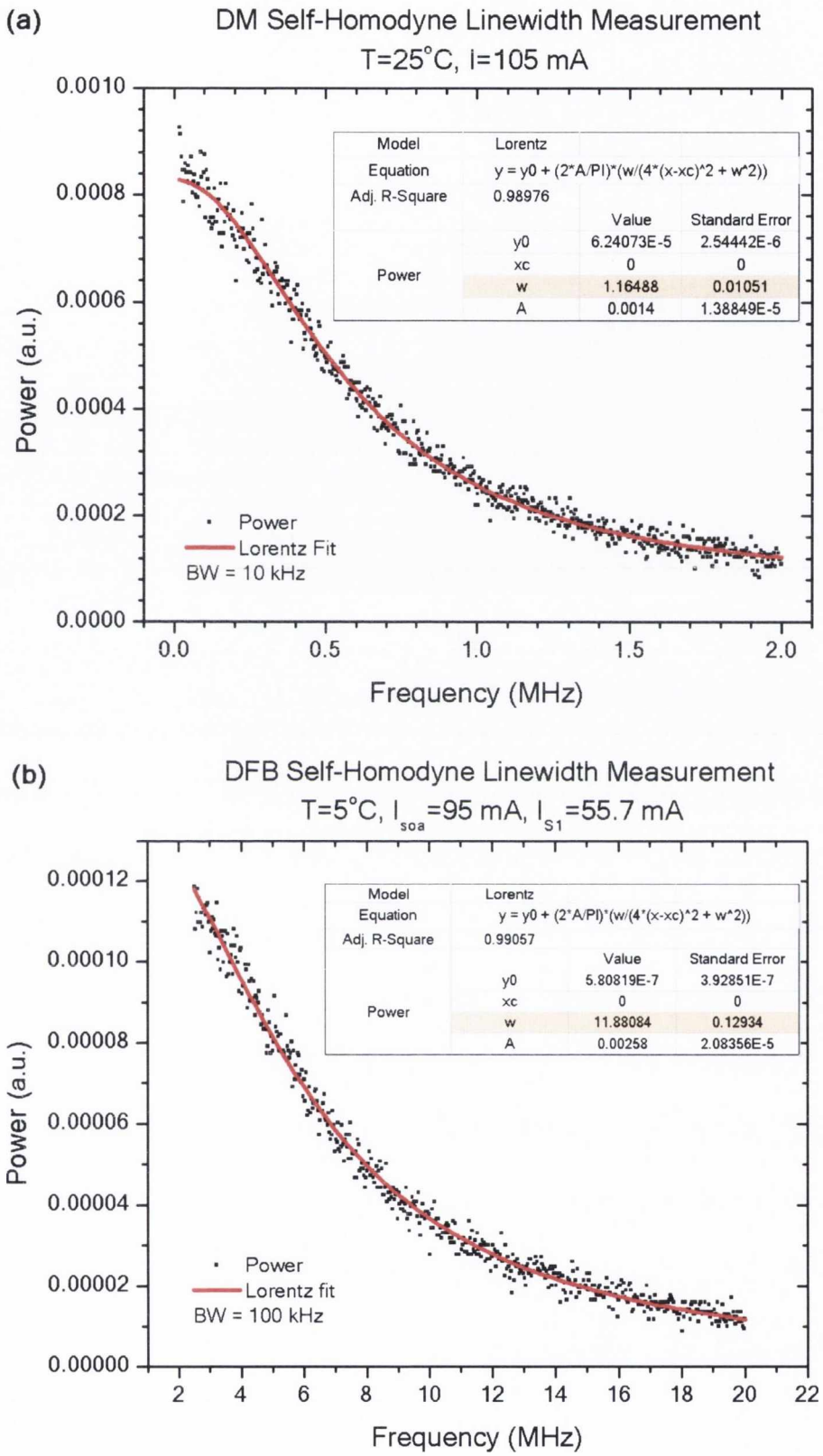

***Figure 5-12**: Self-homodyne linewidth measurement results for the DM (a) and DFB (b) laser sources used during our experimental research.*

Translating these fitting results into relation (5.17) yields a measurement value for the linewidths of the two lasers of

$$\Delta\upsilon_{DM} = \Delta\upsilon_{L_{DM}}/2 \approx 550\ kHz \tag{5.18}$$

$$\Delta\upsilon_{DFB} = \Delta\upsilon_{L_{DFB}}/2 \approx 6.0\ MHz \tag{5.19}$$

As observed, the linewidth characteristics for both lasers are significantly different, with the DM laser diode exhibiting a very narrow output spectrum one order of magnitude smaller than that of the DFB laser diode. The linewidth difference between the two lasers is a key point to successfully perform the microsphere WGM experiments. Because the self-homodyne is a well established and theoretically solid measurement technique, the results for the Lorentzian fits have a small, negligible associated uncertainty. The total error figure is rather determined by repeating the measurement several times (≈5-10) and then estimating the average difference in the extracted linewidth parameter from consecutive readings. The uncertainty associated with the final results in (5.18) and (5.19) was in practice estimated to be $\Delta(\Delta\upsilon_{DM}) \approx 50$ kHz and $\Delta(\Delta\upsilon_{DFB}) \approx 0.5$ MHz.

5.4.2. WHISPERING GALLERY MODE BANDS

As discussed in sections 5.2.4 and 5.3.2 of this chapter, a set of microsphere modes can be excited within the microcavity when the laser emission frequency is modulated over an inverval (i.e. high modulation depth applied to the laser) larger than the free spectral range of the WGM spectrum. The experimental set-up is prepared according to figure 5-9 and the coupling parameters (microsphere-prism alignment, coupling distance and laser polarization) carefully adjusted. When the coupling requirements

are fulfilled a set of modes arises from the flat background and the previous parameters can be further optimized. As discussed in section 5.3.2 the frequency locking loop can be closed at that point, automatically shifting the central frequency of the laser until it gets eventually locked to the centre of the strongest mode within the band. Then the modulation depth applied to the laser is decreased, and attention focused onto a single microcavity mode.

Experimental results showing a typical WGM band excited within the microsphere during our experimental work are presented in figure 5-13.

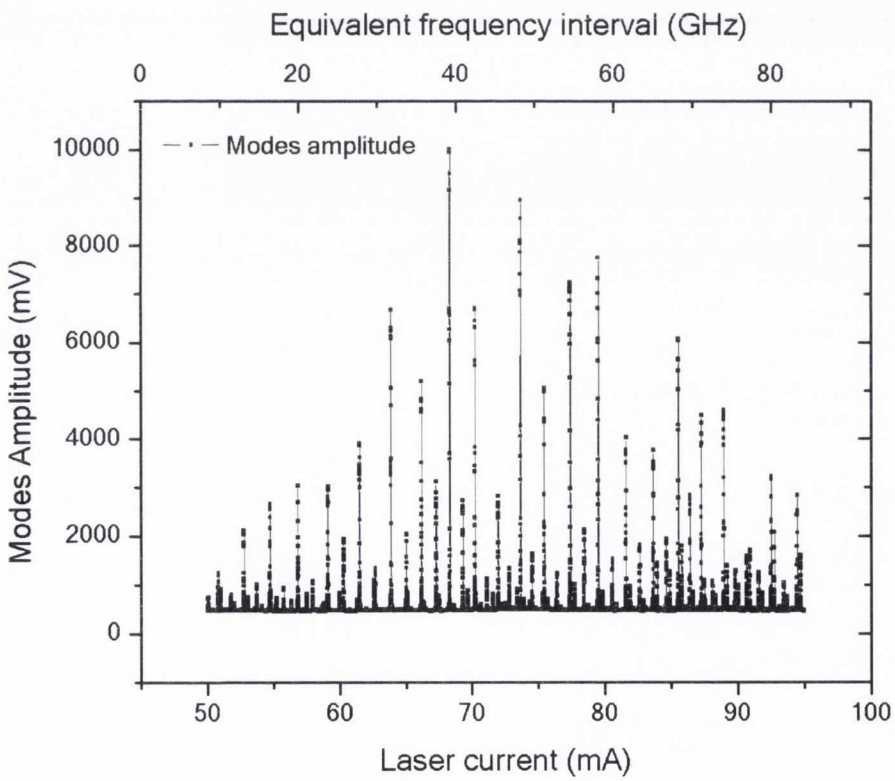

***Figure 5-13**: Experimental results for a WGM band around 1.5 μm excited within the microsphere over a wide tuning interval. A DFB laser operating at T = 16°C is used, and emission frequency tuning achieved by sweeping the laser injection current.*

Note that in this case frequency tuning was achieved by sweeping the laser current rather than applying a modulation signal V_{MOD} because of the wide scanning interval. As discussed in section 5.3.2 data were accordingly acquired using a GPIB interface and personal computer rather than a digital oscilloscope, as shown in figure 5-9. Results shown correspond to the DFB laser source, scanned over a current interval of $\Delta I = 45$ mA approximately equivalent to a wavelength range of $\Delta\lambda = 0.58$ nm (the DFB DC tuning rate was independently measured, and approximately equals $\Delta\lambda/\Delta I \approx 0.013$ nm/mA).

An additional figure (5-14) is presented below including the experimental results for the same WGM band corresponding to a narrower frequency range.

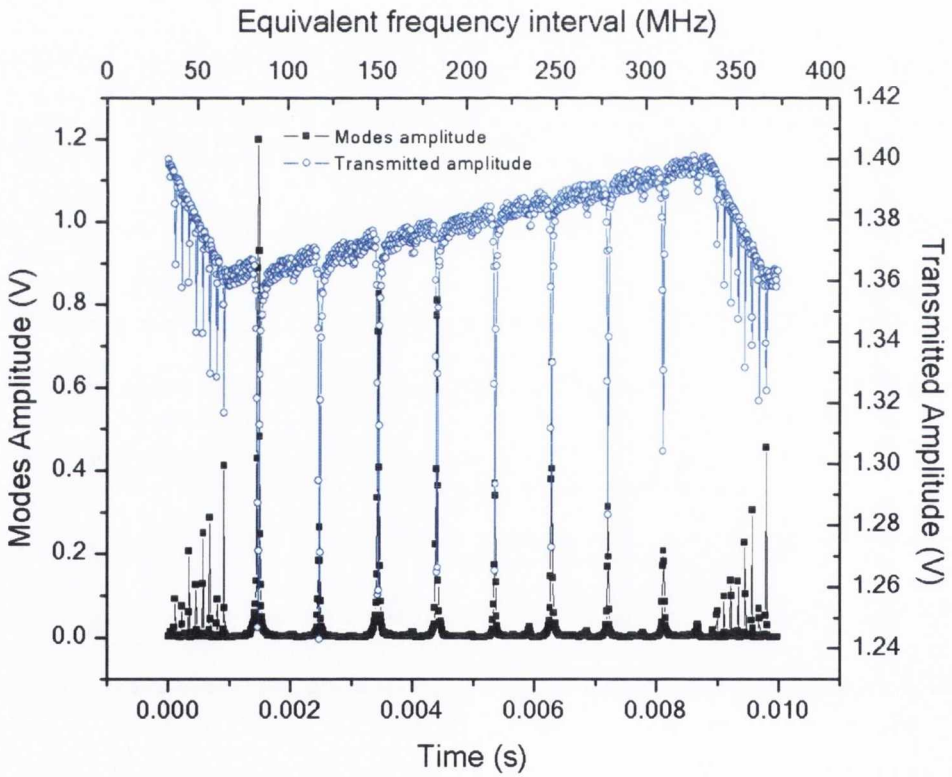

Figure 5-14: *Experimental results for the WGM band presented in figure 5-13 over a narrower frequency range. The emission frequency of the DFB laser is now tuned using a modulation ramp, and the transmitted signal through the optical prism included.*

In this case tuning of the DFB emission frequency is achieved using a modulation ramp and data acquired with the help of a digital oscilloscope (note how the horizontal axis is now presented in a time scale). The transmitted signal through the optical prism is now included, consisting of consecutive *absorption* peaks which correspond to each of the excited WGM's within the microsphere. These two figures qualitatively illustrate the different laser tuning techniques, detection schemes and WGM band structure discussed in previous sections during this chapter. Note how the transmitted amplitude signal through the optical prism presents a small non-zero slope, as a result of the optical power of the laser diode increasing as the current is swept (as discussed in section 5.3.2).

5.4.3. THERMAL EFFECTS

The different thermal effects affecting the size of the microspheres during experimental work have been discussed in detail in section 5.3.2. These effects ultimately lead to a change of the resonant frequency v_0 of the excited WGM, but they do not affect our experimental results as they are compensated by the implemented active feedback loop. The set emission frequency of the laser source is locked to the resonant value at all times, facilitating the analysis of data acquired for the WGM's. In this section some experimental data are presented to illustrate the observed results for these thermal effects, as well as the subsequent minimisation.

The results for the microsphere heating and change of the resonant frequency are first shown in figure 5-15. Data correspond to a single WGM excited within the microsphere making use of the narrow linewidth DM laser diode, after coupling distance and polarization have been optimized to get good SNR for the mode. In this case the laser emission frequency is modulated using a triangular voltage ramp of low

frequency $f_{MOD}^{LOW} \approx 2.2$ Hz and peak-to-peak amplitude $V_{MOD} \approx 275$ mV. A full period is shown in the figure, and the difference between the positive and negative slope intervals become immediately clear. Because the modulation signal is applied at a low frequency rate, the optical power inside the microsphere builds up during the WGM scan time and heats the microcavity producing a thermal shift of the resonant wavelength. The intensity profile of the mode is distorted from its real lineshape, with the final results across the positive and negative slope intervals different from each other.

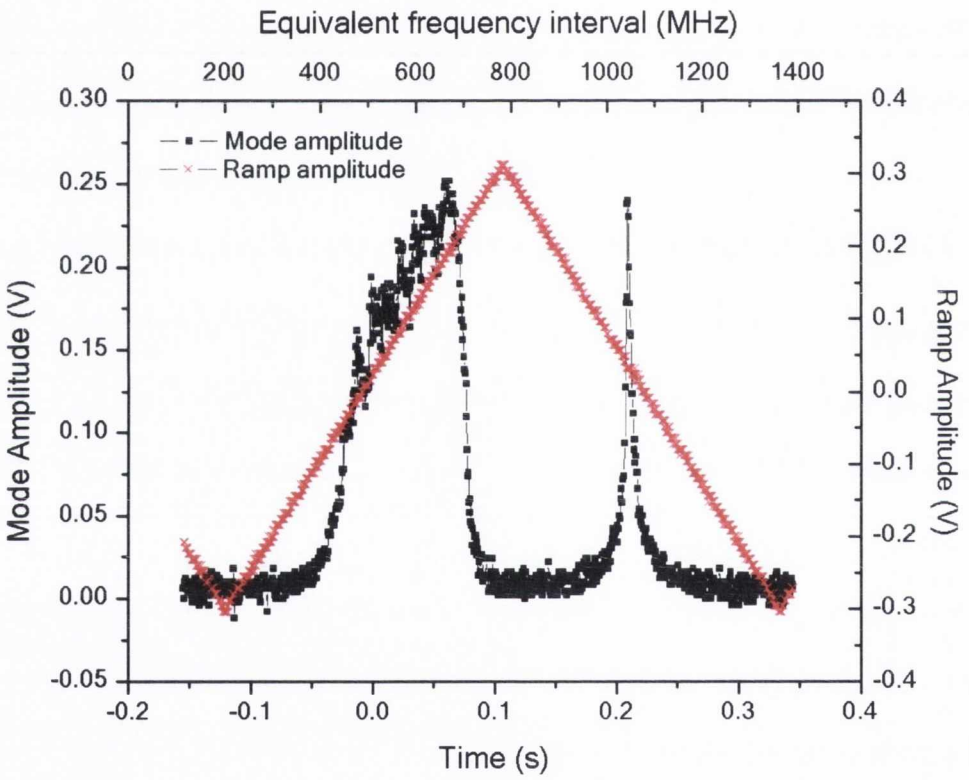

***Figure 5-15**: Experimental results for the excitation of a single WGM within the microsphere using the DM laser modulated at a low frequency $f_{MOD}^{LOW} \approx 2.2$ Hz.*

The behavior of the thermal effect during scan time can be understood according to the additional figure 5-16, which corresponds to the positive-slope period WGM profile shown in figure 5-15 above. The observed thermal-induced shift can be

explained as follows. When scan time equals t_1 during the initial stage of the modulation ramp, the laser frequency is aligned with the high-frequency wing of the unperturbed mode of resonant optical frequency $\upsilon^1{}_0$ and the correspondent amplitude A_1 recorded. As light is coupled into the microcavity the resonant frequency is red-shifted due to thermal effects, with a recorded amplitude A_2 at some intermediate time t_2 when the whole WGM is centred at a resonant frequency $\upsilon^2{}_0$. At time t_3 the laser frequency is exactly aligned with the new resonant value $\upsilon_0{}^3$, so that the amplitude A_3 corresponds to the WGM maximum.

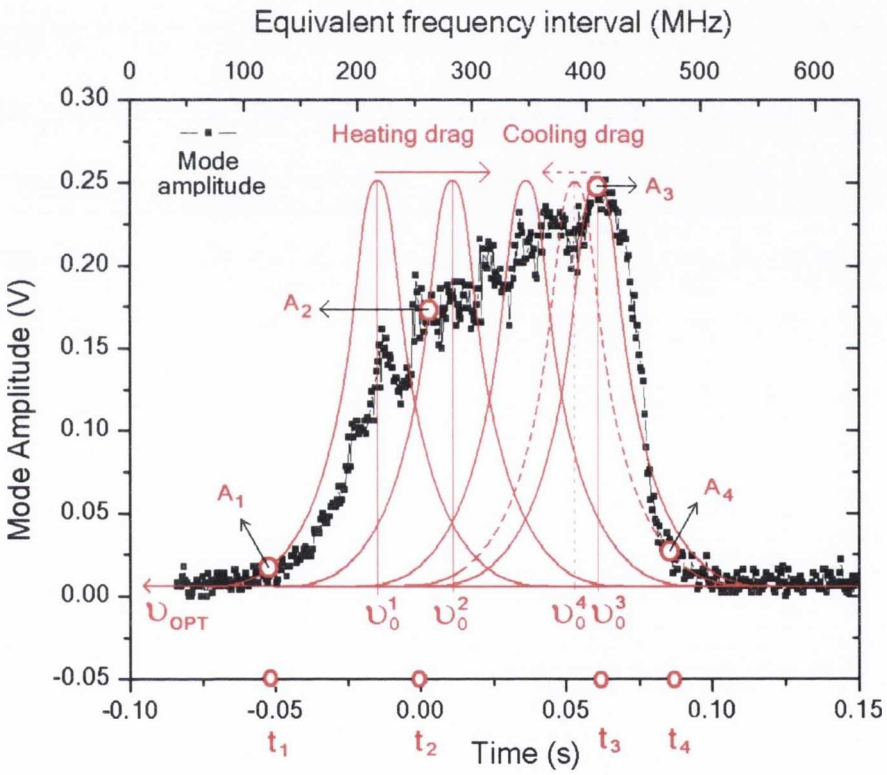

***Figure 5-16**: Experimental results corresponding to the positive slope interval for the excited WGM within the microsphere presented in figure 5-15. The behavior of the thermal-induced shift of the WGM resonant optical frequency υ_0 during scan time is illustrated here at four different points.*

At this point a fundamental change in the thermal *drag* behaviour of the system occurs: because the laser frequency is changing at a faster rate than the induced thermal shift, the laser will target the right hand side of the WGM profile at any time $t>t_3$. This means that the optical power coupled into the microsphere starts to decrease, thus **changing the sign** of the temperature-induced resonant frequency shift. As a result, the recorded amplitude A_4 of the WGM at a time $t_4>t_3$ is dramatically decreased because the resonant frequency υ^4_0 is now shifting in the opposite direction to the laser frequency sweep. This effect gives any WGM mode recorded at low scan frequencies the particular intensity lineshape observed in the figure, facilitating the assessment of this modulation-frequency-related thermal effect. As discussed in previous sections the effect is effectively suppressed by increasing the modulation frequency of the ramp f_{MOD} until the laser frequency sweep becomes faster than the thermal effect response. Figure 5-17 corresponds to an excited WGM recorded using the DM laser modulated at a high frequency value $f_{MOD}^{HIGH} \approx 1.1$ kHz where the thermal effect has been effectively suppressed. A small asymmetry in the wings of the Lorentzian profile can be still observed, but in practice does not affect the results presented in upcoming sections.

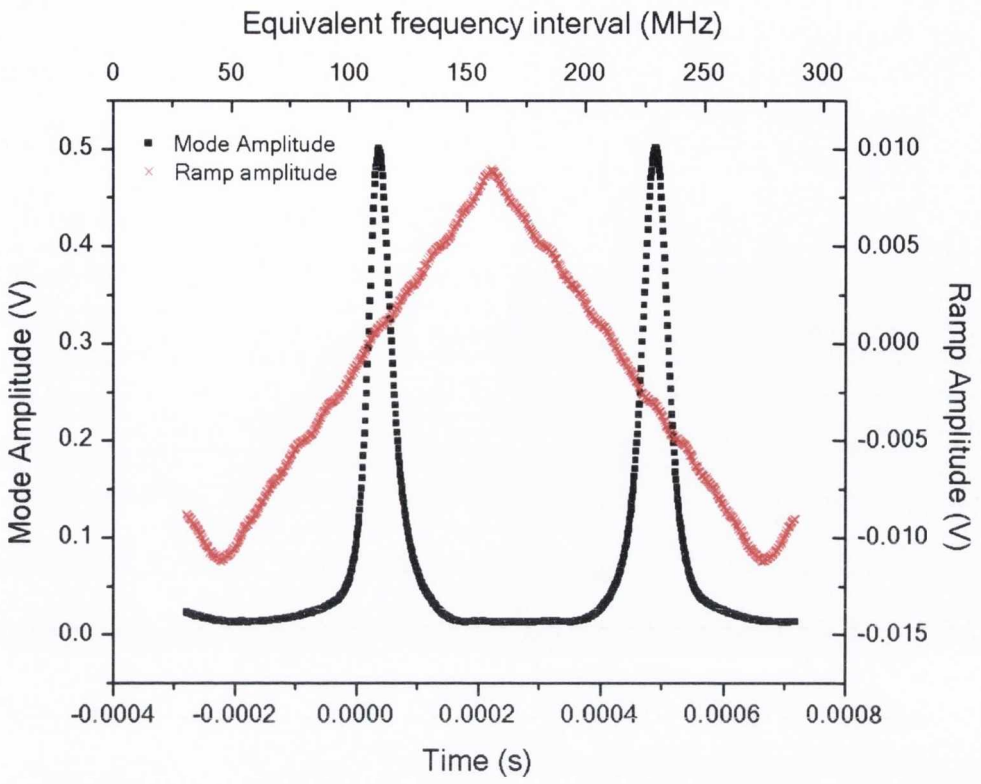

***Figure 5-17**: Experimental trace for a WGM excited within the microsphere using the DM laser modulated at a frequency $f_{MOD}^{HIGH} \approx 1.1$ kHz. The thermal-induced shift of the mode resonant frequency due to a low modulation frequency has been effectively suppressed.*

5.4.4. WGM'S AND NARROW LINEWIDTH LASER

In the first case a narrow-linewidth DM laser diode is used to excite the WGM's within the microsphere. Description of the slotted geometry of the laser has been presented in section 5.2.2 and self-homodyne linewidth measurements yielding a value of $\Delta\upsilon_{DM} \approx 550$ kHz included in section 5.4.1. The emission frequency of the laser was tuned using a modulation ramp at a frequency of $f_{MOD} = 1.124$ kHz, avoiding thermal effects which would otherwise distort the WGM intensity profile. A wide spectral interval was first targeted allowing for observation of complete WGM bands excited within the microsphere. The laser temperature and injection current

were then tuned until the strongest band was targeted, and polarization of the laser optimized. At that point the frequency locking loop was closed, locking the emission frequency of the laser to the strongest mode within the band. The modulation depth applied to the laser was then decreased until only the strong WGM was observed in the oscilloscope. Coupling distance was finally optimized to increase the SNR of the detected signal. The central operating wavelength was measured corresponding to a laser temperature of T_{DM} = 26.6 °C and laser injection current of I_{DM} = 109.2 mA, yielding a value of λ_C^{DM} = 1537.102 nm. Several samples for the WGM were then recorded, after which the modulation depth was increased to get a two-point current measurement in order to calibrate the horizontal axis of the acquired signal into a frequency scale. The ratio of small/high modulation depth, as well as the measured laser DC tuning rate of $(\Delta\lambda/\Delta I)_{DM} \approx 0.0062$ nm/mA, were also included in this calibration. This frequency calibration is necessary to compare sets of data from different lasers. On the other hand, in order to minimise any small drift of the coupling distance that may have occurred during data acquisition time, two consecutive measurements were performed. A coupling distance corresponding to a piezo controller voltage of V_{COUP1} = 10.3 V was first chosen and then the two DM and DFB lasers consecutively used to record the WGM profile. Then the coupling distance was optimized again, corresponding to a value of V_{COUP2} = 11.3 V, and the same lasers used to record the WGM intensity profile again. The observed change in coupling distance was negligible, so that both sets of data can be directly compared.

Results are presented in figure 5-18 corresponding to the WGM mode trace at the two coupling distances corresponding to V_{COUP1} = 10.3 V and V_{COUP2} = 11.3 V within the optimum SNR regime. Appropriate theoretical fits of the experimental results to a Lorentzian curve are included, after shifting the data to a zero baseline and translating

it to a frequency scale. Some small asymmetry in the mode wings can be observed due to residual thermal dragging effects, though it does not significantly affect the theoretical fit results. The fits yield WGM widths of respectively $\Delta\upsilon^{DM1}{}_{WGM} \approx 10.9$ MHz and $\Delta\upsilon^{DM2}{}_{WGM} \approx 11.5$ MHz for the two coupling distances, with an average value for the mode width of

$$\Delta\upsilon_{WGM}^{DM} \approx \mathbf{11.2\ MHz} \tag{5.20}$$

which is much greater than the measured laser linewidth of $\Delta\upsilon_{DM} \approx 550$ kHz. Here lies the key point of these experimental results: The frequency noise associated with the laser linewidth is transformed into AM noise via the sphere mode AM/FM conversion factor; however, because the linewidth of the laser is much smaller than the WGM width, the resulting AM noise is negligible and cannot be observed: The WGM traces presented in figure 5-18 correspond to the unperturbed, *real* intensity profile of the whispering gallery mode. Stability of the lineshape was experimentally observed. This is a very important fact to keep in mind in upcoming section 5.4.6 when analysing the experimental results obtained with the two different lasers.

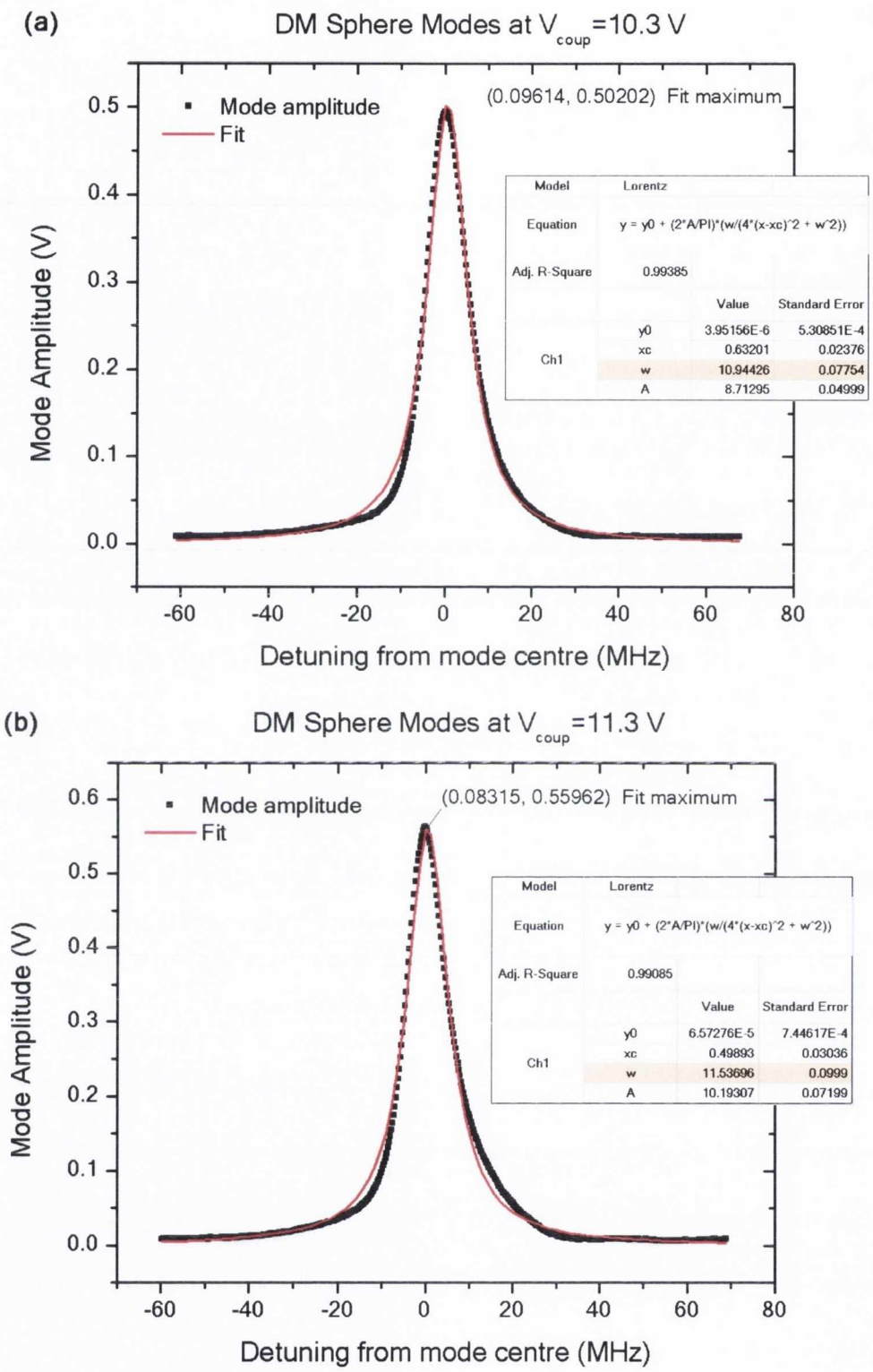

***Figure 5-18**: Experimental results for the microsphere WG mode excited at two different coupling distances (corresponding coupling voltages (a) 10.3 V and (b) 11.3 V) with a narrow linewidth DM laser ($\Delta\upsilon_{DM} \approx 550$ kHz).*

Estimation for the value of the Q factor of the spheres from the experimental data yields a value of $Q \approx 10^7$, confirming that the microspheres possess a high quality surface with very low losses associated. Data were acquired during a time interval of around 20 minutes so that the quality of the microresonators is assumed to remain constant, a key feature in order to compare results using two different lasers.

5.4.5. WGM'S AND WIDE LINEWIDTH LASER

In the second case the WGM mode was excited using a DFB laser with a measured linewidth of approximately $\Delta\upsilon_{DFB} \approx 6$ MHz as shown in previous figure 5-12. The same procedure to locate the WGM band containing the strongest modes and lock the emission frequency of the laser to the strongest one within the band was applied as described in the previous section. In order to facilitate comparison of data acquired with the two lasers, the polarization state of the DFB laser was adjusted to be the same as that of the DM case. Coupling distance was kept at the same value for both lasers as described in the previous section. The laser operating central wavelength was measured to be $\lambda_C^{DFB} = 1537.134$ nm at a laser temperature of $T_{DFB} = 4$ °C and injection current of $I_{DFB} = 52.92$ mA. The modulation ramp was applied at the same frequency of $f_{MOD} = 1.124$ kHz and individual traces for the WGM were recorded consecutively. The modulation depth was then increased in order to perform the two-point current measurement for calibration purposes in the same manner as in the DM laser case. In this case the measured DC tuning rate of the DFB laser yielded a value of $(\Delta\lambda/\Delta I)_{DFB} \approx 0.0132$ nm/mA. It is very important to emphasize that we must work in the same wavelength region and polarization state as that of the DM laser, in order to excite microsphere modes within the same band for ease of comparison of experimental data.

Results for the obtained data are presented in figure 5-19, containing a group of twenty consecutive trace samples for the excited WG mode at each of the two coupling distances V_{COUP1} = 10.3 V and V_{COUP2} = 11.3 V. Amplitudes have been normalized to match those obtained with the DM laser in order to compare the results from both lasers, and data are presented on a carefully scaled frequency axis as previously explained. The calculated average and Lorentzian fit in each case are included, yielding values for the WGM linewidth of $\Delta\upsilon^{DFB1}{}_{WGM} \approx 15.2$ MHz and $\Delta\upsilon^{DFB2}{}_{WGM} \approx 14.8$ MHz respectively, with an average of approximately

$$\Delta\upsilon_{WGM}^{DFB} \approx \mathbf{15.0\ MHz} \tag{5.21}$$

The frequency noise associated with the laser linewidth is again transformed into amplitude noise by the microsphere excited WGM, which is effectively acting as an AM/FM converter according to the Lorentzian lineshape described in the previous section. However, the measured DFB laser linewidth of $\Delta\upsilon_{DFB} \approx 6.0$ MHz presented in section 5.4.1 is now equivalent to approximately 40% of the WGM width. Here lies the main difference as compared with the results using the narrow linewidth DM laser: in this case the DFB laser linewidth is of the order of the WGM width and the induced variations in the amplitude can be observed across the whole Lorentzian lineshape. This amplitude noise pattern is thus directly related to the linewidth properties of the laser source, and can be utilised to estimate such value.

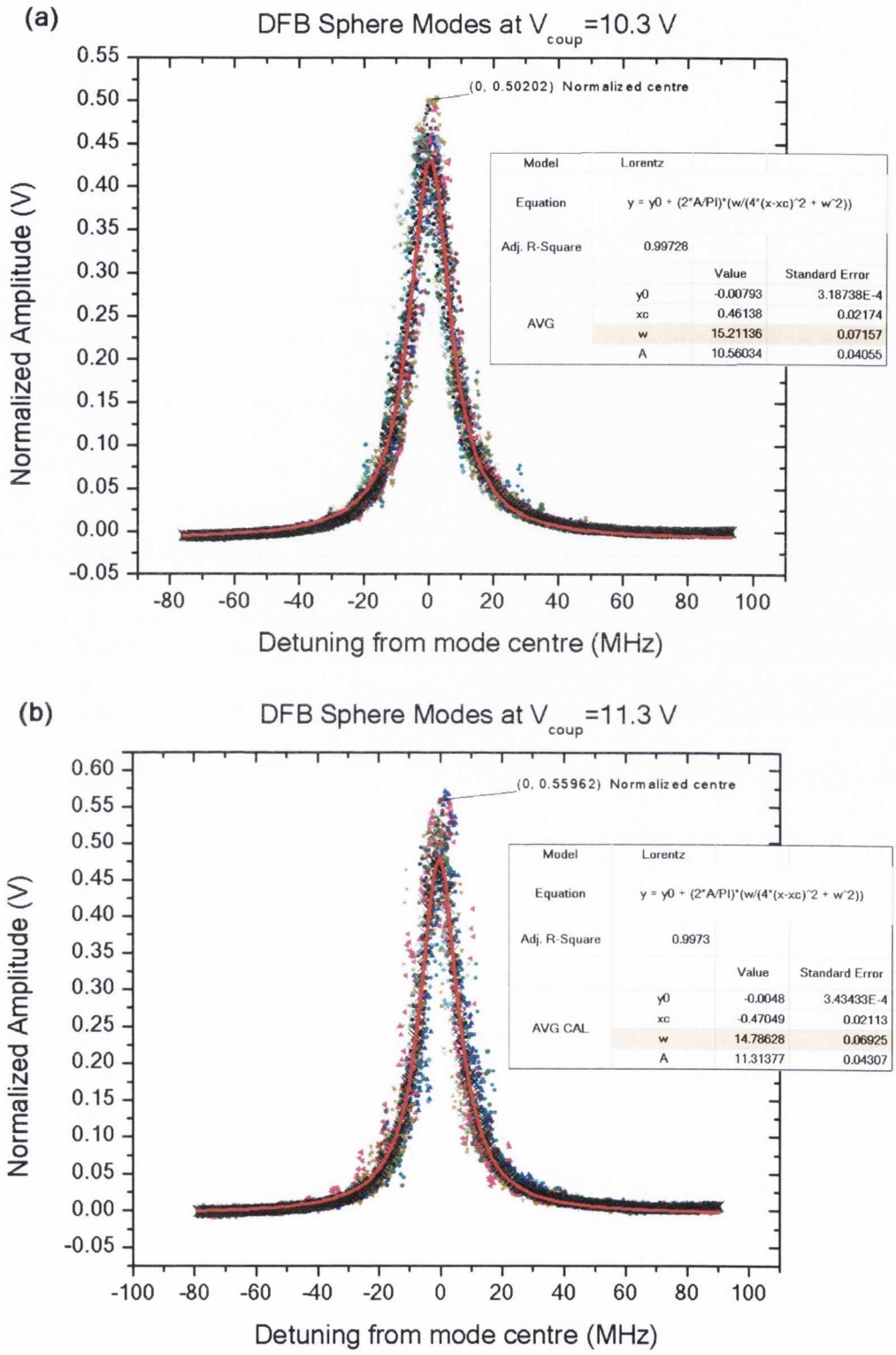

***Figure 5-19**: Experimental results for the microsphere WG mode excited at two different coupling distances (corresponding coupling voltages (a) 10.3 V and (b) 11.3 V) with a wide linewidth DM laser ($\Delta\upsilon_{DFB} \approx 6$ MHz). Calculated average and corresponding Lorentzian fits are included.*

5.4.6. DATA ANALYSIS AND LASER LINEWIDTH

As it becomes clear from the discussion in previous section, the amplitude noise pattern observed across the intensity profile of a WGM excited within a high-Q microspherical resonator is directly related to the linewidth of the laser source utilised. This assertion only applies when additional effects distorting the intensity profile of the microsphere mode have been effectively suppressed, such as thermal effects associated with the laser source or external perturbations as discussed in section 5.3.2. Thus, the noisy pattern can be analysed and information extracted regarding the underlying characteristics of the noise characteristics of the laser emission frequency. A simple model to account for the experimental results presented in previous sections will be presented herein, and compared to the independent linewidth results obtained using a self-homodyne measurement technique as presented in section 5.4.1.

A schematic diagram of the simple model utilised to analyse the presented experimental results is sketched in figure 5-20 below.

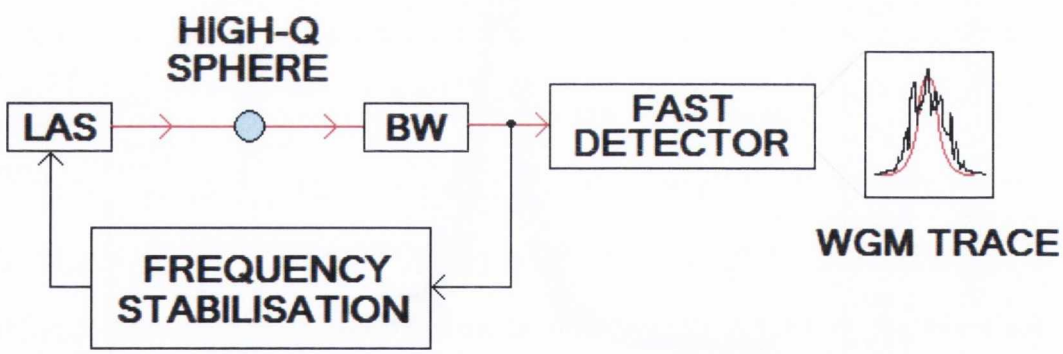

***Figure 5-20**: Schematic diagram for the simple model utilised to analyse the experimental WGM results presented in this chapter and extract information about the laser source linewidth.*

In our simple model laser light is coupled into the high-Q microsphere and then scattering from its surface detected with an appropriate fast photodetector. Coupling of light into the microresonator can be achieved by the optical prism coupling method described in section 5.3.2. Some feedback system is implemented, which effectively suppresses any frequency effect distorting the acquired WGM trace other than that due to the laser linewidth. Some assumptions are made which apply to our experimental results:

1. The output of the laser source follows a Lorentzian lineshape (this assumption is valid for most laser diodes operating above threshold, where the amplitude noise of the optical field can be neglected and only the phase noise due to spontaneous emission processes within the laser active region contribute to the final laser linewidth [5, 25]).
2. The effective system bandwidth is large enough so it does not significantly affect the amplitude noise pattern in the WGM trace acquired.
3. The Q-factor of the microcavity remains constant during the timescale of the experimental work.

In all cases, the excited WGM acts as an effective AM/FM converter where frequency noise introduced by the laser source is transformed into amplitude perturbations. Under these assumptions, two cases can be distinguished where the intensity profile of the excited WGM has different characteristics:

A) *The laser linewidth is much smaller than the WGM width,* $\Delta\upsilon_{LAS} << \Delta\upsilon_{WGM}$:

In this case the amplitude noise associated with the frequency noise of the laser is negligible and the measured WGM linewidth is only limited by the microsphere Q factor (i.e., its surface quality). A smooth profile is observed and the measured width $\Delta\upsilon^{Q}_{WGM}$ corresponds to the *real* value for the surface-limited mode, unperturbed by any other sources other than the physical characteristics of the microresonator itself. This case corresponds to the experimental results presented in section 5.4.4, obtained using the DM laser diode.

B) *The laser linewidth is of the order of the WGM width,* $\Delta\upsilon_{LAS} \approx \Delta\upsilon_{WGM}$. In this case the amplitude noise associated to the frequency noise of the laser cannot be neglected, so that a characteristic noise pattern can be clearly observed across the WGM. The resulting profile of the acquired microsphere mode thus corresponds to the convolution of the laser intensity profile and the unperturbed microcavity mode described in A). Because both contributions are Lorentzian, the resulting lineshape for the WGM is also Lorentzian with a linewidth equal to the sum of both contributions,

$$\Delta\upsilon^{N}_{WGM} = \Delta\upsilon^{Q}_{WGM} + \Delta\upsilon_{LAS} \tag{5.22}$$

where the superscript *N* refers to the *noisy* character of the recorded WGM. This case corresponds to the experimental results presented in section 5.4.5, obtained using the DFB laser diode.

Equation (5.22) thus illustrates the key relation in order to extract the information about the laser source linewidth from the experimental data recorded:

An estimation of the laser linewidth $\Delta\upsilon_{LAS}$ can be obtained by simply subtracting the WGM width values obtained using the wide and narrow linewidth lasers, respectively:

$$\Delta\upsilon_{LAS} = \Delta\upsilon_{WGM}^{N} - \Delta\upsilon_{WGM}^{Q} = \Delta\upsilon_{WGM}^{DFB} - \Delta\upsilon_{WGM}^{DM} \quad (5.23)$$

Thus, according to our experimental results presented in (5.20) and (5.21) we obtain a final result for the DFB laser linewidth of

$$\boldsymbol{\Delta\upsilon_{DFB}^{2laser} \approx (15.0 - 11.2) = 4.8\ MHz} \quad \textbf{(5.24)}$$

The superscript *2laser* emphasizes the fact that the WGM data acquired using the *two* laser diodes have been used to extract the final result.

Error analysis

In order to estimate the uncertainty associated with the presented results it is necessary to perform an appropriate analysis of the main error sources in the system.

The first significant error source for the linewidth parameter extracted from the WGM traces is that related to the finite number of measurements. This error source **only** applies to the DFB WGM traces presented in figure 5-19, where a sample of N=20 traces has been used to calculate the mode linewidth at each of the two coupling distances $V_{COUP1,2}$. In the case of the DM sphere modes of figure 5-18 high stability of the WGM lineshape was routinely observed and thus no significant statistical variation of the extracted linewidth was assumed. Hence, the error associated with the limited sample size for the DFB case can be estimated using the so-called *Bootstrap method* [26], a special case of the widely spread Monte-Carlo data simulation

techniques. This method can be applied to N *independent and identically distributed (*or *iid)* data points, meaning that the sequential order of the data points is not of consequence to the process used to get the fitted parameters ***a***. Such is the case of the Lorentzian linewidth of the fitted WGM data presented in previous sections, as the result does not depend on the sequential order of the N=20 traces recorded at each coupling distance. The first stage to apply the Bootstrap method is to generate *synthetic* data sets $\{D^S_i\}$, each of them of the same size N than the original set D_0. This is achieved by simply drawing N data points from the original set at a time *with replacement*, meaning that each original data point can be randomly selected more than once when generating a particular D^S_i. The next stage is to subject each of these synthetic sets to the same fitting procedure as that performed on the original one, obtaining a set of simulated fitted parameters $\{a^S_i\}$. The key statement of the Bootstrap method is that **the set of parameters $\{a^S_i\}$ is distributed around a_0 in the same way than a_0 is distributed around the true value a_{true}.** Hence, the standard deviation associated with the set $\{a^S_i\}$ can be regarded as a valid estimation of the error in the fitted parameter a_0.

The results for the application of the bootstrap method to the DFB laser WGM traces shown in figure 5-19 are presented in figure 5-21 and table 5-1. Ten synthetic data sets have been generated from each of the two N = 20 WGM traces sets at the two coupling distances V_{COUP1} = 10.3 V and V_{COUP2} = 11.3 V. Each of the synthetic sets has been fitted to a proper Lorentzian lineshape and the correspondent mode width extracted, allowing for consequent computation of the average and standard deviation of the simulated fitted set. As discussed earlier within this section, the standard deviation represents a proper estimation of the WGM linewidth error associated with

the finite sample size, yielding a value of $\sigma_{bootstrap} = \Delta_{SAMPLE}(\Delta\upsilon_{WGM}) \approx$ **0.3 MHz** in this case.

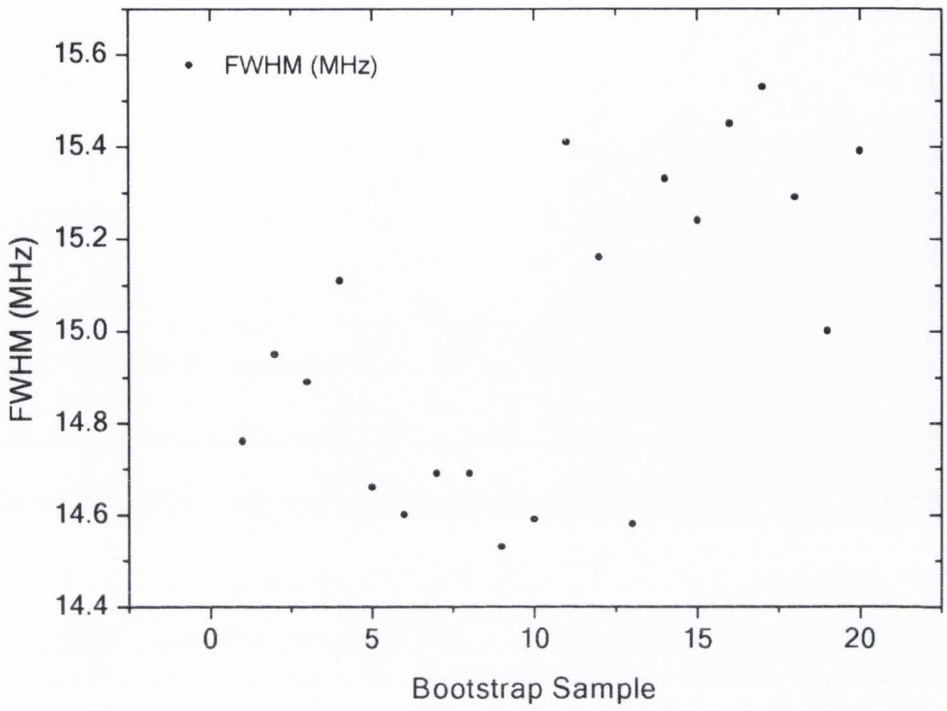

***Figure 5-21**: Results for the application of the Bootstrap data simulation method to the DFB WGM traces of figure 5-19. The average and standard deviation of the simulated fitted linewidths are included in table 5.1.*

Table 5-1 · Bootstrap Fit Results

Sample	1	2	3	4	5	6	7	8	9	10
Mode FWHM (MHz)	14.76	14.95	14.89	15.11	14.66	14.60	14.69	14.69	14.53	14.59
Sample	11	12	13	14	15	16	17	18	19	20
Mode FWHM (MHz)	15.41	15.16	14.58	15.33	15.24	15.45	15.53	15.29	15.00	15.39
Statistics	Mean (MHz)		15.00			Standard Deviation (MHz)			0.34	

The second important source of error in the estimation of the sphere modes linewidth is that related to the shift of the coupling distance. As discussed in previous sections WGM traces can be optimized by tuning the coupling distance between the glass microsphere and the optical prism. If the sphere is too far from the prism only a small fraction of the evanescent field is coupled into the microcavity, and the intensity of the recorded WGM's becomes very small. When the coupling distance decreases the overlap with the evanescent field increases and the intensity of the sphere modes is enhanced. However, if the coupling distance gets too small the WGM itself may decay into the prism volume, giving rise to a broadening of its intensity profile. Thus, if the coupling distance changes significantly during the measurement interval some effective error is introduced in the extracted FWHM parameter.

In the case of the DM and DFB sphere modes presented in sections 5.4.4 and 5.4.5, two sets of WGM's have been consecutively recorded at two different coupling distances. Each set of modes has been independently fitted and results for the linewidth extracted, as shown in figures 5-18a,b (DM laser) and 5-19a,b (DFB laser). Thus, the actual fit results can be used to realistically estimate the effective error introduced in the linewidth parameter by any shift of the coupling distance. According to such values the difference of the measured WGM width for a given laser at two different coupling distances is

$$\begin{aligned} \Delta_{COUP}(\Delta\upsilon_{WGM}^{DM}) &\approx \Delta\upsilon_{WGM,b}^{DM} - \Delta\upsilon_{WGM,a}^{DM} = |11.5 - 10.9| = 0.6\ MHz \\ \Delta_{COUP}(\Delta\upsilon_{WGM}^{DFB}) &\approx \Delta\upsilon_{WGM,b}^{DFB} - \Delta\upsilon_{WGM,a}^{DFB} = |14.8 - 15.2| = 0.4\ MHz \end{aligned} \tag{5.25}$$

Because the coupling distance is a common parameter for both lasers, an average of the previous values is calculated to estimate the effective error in the WGM linewidths, $\Delta_{COUP}(\Delta\upsilon_{WGM}) \approx$ **0.3 MHz**, valid for both data sets.

In this way the total error associated with the WGM's linewidth values can be properly estimated. As explained earlier within this section, the error associated with the finite data sample size only applies to the DFB sphere modes, while that associated with the shift of the coupling distance does affect the sphere modes for both the DM and DFB laser diodes. Because both effects are independent from each other the two error contributions are summed up when required, yielding the following results for the total error in the measured WGM linewidths:

$$\begin{aligned} \Delta_{TOT}(\Delta\upsilon_{WGM}^{DM}) &= \Delta_{COUP}(\Delta\upsilon_{WGM}) \approx 0.3\ MHz \\ \Delta_{TOT}(\Delta\upsilon_{WGM}^{DFB}) &= \Delta_{COUP}(\Delta\upsilon_{WGM}) + \Delta_{SAMPLE}(\Delta\upsilon_{WGM}) \approx 0.6\ MHz \end{aligned} \tag{5.26}$$

Applying these results to the DFB laser linewidth estimation given in (5.24) the total associated error can be calculated, yielding a value of

$$\boldsymbol{\Delta\left(\Delta\upsilon_{DFB}^{2laser}\right)} = \Delta_{TOT}(\Delta\upsilon_{WGM}^{DM}) + \Delta_{TOT}(\Delta\upsilon_{WGM}^{DFB}) \approx \mathbf{0.9\ MHz} \tag{5.27}$$

Thus, we can now compare the values for the DFB laser linewidth obtained using the WGM method with that extracted from the independent self-homodyne measurements presented in section 5.4.1. Table 5-2 summarizes the results, including the relative difference of the WGM results with the self-homodyne approach along with the estimated accuracy of each of them.

Table 5-2 · DFB laser linewidth measurement results				
MEASUREMENT TECHNIQUE	**Corresponding results**	**$\Delta\upsilon_{DFB}$**	**Relative difference from self-homodyne result**	**Estimated accuracy achieved**
		MHz	%	MHz
Self-Homodyne	(3.7)	6.0	-	≈ 0.5
WGM-based Two lasers	(3.12)	4.8	≈ 20	≈ 0.9

We can draw some conclusions based on these results. On one hand, it can be noted that the relative difference of the WGM-based results compared with the self-homodyne approach yields a significant value of ≈ 20%. However, we can observe on the other hand that the estimated accuracy achieved during experimental work is of the order of 1 MHz. This is equivalent to a relative difference in the laser linewidth of 16%, which strongly supports that the WGM-based experimental results agree with the independent self-homodyne measurement within experimental error. Such a conclusion makes our presented experimental research a success, as the aim was not to improve the accuracy of well-established laser linewidth measurement techniques but rather to propose and demonstrate the capability of a completely different experimental scheme for the same purpose. Note that our microsphere-based techniques, in a similar way as the self-homodyne and *self-heterodyne* techniques discussed in section 5.2.3, effectively suppress the 1/f noise affecting the system, a major limitation in heterodyne linewidth measurements. The accuracy of this novel microsphere-based scheme could be improved in several ways. The microsphere fabrication process could be optimized, giving rise to higher Q-factors which would

increase the AM/FM WGM response. A lower-noise transimpedance amplifier would also improve the SNR of the acquired signals. Modulation of the laser sources could be shifted to higher frequencies, meaning that the locking loop would further reduce the system 1/f noise. Frequency-induced thermal effects would be also further minimised. Together with of all these factors, a deeper theoretical analysis could be carried out to analyse the acquired data in more detail. The fine structure of the observed AM noise is related to the averaged instantaneous departure $\delta\upsilon(t)$ of the laser emission frequency from its ideal value $\upsilon_0(t)$ at a time t over the measurement time $\delta\tau$. Developing an appropriate model to perform a statistical analysis of this fine structure would allow us to gain a deeper understanding of the processes ultimately limiting the measured laser linewidth. A very detailed analysis of the most important statistical aspects of optical frequency measurement has been carried out by Allan [27] and Cutler [28], including the effects of the finite measurement time in the final results. The relationship of the lineshape of the laser output power spectrum and the frequency noise has been studied in detail by Stephan et al. in [7], while a more comprehensive study has been published by Petermann [8]. Optimizing the coupling of light into the microsphere and thus improving the SNR of the acquired signal would ultimately make the use of an optical amplifier unnecessary, increasing the total system bandwidth and thus improving the quality of a statistical-based analysis.

Wide linewidth laser and standard deviation

An additional approach to estimate the linewidth of a laser source making use of our WGM scheme can be understood on the basis of the AM/FM noise conversion introduced by the microcavity mode. The microcavity behaves as an effective absorber in a similar fashion as a frequency-dependent absorbing transition in a gas

that changes the optical power transmitted through a gas-filled cell or HC-PBF. In the case of a gas, the AM/FM relation which describes the gas absorption lineshape $I(\upsilon)$ can exhibit a Gaussian, Lorentzian or Voigt profile depending on the specific pressure regime. In the case of a microsphere, the AM/FM relation is described by a Lorentzian lineshape provided that any effects significantly distorting the lineshape are effectively suppressed. As explained in section 5.3.2, an appropriate feedback loop is implemented in our case that effectively suppresses any of these effects, allowing for Lorentzian fit of the experimental data recorded. Only when the linewidth of the utilised laser source is of the order of magnitude of the WGM width does this Lorentzian profile become distorted: some amplitude noise is introduced in the unperturbed profile due to the laser source frequency noise.

In the previous section we have successfully analysed the *average* amplitude for the noisy profiles and compared it with the unperturbed WGM profiles. However, a second approach arises if we examine the *standard deviation* associated with the amplitude of the noisy experimental data. The amplitude noise introduced in the WGM by the laser frequency noise (i.e., its linewidth $\Delta\upsilon_{LAS}$) is directly proportional to the slope of the **unperturbed**, *real* WGM profile. This means that, in the ideal case where the laser linewidth is negligible compared to the width of the sphere modes, the maximum noise amplitude will occur at the unperturbed WGM frequency coordinates of maximum slope: the *inflection* points. These points are symmetrically located at either side of the mode from its centre, and the difference between their frequency values is approximately equal to the linewidth of the unperturbed WGM ($\Delta\upsilon^{Q}{}_{WGM}$ according to our notation). This explains why we are focusing our attention towards the standard deviation of the recorded noisy modes: this parameter is *sensitive* to any noise amplitude change. That is, **the standard deviation of the amplitude of the**

noisy WGM's will exhibit two peaks, spaced apart by a frequency distance equal to the width of the unperturbed sphere mode. Hence, in this ideal case, the information that we were extracting from the modes recorded using a narrow linewidth laser would be available from the set of data acquired using a wide linewidth laser. This would allow for estimation of the DFB laser linewidth using relation (5.23), only requiring the use of **one** laser diode and thus simplifying the experimental requirements to a very significant extent.

However, in the real case presented during this chapter the linewidth of the DFB laser diode is not negligible compared to the width of the microsphere WGM. This effectively gives rise to a shift in the standard deviation maxima peaks, whose exact magnitude depends on the ratio between the laser and WGM linewidths. Further theoretical analysis is thus necessary to extract the linewidth of the unperturbed modes from the experimental data, opening up the possibility to implement this second novel technique in future work.

5.5. CONCLUSIONS

In this chapter we have investigated the optical properties and laser linewidth characterization applications of microspherical resonators in the 1.5 μm spectral regime, paying attention to the so-called Whispering Gallery Modes (WGM's) that can be excited within these microcavities under specific conditions. The fabrication process of high quality silica microspheres has been carefully detailed and demonstrated, with spherical microresonators of Q-factors of the order of 10^7 routinely fabricated. Excitation and characterization of single and multiple WGM's within the spheres has been achieved using two lasers of different linewidth

characteristics, a Discrete Mode (DM) narrow linewidth laser diode and a Distributed Feed Back laser diode, with a somewhat broader linewidth, directly acquired from industry. These diode lasers exhibit linewidth figures appropriate for spectroscopy applications and allow for easy application of modulation techniques compared to other more complex laser sources. This has allowed us to propose and demonstrate a novel application based on the WGM results to measure the linewidth of laser sources. The different thermal effects distorting the WGM intensity profiles have been discussed and an active feedback loop implemented that effectively suppresses these effects. This locking loop allowed for the set emission frequency of the laser to be locked to the resonant frequency of the targeted WGM at any time, significantly facilitating the subsequent experimental work. The absence of perturbing thermal effects allowed for the acquired WGM data to be analysed and results for the linewidth of the DFB laser extracted.

A novel method based on the WGM results has been then discussed and demonstrated in order to estimate the linewidth of the DFB laser diode utilised. The linewidth of the DFB and DM laser diodes has been first measured applying the self-homodyne measurement technique, yielding values of $\Delta\upsilon_{DM} \approx 550$ kHz and $\Delta\upsilon_{DFB} \approx 6.0$ MHz respectively. The WGM-based method to estimate the DFB linewidth, making use of the experimental data recorded with the two laser diodes, yielded a result of $\Delta\upsilon^{2laser}{}_{DFB} \approx 4.8$ MHz. Comparison of these results with the independent self-homodyne measurements leads to the conclusion that the novel approach demonstrated in this chapter yield consistent results, proving the validity of the novel microsphere-based experimental scheme as a linewidth measurement technique. The total accuracy achieved implementing this technique has been estimated and possible ways of improving such accuracy suggested. The basis for a second WGM-based method, only

requiring the experimental results obtained using the DFB laser diode, has been proposed and discussed in detail. It would allow for estimation of the DFB linewidth using only one single laser and simplifying to a great extent the experimental requirements. These new laser linewidth measurement experimental schemes open up new possibilities for further research and future work, either related to the characterization of noise processes affecting the spectral performance of lasers or to a deeper characterization and understanding of WGM's in optical microcavities.

5.6. REFERENCES

1. J. C. Knight, "Photonic crystal fibres," Nature **424**, 847-851 (2003).

2. P. S. J. Russell, "Photonic-Crystal Fibers," Lightwave Technology, Journal of **24**, 4729-4749 (2006).

3. A. Chiasera, Y. Dumeige, P. Féron, M. Ferrari, Y. Jestin, G. N. Conti, S. Pelli, S. Soria, and G. C. Righini, "Spherical whispering-gallery-mode microresonators," Laser & Photonics Review **9999**, NA (2009).

4. R. Laroy, "New concepts of wavelength tunable laser diodes for future telecom networks," in *Vakgroep Informatietechnologie (INTEC), Faculteit Ingenieurswetenschappen*(Universiteit Gent, Gent, Belgium, 2006).

5. C. Henry, "Phase noise in semiconductor lasers," Lightwave Technology, Journal of **4**, 298-311 (1986).

6. A. L. Schawlow, and C. H. Townes, "Infrared and Optical Masers," Physical Review **112**, 1940 (1958).

7. G. M. Stéphan, T. T. Tam, S. Blin, P. Besnard, and M. Têtu, "Laser line shape and spectral density of frequency noise," Physical Review A **71**, 043809 (2005).

8. K. Petermann, T. Okoshi, and T. Kamiya, *Laser Diode Modulation and Noise* (Kluwer Academic Publishers, 1991).

9. F. R. Connor, *Noise* (Edward Arnold (Publishers) Ltd., 1973).

10. C. Herbert, D. Jones, A. Kaszubowska-Anandarajah, B. Kelly, M. Rensing, J. O'Carroll, R. Phelan, P. Anandarajah, P. Perry, L. P. Barry, and J. O'Gorman, "Discrete mode lasers for communication applications," Optoelectronics, IET **3**, 1-17 (2009).

11. B. Kelly, R. Phelan, D. Jones, C. Herbert, J. O'Carroll, M. Rensing, J. Wendelboe, C. B. Watts, A. Kaszubowska, P. P. Anandarajah, C. Guignard,

and L. R. Barry, "Discrete mode laser diodes with very narrow linewidth emission," Electronics Letters **43** (2007).

12. J. Patchell, D. Jones, B. Kelly, and J. O'Gorman, "Specifying the wavelength and temperature tuning range of a Fabry-Perot laser containing refractive index perturbations (Invited Paper)," in *Opto-Ireland 2005: Optoelectronics, Photonic Devices, and Optical Networks*(SPIE, Dublin, Ireland, 2005), pp. 1-13.

13. R. Phelan, B. Kelly, J. O'Carroll, C. Herbert, A. Duke, and J. O'Gorman, "-40 °C < T < 95 °C mode-hop-free operation of uncooled AlGaInAs-MQW discrete-mode laser diode with emission at λ = 1.3 μm," Electronics Letters **45**, 43-45 (2009).

14. J. Elijah Kannatey-Asibu, "Broadening mechanisms," in *Principles of Laser Materials Processing*, J. W. Sons, ed. (2009), pp. 90-92.

15. H. Ludvigsen, M. Tossavainen, and M. Kaivola, "Laser linewidth measurements using self-homodyne detection with short delay," Optics Communications **155**, 180-186 (1998).

16. G. C. Bjorklund, "Frequency-modulation spectroscopy: a new method for measuring weak absorptions and dispersions," Opt. Lett. **5**, 15-17 (1980).

17. M. Nazarathy, W. V. Sorin, D. M. Baney, and S. A. Newton, "Spectral analysis of optical mixing measurements," Lightwave Technology, Journal of **7**, 1083-1096 (1989).

18. A. Biswas, H. Latifi, R. L. Armstrong, and R. G. Pinnick, "Time-resolved spectroscopy of laser emission from dye-doped droplets," Opt. Lett. **14**, 214-216 (1989).

19. H. M. Tzeng, K. F. Wall, M. B. Long, and R. K. Chang, "Evaporation and condensation rates of liquid droplets deduced from structure resonances in the fluorescence spectra," Opt. Lett. **9**, 273-275 (1984).

20. H. M. Tzeng, K. F. Wall, M. B. Long, and R. K. Chang, "Laser emission from individual droplets at wavelengths corresponding to morphology-dependent resonances," Opt. Lett. **9**, 499-501 (1984).

21. W. Stöber, A. Fink, and E. Bohn, "Controlled growth of monodisperse silica spheres in the micron size range," Journal of Colloid and Interface Science **26**, 62-69 (1968).

22. M. L. Gorodetsky, and V. S. Ilchenko, "Optical microsphere resonators: optimal coupling to high-Q whispering-gallery modes," J. Opt. Soc. Am. B **16**, 147-154 (1999).

23. G. Schweiger, and M. Horn, "Effect of changes in size and index of refraction on the resonance wavelength of microspheres," J. Opt. Soc. Am. B **23**, 212-217 (2006).

24. W. von Klitzing, R. Long, V. S. Ilchenko, J. Hare, and V. Lefèvre-Seguin, "Frequency tuning of the whispering-gallery modes of silica microspheres for cavity quantum electrodynamics and spectroscopy," Opt. Lett. **26**, 166-168 (2001).

25. C. Henry, "Theory of the linewidth of semiconductor lasers," Quantum Electronics, IEEE Journal of **18**, 259-264 (1982).

26. W. Press, S. Teukolsky, W. Vetterling, and B. Flannery, "Chapter 15: Modeling of Data, section 15.5 Nonlinear Models," in *Numerical Recipes 3rd Edition: The Art of Scientific Computing*(Cambridge University Press, 2007), pp. 809-810

27. D. W. Allan, "Statistics of atomic frequency standards," Proceedings of the IEEE **54**, 221-230 (1966).

28. L. S. Cutler, and C. L. Searle, "Some aspects of the theory and measurement of frequency fluctuations in frequency standards," Proceedings of the IEEE **54**, 136-154 (1966).

CHAPTER 6

CONCLUSIONS AND FUTURE WORK

6.1. OVERVIEW

The experimental work presented during this thesis was motivated by the wide range of possibilities that novel photonic microstructures open up in laser-based spectroscopy experiments. Due to the huge amount of research and development work concerning diode lasers carried out within the telecommunication industry sector during the last decades, applications of laser spectroscopy to gas sensing have undergone a spectacular development. On one hand, this research area has benefited from the progressively improvement and availability of laser sources exhibiting excellent characteristics regarding laser spectroscopy techniques. On the other hand, a huge amount of cutting-edge experimental work in this area has arisen during the last years due to the design and fabrication of new, exotic photonic microstructures that could not be even imagined only some decade ago. Our work was aimed to investigate and exploit the specific properties of the so-called *Hollow-Core Photonic Bandgap Fibres* (HC-PBF's) in gas sensing experiments, paying special attention to any emerging experimental schemes with potential applications to laser frequency stabilisation.

Considering the experimental work presented over the five chapters of this thesis, conclusion can be drawn that our initial aim has been undoubtedly fulfilled to a very significant and satisfactory extent. Setting the basic theoretical concepts, main description and experimental characterization of our laser spectroscopy system in **chapter 2** has first allowed us to step into the nonlinear absorption regime as reported in **chapter 3**. This regime was very attractive to our purposes, as some gas absorption effects happening under these particular conditions are potentially applicable to laser stabilisation. In particular, much work has been done during the last ten years regarding nonlinear optics in HC-PBF's [1], and several research groups around the world have reported studies of nonlinear acetylene absorption hosted in these fibres [2-4]. We have successfully characterised non-resonant saturation of acetylene transitions, and more importantly demonstrated a novel double-saturation scheme yielding consistent results. A closer look at some of these results suggests that the novel technique might be sensitive to fundamental properties of saturated gaseous systems, thus opening possibilities for further research.

Nonlinear effects using acetylene hosted in HC-PBF's have been utilised by some researchers to implement laser stabilisation techniques [5-9]. This encouraged us to apply the experimental results presented in chapter 3 to the laser stability field, leading to the successful implementation of a novel laser frequency locking technique as presented in **chapter 4**. High-accuracy stabilisation of the emission frequency of a high-power DFB laser diode has been demonstrated; with absolute frequency stabilisation figures comparable to those obtained using more complex techniques. In addition, the novel scheme allowed for stabilisation of the laser frequency in a modulation-free fashion significantly improving its potential applications. This is a significant feature that makes our approach more attractive than other schemes, plus it

is based in a simple, affordable experimental arrangement. Further optimization of the achieved results has been also discussed.

Lastly, a second photonic microstructure was targeted due to some of its optical properties directly related to laser linewidth characteristics and laser frequency stability. The so-called light-guiding *Whispering Gallery Modes* (WGM's) within optical microspheres have been investigated and reported in **chapter 5**, where a novel experimental scheme to estimate the emission linewidth of laser sources was proposed and demonstrated. High-quality microspheres were routinely fabricated that allow for extremely low losses of guided WGM's, enhancing light-matter interaction to a huge extent. The experiments were carried out using laser diodes of different linewidth characteristics, and linewidth measurements utilising the novel scheme have been reported, consistent with other well-known measurement techniques. Successful implementation of this microsphere-based scheme to study and characterize frequency noise processes in laser diodes opens up further possibilities for research. Much research is nowadays focused on this type of microresonators and WGM's [10], so investigation and merging of our stabilisation scheme with other techniques seems to be a promising, feasible aim.

6.2. FUTURE WORK

As described during the previous section and corresponding chapters, several possibilities arise to further extend our experimental work. Suggestions are first included in **chapter 3** regarding the optimization of nonlinear absorption signals in HC-PBF-based sensing schemes. This should be the basic, starting point to enhance the reported results and facilitate their subsequent application. Further optimization of

the frequency stability scheme demonstrated in **chapter 4** stands out as a very recommendable research line, because much interest is directed nowadays towards precise determination of the absolute frequencies of acetylene transitions in the 1.5 μm spectral region (it has been suggested as a reference for the creation of wavelength standards for the C-band of optical communications [8, 11]).

Finally, the novel laser measurement scheme demonstrated in **chapter 5** could also be optimized by some of the methods discussed during the corresponding conclusion section. Further improvement of the quality of the spherical microresonators would lead to WGM intensity profiles *extremely* sensitive to the frequency characteristics of the exciting laser source, opening the possibility of using our linewidth measurement scheme for more advanced characterization purposes.

6.3. REFERENCES

1. J. M. Dudley, and J. R. Taylor, "Ten years of nonlinear optics in photonic crystal fibre," Nat Photon **3**, 85-90 (2009).

2. F. Benabid, P. Light, F. Couny, and P. Russell, "Electromagnetically-induced transparency grid in acetylene-filled hollow-core PCF," Opt. Express **13**, 5694-5703 (2005).

3. S. Ghosh, J. E. Sharping, D. G. Ouzounov, and A. L. Gaeta, "Resonant Optical Interactions with Molecules Confined in Photonic Band-Gap Fibers," Physical Review Letters **94**, 093902 (2005).

4. R. Thapa, K. Knabe, M. Faheem, A. Naweed, O. L. Weaver, and K. L. Corwin, "Saturated absorption spectroscopy of acetylene gas inside large-core photonic bandgap fiber," Opt. Lett. **31**, 2489-2491 (2006).

5. M. J. Andrew, K. Kevin, L. JinKang, T. Rajesh, T. Karl, C. Francois, S. L. Philip, B. Fetah, R. W. Brian, and L. C. Kristan, "Stability of Optical Frequency References Based on Acetylene-Filled Kagome-Structured Hollow Core Fiber," in *Frontiers in Optics*(Optical Society of America, 2008), p. FWF7.

6. K. Nakagawa, Y. Sato, M. Musha, and K. Ueda, "Modulation-free acetylene-stabilized lasers at 1542 nm using modulation transfer spectroscopy," Applied Physics B (Lasers and Optics) **B80**, 479-482 (2005).

7. A. Onae, K. Okumura, J. Yoda, K. Nakagawa, A. Yamaguchi, M. Kourogi, K. Imai, and B. Widiyatomoko, "Toward an accurate frequency standard at 1.5 μm based on the acetylene overtone band transition," Instrumentation and Measurement, IEEE Transactions on **48**, 563-566 (1999).

8. P. Balling, and P. Křen, "Development of wavelength standard at 1542 nm: acetylene stabilized DFB laser," in *WDS'05 Proceedings of Contributed Papers: Part III - Physics*, J. Šafránková, ed. (Matfyz press, Charles University, Prague, 2005), pp. 590-594.

9. J. C. Petersen, and J. Hald, "Frequency and wavelength standards based on gas filled HC-PBFs," in *Lasers and Electro-Optics, 2008 and 2008 Conference on Quantum Electronics and Laser Science. CLEO/QELS 2008. Conference on*(2008), pp. 1-2.

10. A. Chiasera, Y. Dumeige, P. Féron, M. Ferrari, Y. Jestin, G. N. Conti, S. Pelli, S. Soria, and G. C. Righini, "Spherical whispering-gallery-mode microresonators," Laser & Photonics Review **9999**, NA (2009).

11. S. L. Gilbert, and W. C. Swann, *Acetylene 12C2H2 absorption reference for 1510 nm to 1540 wavelength calibration* (U.S. Dept. of Commerce, Technology Administration, National Institute of Standards and Technology, Boulder, Colorado, 2001).

Has de
Asimilar,
Mi habilidad,
Física.